Materials Horizons

ROYAL SOCIETY OF CHEMISTRY

REVIEW

View Article Online
View Journal | View Issue

Cite this: *Mater. Horiz.*, 2023, **10**, 1140

The fundamentals and applications of piezoelectric materials for tumor therapy: recent advances and outlook

Yan Wang,[a] Pengyu Zang,[a] Dan Yang,*[a] Rui Zhang,[a] Shili Gai[a] and Piaoping Yang *[ab]

Malignant tumors are one of the main diseases leading to death, and the vigorous development of nanotechnology has opened up new frontiers for antitumor therapy. Currently, researchers are focused on solving the biomedical challenges associated with traditional anti-tumor medical methods, promoting the research and development of nano-drug carriers and new nano-drugs, which brings great hope for improving the curative effect and reducing toxic and side effects. Among the new systems being investigated, piezoelectric nano biomaterials, including ferroelectrics, piezoelectric and pyroelectric materials, have recently received extensive attention for antitumor applications. By coupling force, light, magnetism or heat and electricity, polarized charges are generated in these materials microscopically, forming a piezo-potential and establishing a built-in electric field. Polarized charges can directly act on the materials in the tumor micro-environment and also assist in the separation of carriers and inhibit recombination based on piezoelectric theory and piezoelectric optoelectronic theory. Based on this, piezoelectric materials convert various forms of primary energy (such as light energy, mechanical energy, thermal energy and magnetic energy) from the surrounding environment into secondary energy (such as electrical energy and chemical energy). Herein, we review the basic theory and principles of piezoelectric materials, pyroelectric materials and ferroelectric materials as nanomedicine. Then, we summarize the types of piezoelectric materials reported to date and their wide applications in treatment, imaging, device construction and probe detection in various tumor treatment fields. Based on this, we discuss the relevant characteristics and post-processing strategies of nano piezoelectric biomaterials to obtain the maximum piezoelectric response. Finally, we present the key challenges and future prospects for the development of ferroelectric, piezoelectric and pyroelectric nanomaterial-based nanoagents for efficient energy harvesting and conversion for desirable therapeutic outcomes.

Received 30th September 2022,
Accepted 3rd January 2023

DOI: 10.1039/d2mh01221a

rsc.li/materials-horizons

1 Introduction

Malignant tumors are difficult to treat because of their high mortality rate and significant metastasis, making anti-tumor therapy one of the most challenging medical tasks. The treatment of primary tumors mainly relies on local surgery and radiotherapy in current clinical practice. However, they are usually associated with high side effects, poor prognosis, and high drug resistance. Also, primary tumors colonize distant organs in a series of "metastatic cascades." Metastatic tumors are a systemic disease. In this case, the primary method for preventing and treating tumor metastasis is systemic therapy in current clinical practice, including chemotherapy, targeted therapy, and immunotherapy.[1] However, these strategies have the shortcomings of adverse effects, effectiveness in a tiny portion of the population, and lengthy treatment times. The process of tumor metastasis involves several basic steps including the local invasion of primary tumor cells, infiltration and circulatory survival of the blood or lymphatic system, arrest and exosmosis of distant organs, survival in a new environment, and metastatic colonization.[2,3] The process of tumor metastasis consists of several basic steps that local invasion of primary tumor cells, infiltration and circulatory survival of the blood or lymphatic system, arrest and exosmosis of distant organs, survival in a new environment, and metastatic colonization. Metastatic cancers can be inhibited by intervening in the progression of one step in the metastatic cascade. Also, the characteristics of the metastatic

[a] *Key Laboratory of Superlight Materials and Surface Technology, Ministry of Education, College of Material Science and Chemical Engineering, Harbin Engineering University, Harbin, 150001, P. R. China. E-mail: yangdan@hrbeu.edu.cn, yangpiaoping@hrbeu.edu.cn*

[b] *Yantai Research Institute, Harbin Engineering University, Yantai 264000, P. R. China*

tumor microenvironment can provide a basis for current and future metastatic therapy. In recent years, concerted efforts to improve cancer treatment have yielded some results. With the rapid pace of the development of nanomaterials into antitumor biomaterials, various smart nanomedicine devices and drugs have been carefully designed and constructed, with researchers striving for a breakthrough in basic research and clinical trials.[4] The physical and chemical properties or biological effects of nano-preparations determine their safety, efficient precision diagnosis and treatment effect.[5–7] Shi and colleagues used piezoelectric materials to improve ultrasound power therapy, which was the first application of piezoelectric materials as nanomedicines in the antitumor field.[1] The built-in electric field separates electrons and holes, thereby improving the ability to generate reactive oxygen species for tumor treatment under piezoelectric catalytic modulation. Based on FEM simulative analysis, they determined that the built-in electric field can regulate the energy band, which is more favorable for the production of toxic reactive oxygen species. This suggests that the introduction of piezoelectric effects in photodynamic therapy modalities for nanomedicines is indeed a promising avenue for development. This work complements traditional photodynamic therapy with new working principles, which is an example of multidisciplinary cross-collaboration in solving practical scientific problems.

Piezoelectric materials are crystals in which a voltage appears between their two end faces when subjected to pressure, where the piezoelectric effect exists in most non-centrosymmetric crystals.[8] Piezoelectric materials without a center of symmetry include pyroelectric materials and ferroelectric materials. Specifically, a pyroelectric material is also a piezoelectric body, and its crystal structure similarly does not have a center of symmetry. Temperature changes in pyroelectric materials can cause polarization intensity changes, but not all piezoelectric bodies are pyroelectric bodies. Ferroelectric crystals are piezoelectric, but their crystal structure does not have a center of symmetry. A ferroelectric body must be an ionic crystal, which is a type of piezoelectric body with spontaneous polarization, but not all piezoelectric bodies are ferroelectric. Ferroelectric materials can cause polarization intensity changes under the action of a magnetic field. Thermoelectric materials include ferroelectric materials, which are branches of piezoelectric materials. It is worth noting that the piezoelectric materials mentioned herein do not specifically distinguish them, where piezoelectric materials are used as representatives, which all have their own advantages, as detailed in Section 2. Nanodrugs and devices can be designed by selecting suitable materials for different purposes and environments. In terms of physical and chemical properties, piezoelectric materials can be broadly classified into three categories, *i.e.*, inorganic, organic and composite piezoelectric materials. Among the inorganic piezoelectric materials, the representative lead-free ferroelectric materials with a chalcogenide structure include $BaTiO_3$ (BTO), $BiFeO_3$ (BFO), $LiTaO_3$, alkali niobate (K, Na, Li, and Ag) NbO_3, alkali bismuth titanate (K and Na) $_{0.5}Bi_{0.5}TiO_3$, $ZnSnO_3$, Bi_2WO_6, $CaTiO_3$, and $SrTiO_3$, which have high electromechanical coupling.[9–14] The second type of inorganic piezoelectric material is wurtzite structure crystals, belonging to the hexagonal crystal system, such as ZnO, SiC, AlN, GaN, InN, BN, CdS, and CdSe.[15,16] Organic piezoelectric materials include polymers and biomolecular piezoelectric materials. Some flexible polymers have an asymmetric molecular structure and orientation, and their molecular dipole is reoriented after stretching, thus exhibiting ferroelectricity and piezoelectricity.[17] Bio-piezoelectric polymers have excellent mechanical flexibility and low biotoxicity. The most representative bio-piezoelectric polymer is polyvinylidene fluoride [PVDF, $(CH_2CF_2)_n$]. The electronegativity difference between hydrogen and fluorine atoms produces a molecular dipole, resulting in the piezoelectric effect. The properties of PVDF copolymers can be improved, for example, polyvinylidene fluoride trifluoroethylene [P(VDF-TrFE)] copolymers have higher flexibility, better crystallinity, higher residual polarization and electromechanical coupling factor compared to PVDF. The piezoelectric effect exists not only in PVDF and its copolymers, but also in polymers such as poly-L-lactic acid, polyacrylonitrile, poly-β-hydroxybutyrate, polyvinyl chloride, and odd nylon (*e.g.*, nylon-11). Interestingly, piezoelectric effects are also present in many biomolecules (*e.g.*, amino acids, peptides, and proteins) and biological tissues (bone, ligaments, tendons, skin, and hair) as a result of the structural asymmetry of biomolecules.[18] For example, amino acids with non-centrosymmetric crystal structures have ferroelectric properties, while peptides and proteins have amino acids as their basic units, and thus amino acid sequences and spatial conformations determine the biological functions of peptides and proteins, thus providing structure-dependent piezoelectric properties. Compared with inorganic bio-piezoelectric materials, most organic bio-piezoelectric polymers generally exhibit relatively lower piezoelectric charge coefficients, resulting in lower charge generation levels. Piezoelectric composites are constructed by combining organic piezoelectric materials with inorganic piezoelectric materials. Consequently, the excellent flexibility of organic piezoelectric materials is retained, while the high electromechanical coupling performance of inorganic piezoelectric materials is obtained, thus improving the overall piezoelectric performance.[19] In addition, smaller dimensions can provide stronger electron transfer rates and the ability to interact with the substrate, and thus the dimensionality of piezoelectric materials also affects their performance.[20]

Piezoelectric materials have a wide range of applications and have been used in various fields since their discovery including sensing,[21–27] driving,[28,29] and transduction.[30–32] Obviously, these applications do not rely on piezoelectric effects alone, given that some piezoelectric materials also possess pyroelectric and ferroelectric properties, which allow wonderful correlations among force, light, electricity, magnetism, and heat and provide new research frontiers for antitumor therapeutic exploration. Herein, we introduce bio-piezoelectric platforms from the perspective of antitumor therapeutic system design (Scheme 1), focusing on their theoretical basis as nanomedicines and carriers, summarizing strategies to improve their piezoelectric properties, and reviewing their recent biomedical applications for cancer therapy

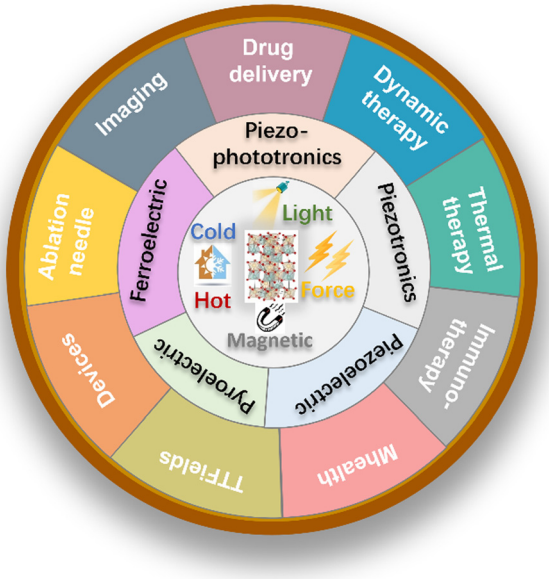

Scheme 1 Schematic overview of the structure of this review.

and diagnosis. This review aims to gain insight into the theoretical mechanisms underlying the state-of-the-art piezoelectric biological platforms and provide new insights into future strategies for the design of antitumor therapies. Finally, the future challenges and opportunities related to piezoelectric materials and biology are prospected.

2 Piezoelectric, pyroelectric and ferroelectric effect

2.1 Piezoelectric, pyroelectric and ferroelectric effect

2.1.1 A brief introduction of piezo-, pyro-, and ferroelectric effect. In 1880, brothers Pierre and Jacques Curie discovered the piezoelectric effect while studying crystal symmetry. The piezoelectric effect exists in crystalline materials with non-symmetric structures, where among the 21 non-centrosymmetric crystal classes, 20 exhibit the piezoelectric effect (Table 1).[33,34] Materials with a piezoelectric effect are called piezoelectric materials. When mechanical stress (including stretching, squeezing and twisting) is applied to a piezoelectric material, the material will undergo microscopic mechanical deformation due to the external force. The lack of central symmetry leads to the displacement of the centers of positive and negative charges in the material, generating polarization phenomena.[17] Subsequently, positive and negative polarized charges appear on the surfaces of the opposite ends of the material, generating a piezo-potential distributed along the direction of stress. The charge density is proportional to the strength of the external mechanical stress. This phenomenon of polarization and electricity generated by stress is called the piezoelectric effect. When the applied mechanical stress is removed, the material deformation is restored and it returns to the uncharged state. This process is the conversion of stress to electricity, and the polarity of the charge changes with the direction of the stress. This process of converting mechanical energy into electrical energy is defined as the direct piezoelectric effect, which can be applied to signal pickup. The piezoelectric effect also includes the converse piezoelectric effect, which is the conversion of electricity to stress, *i.e.*, when an electric field is applied in the polarization direction of a piezoelectric material, the material is mechanically deformed, and when the electric field is removed, the material deformation disappears, and this process can be applied to signal excitation. Therefore, the piezoelectric effect is the coupling of dynamics and polarization. Whether a material has a piezoelectric effect is determined by the symmetry of its structure. Therefore, the piezoelectric effect is generated under the following conditions: (1) dielectric materials, (2) crystal structure has no center of symmetry, and (3) structure must have positively and negatively charged masses, *i.e.*, a piezoelectric material is an ionic crystal or molecular crystal composed of ionic clusters, and these materials are also called piezoelectrics (PZT).

In addition, among the 20 non-centrosymmetric point groups, there are 10 polar crystals with a unique polar axis, in which spontaneous polarization occurs, showing different properties at the two ends of the polar axis.[35] They are crystals that are spontaneously polarized by the polarity axis. The effect of an external electric field does not change the polarized degree of the crystal or the polarized direction because the dipole moments of all particles are parallel. These materials not only can exhibit piezoelectric effects due to mechanical stress effects but also can change their polarization intensity due to thermal expansion upon temperature changes. This phenomenon of spontaneous polarization of crystals due to temperature changes is called the pyroelectric effect. As the crystal temperature changes, positive and negative polarization charges are generated on the crystal surface perpendicular to the polar axis. These polar crystals whose spontaneous polarization intensity increases with an increase in temperature are called pyroelectrics. Only pyroelectrics have only one orientation of spontaneous polarization and do not steer with an applied electric field.

Table 1 General dielectric, piezoelectric, pyroelectric and ferroelectric types and their point group

Dielectric crystal type (32)		
Non-centrosymmetrical crystal type (21), Among them, piezoelectric crystal (20)		
	Polar crystal (10)	1, 2, 3, 4, 6, *m*, *mm*2, 4*mm*, 3*m*, 6*mm*
	Nonpolar crystal (11)	222, 32, 422, 622, 23, $\bar{4}$, $\bar{4}m2$, $\bar{6}$, $\bar{6}m2$, $\bar{4}3m$, 432 (no piezoelectric)
Centrosymmetrical crystal type (11)		$\bar{1}$, 2/*m*, $\bar{3}$, 4/*m*, 6/*m*, *mmm*, $\bar{3}m$, 4/*mmm*, 6/*mmm*, *m*3, *m*3*m*

There are also several crystal point groups in pyroelectric materials, which have spontaneous polarization in the appropriate temperature range and have two or more possible orientations for spontaneous polarization. This part of pyroelectrics is called ferroelectrics.[33,36] In the natural state, there are many small polarization regions inside ferroelectrics, and the electric dipole polarization in each small region is arranged in the same direction, but the orientation of each small region is different, leading to the formation of domains. Given that the electric domains are randomly distributed in the crystal, the electric dipole orientation in each domain is different, the polarizations will cancel each other and the total polarization intensity of the material is zero. When a material is exposed to a large external electric field, its domain orientations can be reoriented by the electric field to align in individual directions for overall material polarization. This property is known as ferroelectricity, which is a unique aspect of ferroelectric materials. However, when a ferroelectric material warms up above its critical temperature, *i.e.*, the Curie temperature (T_c), it is converted from ferroelectricity to paraelectricity. Subsequently, the symmetry of the structure increases and the spontaneous polarization disappears. Therefore, the spontaneous polarization of ferroelectrics occurs in the range of temperatures less than the Curie temperature. The spontaneous polarization dipole moment of ferroelectric materials can change with the direction of the externally applied electric field and lags behind it. This phenomenon is called the ferroelectric effect. Specifically, the degree of polarization along the polarity axis of a crystal material can be reversed by reversing the polarity of the electric field. The relationship curve between the degree of polarization of ferroelectric materials and the strength of the applied electric field is called the electric hysteresis line. Commonly, ferroelectrics possess a hysteresis loop, structural phase transition temperature (*i.e.*, Curie point), and critical properties.

Therefore, general dielectric materials will produce polarization under the action of an electric field. Piezoelectric materials will also produce polarization because of their asymmetric center, and when there is directional mechanical stress acting on their surface, they deform, and their positive and negative charge centers are displaced. By default, pyroelectrics are classified as a subclass of piezoelectrics. Pyroelectric materials not only have piezoelectric effects but also undergo spontaneous polarization phenomena with a change in temperature because of their unique polar axes and polar dipole moments. Although the change in temperature is directionless, it causes spontaneous polarization in pyroelectric materials. Similarly, this is why ferroelectric materials belong to a subclass of piezoelectric and pyroelectric materials. All ferroelectric materials are both pyroelectric and piezoelectric materials. The spontaneous polarization of ferroelectric materials can be induced by other conditions besides a change in temperature. Because of the presence of electric domains, the number of polarization orientations in the ferroelectric body will be greater than two, which will change with a change in the external electric field. However, when the Curie temperature is exceeded, a phase transition occurs and the ferroelectricity disappears, as summarized in Fig. 1.

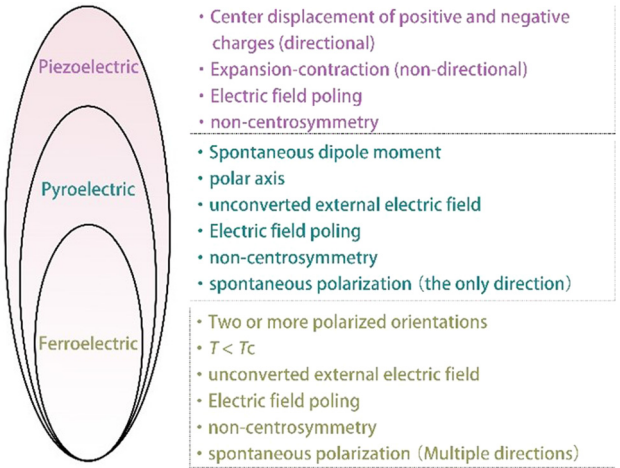

Fig. 1 Relationship among piezo-, pyro-, and ferroelectric materials and their properties.

2.1.2 The fundamental theory of the piezo-, pyro-, and ferroelectric effects. Most crystals have symmetric cells, but not piezoelectric crystals. Piezoelectricity arises from the asymmetrical nature of the crystal structure. Specifically, the absence of a center of symmetry in a crystal structure results in the presence of electric dipoles in it, forming two equal and different point charges with overlapping centers in the cell (Fig. 2A).[36] Despite the asymmetrical arrangement of atoms in the lattice, piezoelectric crystals remain electrically neutral due to the adjacent negative charges canceling out the positive charge. However, if a piezoelectric crystal is squeezed or stretched, the atoms move away from their positions. Thus, a net charge is acquired throughout the crystal, where the net positive and electronegative charges appear on opposite sides and outer surfaces of the crystal, as in the case of wurtzite zinc oxide. The hexagonal wurtzite ZnO crystal structure lacks centrosymmetry, where the Zn^{2+} and O^{2-} are tetrahedrally coordinated. The centers of the positive and negative ions overlap, and the crystal as a whole shows no spontaneous polarization. When stress is applied to the unit cell, the original atomic positions of the O^{2-} and the Zn^{2+} are shifted relative to each other, which leads to the acquisition of dipole moments in the unit cell. Consequently, the crystal acquires a piezopotential due to the collective induced polarization of the charges in the entire cell in the piezoelectric crystal.

Pyroelectric materials can be spontaneously polarized due to their unique polarity axis. Temperature changes lead to changes in the degree of spontaneous polarization and exhibit charge release phenomena.[33,35] In the case of ZnO (Fig. 2B), if the temperature remains constant ($dT/dt = 0$), the balance between shielding and polarization charges in the crystal remains constant, and therefore no potential or pyroelectric current is generated. When the temperature increases, the thermal vibrational energy of the zinc ion increases and it is difficult to fix it at a position away from the center. The odds of

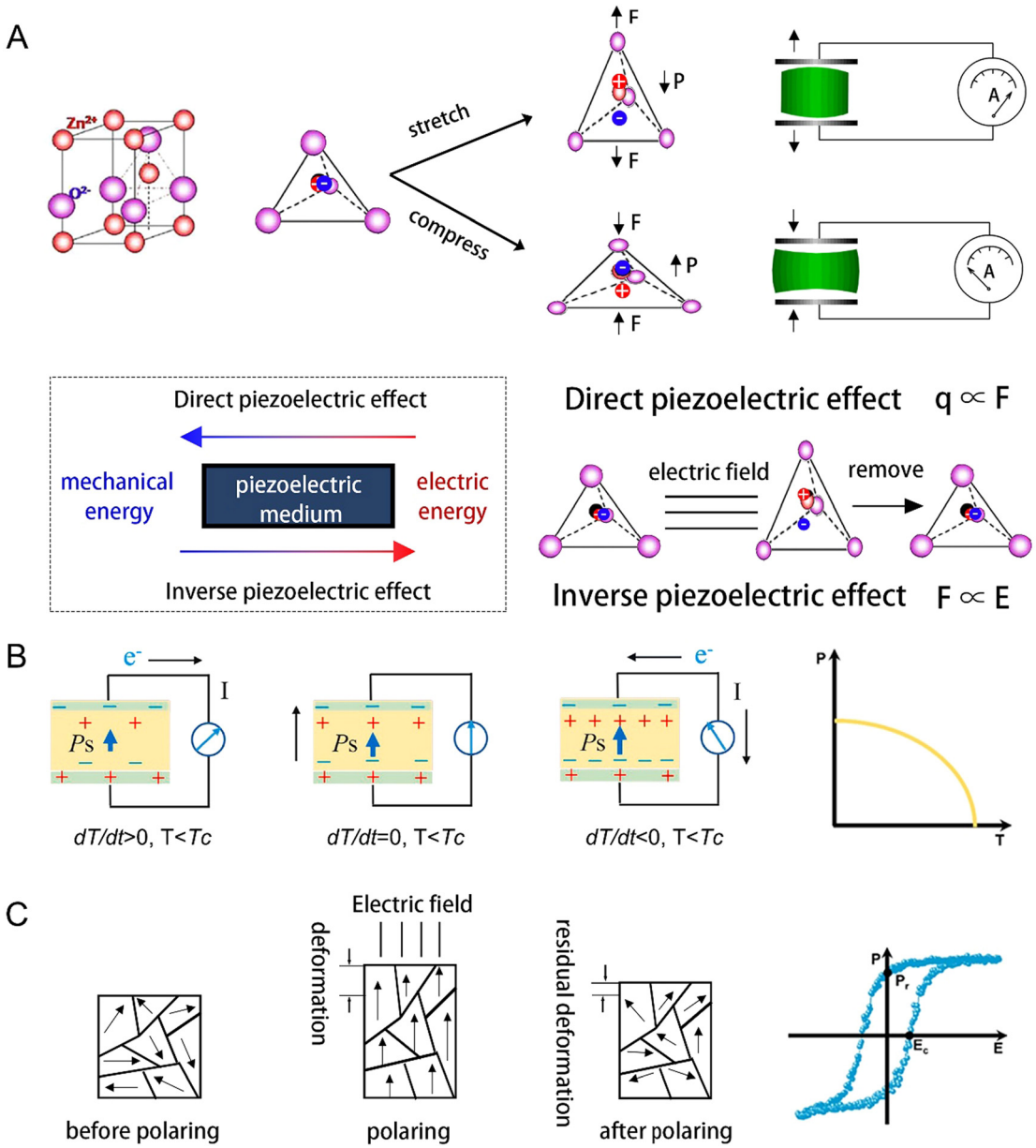

Fig. 2 Mechanism of the piezo-(A), pyro-(B), and ferroelectric (C) effects.[33,35] Copyright 2020, the American Chemical Society.

its proximity to the oxygen ion are equal and the crystal maintains a high degree of symmetry. At this point, the electric dipoles in the pyroelectric body experience large-angle oscillations relative to the direction of their respective alignment axes, and they also lose their orientation. Consequently, the polarization amplitude of the pyroelectric decreases and the polarized charge is reduced, indicating that the original electrical equilibrium between the shielding and polarized charges is partially broken. The constraint of the built-in dipole on the shielding charge is weakened, allowing a portion of the shielding charge to flow to the surface of the matter, which becomes pyroelectric free charges and establishes a new equilibrium. This leads to the redistribution of free charge throughout the crystal. If a pyroelectric material is connected to an open circuit in its pristine form, a large amount of free charge resting on its surface is released from both polar surfaces of the pyroelectric element and flows as a current. On the contrary, when the temperature decreases ($dT/dt < 0$), the thermal vibrational energy of the zinc ion decreases and its energy is not sufficient to overcome the electric field effect of the asymmetric oxygen ion. The Zn ions are fixed at a position off-center. Moreover, the electric dipole only undergoes small oscillations, increasing the polarization intensity. Therefore, the polarization charge is more than the shielding charge and the free charge is redistributed to compensate for the dipole change. Simultaneously, a charge opposite to the shielding charge is generated on the surface. Similarly, a pyroelectric current also occurs if a pyroelectric element is connected to an open circuit. However, the direction of this current is opposite to the former.

There are many crystals with ferroelectricity, which can generally be divided into two major groups, where the first is potassium dihydrogen phosphate KH_2PO_4 (KDP) with hydrogen bonds. Its transition from a *cis*-electric phase to ferroelectric phase is a disordered–ordered phase transition. In the case of the hydrogen-bonded iron transistors represented by KDP, the data of neutron bypassing showed that above the Curie temperature, the distribution of protons along the hydrogen bonds is in a symmetric bell-spread shape. Below the Curie temperature, the distribution of protons is more concentrated and asymmetric to the neighboring ions, and the protons are closer to the hydrogen bonding end. The other category is represented by barium titanate, where the transition from a *cis*-electric phase to a ferroelectric phase is due to the relative displacement of two of the sublattices. For ferroelectrics represented by chalcogenide type, bypassing experiments proved that the appearance of spontaneous polarization is due to the relative displacement of the sublattice of positive ions from the sublattice of negative ions.

Ferroelectric materials are piezoelectric materials with good piezoelectric properties simultaneously. Given that the positive and negative charge centers of ferroelectrics do not coincide, they generate electric dipole moments spontaneously (Fig. 2C).[8,33] Therefore, they can change the polarization direction under the action of an applied electric field. It is also possible to change the electric dipole moment of a material under the action of a force field for it to macroscopically exhibit polarization, producing a piezoelectric effect, which makes the surface of the material electrically charged. Ferroelectric materials are also pyroelectric materials with pyroelectric properties. Pyroelectricity is a phenomenon in which the temperature of a material changes, resulting in a change in the electrodynamic state of the material. Ferroelectrics that have not been artificially polarized by an external electric field (electret) do not exhibit polarity macroscopically, and therefore have no pyroelectric properties, where only electret-treated ferroelectrics have polarization and can produce pyroelectric effects.

Because polarization creates a built-in electric field in a piezoelectric material, it can drive free carriers to migrate in different directions. Moreover, the direction and degree of polarization can be controlled by applying external forces, adjusting the temperature, and changing external electric/magnetic fields. This gives the piezoelectric material more freedom to adjust the local band changes at the interface of the piezoelectric/active material or piezoelectric heterojunction, resulting in dynamic control of surface properties and surface redox reactions of the material.

2.2 Piezotronic effect and piezophototronic effect

2.2.1 Piezo-potential: the core of piezotronics and piezophototronics. Piezoelectric effects are widely found in asymmetric materials such as piezoelectric, pyroelectric, ferroelectric and nonlinear optical materials. Interestingly, some piezoelectric materials with bandgaps of about 2.5–3.5 eV also have typical semiconducting properties, allowing the two properties to be coupled synergistically.[37] The process of piezoelectric effect creates a piezo-potential and a built-in electric field due to the generation and migration of positive and negative polarization charges. The piezo-potential and built-in electric field can induce changes in the height of the potential barrier at the semiconductor interface, making it possible to engineer charge carrier properties at the heterojunction interface and in the bulk phase. This coupled structure, based on both semiconductor and piezoelectric properties, belongs to the category of piezotronics.[38] The concept of piezotronics was first proposed by Academician Zhonglin Wang and coworkers in 2006 and introduced in 2007, *i.e.*, the basis of the piezotronic effect is the use of the piezo-potential to regulate and control the carrier transport properties of the interface or junction region.[39]

In 2010, Academician Zhonglin Wang and coworkers also proposed the concept of piezophototronics.[40,41] The field of piezoelectric photoelectronics is the study of the coupling effect among semiconductor, optical excitation and piezoelectric properties. In this case, the semiconductor has both piezoelectric and photosensitizing properties. It generates photoinduced electrons and holes under illumination, also providing strain-induced polarizing charge to facilitate charge separation for surface reduction and oxidation. These intrinsic properties are determined by the discontinuity of the local band structure and the concomitant band arrangement. Piezophototronic effects focus on the use of piezoelectric charge/potential as a ''gate'' voltage to regulate the carrier migration behavior (separation, transport and complexation) and redox dynamics at interfaces or junctions, providing the driving force for the transport of photocatalytic carriers (electrons/holes) in the designed direction and promoting their separation and inhibition their complexation, which can directly affect the performance of the properties in generating reactive oxygen species. Piezophototronics has developed rapidly since it was first proposed by Academician Zhonglin Wang in 2010, but a renewed understanding of the structure and properties of interfacial energy bands in semiconductors is important for practical applications. With the development of piezophototronics, transistors, nanogenerators, light-emitting diodes and solar cells have rapidly developed, and recently also been widely investigated in catalysis and photolysis of water. However, there are few reports on the introduction of piezophototronics in the development of nanomedicines.

Therefore, in the case of materials with semiconductor, photoexcitation and piezoelectric properties, those with coupling structures can be divided into four types (Fig. 3), as follows:[42] (1) research on the coupling effects of semiconductor properties and photoexcitation properties belongs to the field of optoelectronics, which are mostly used in photoelectric communication, data processing, information storage, imaging technology, photocatalysis, photodynamic therapy, photolysis of water, *etc.* (2) The study of the coupling effect between semiconductor and piezoelectric properties belongs to the field of piezoelectric electronics, which are mostly used in energy harvesting and conversion processes, such as strain sensors, diodes, transistors, Schottky contact chemical sensors and other devices. (3) The

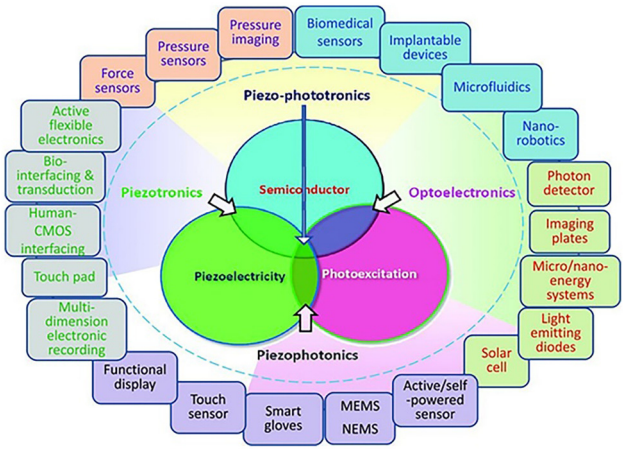

Fig. 3 Schematic diagram of coupling effects among semiconductor, photoexcitation and piezoelectric properties and their potential applications.[38] Copyright 2016, Wiley-VCH.

study of the coupling effect between photoexcitation and piezoelectric properties belongs to the field of piezophotonics, which are mostly used in stress luminescence, bioimaging and stress sensing. (4) The study of the coupling effect between semiconductor, photoexcitation and piezoelectric properties belongs to the field of piezophototronics, which are mostly used in solar cells, photodetectors, light-emitting diodes and photocatalysis.

2.2.2 Fundamental theory of piezotronic and piezophototronic effects. After light stimulation, only photogenerated charge carriers are generated in a non-polarized semiconductor, while no charge is created in the semiconductor, whether or not if it is polar or non-polar. In their native condition, titanium dioxide and barium titanate are examples. When the light-induced free electrons contact an ionic solution, they flow across the interface towards the ionic solution due to the difference in the work functions of the two phases, causing the semiconductor band to bend upward. This band bending prevents electron transmission in surface reduction processes but promotes hole transfer in oxidation reactions (Fig. 4A).[43,44] When the semiconductor conduction band energy level is more negative than the usual redox potential of $^{\bullet}O_2^-/O_2$ (0.33 V *vs.* NHE), the electrons in the conduction band can reduce the adsorbed O_2 molecules to $^{\bullet}O_2^-$ free radicals. The valence band energy level of the semiconductor is rectified by the typical redox potential of $^{\bullet}OH/-OH$ (+1.9V *vs.* NHE), causing the holes in the valence band to oxidize $-OH$ to $^{\bullet}OH$. However, redox processes cannot occur without further treatments, such as perfect barium titanate crystals, given that the concentration of free charge in certain semiconductor crystals is relatively low. In addition to semiconductor capabilities, barium titanate crystals exhibit piezoelectric qualities. After the material is polarized, the piezoelectric action causes the polarization charge to collect at the conduction and valence bands of the semiconductor material, resulting in the displacement of the conduction and valence bands. The band bending of the polarized semiconductor is presented in Fig. 4(Aiii and iv). After polarization, the surface with positive polarization charge accumulation is designated as V^+ in the image, while the surface with negative polarization charge accumulation is marked as V^-. The potential lowers throughout the domain at the V^+ surface, leaving the surface with a lower potential than the bulk, which results in downward bending at V^+. Similarly, a cross-domain potential is formed in a negatively charged surface (V^-), which places the surface at a greater potential than the bulk, forcing V^- to bend upward. Meanwhile, as shown in Fig. 4(Bi), the accumulation of positively and negatively polarized charges attracts the aggregation of electrons and holes on the V^+ plane and V^- plane, respectively. Therefore, the internal electric field of barium titanate materials shows spontaneous polarization, and the strength of the internal electric field determines the degree of band bending at the interface. The piezoelectricity regulates the energy band bending and electron transfer of semiconductors in solution, similar to the effect on heterojunctions.[45] Similarly, in heterojunctions such as P–N and Z-scheme, the charge carriers transmitted through the junction are strongly dependent on the polarization charge. In addition, the polarization charge is also affected by the degree and direction of the external stimulus strain, and thus the piezoelectric effect can be reasonably regulated to control the transfer of charge carriers.[46]

In addition, the migration of the charge carriers in a semiconductor or the absorption of the surrounding medium will neutralize the polarization charge and produce a depolarization field, as shown in Fig. 4(Bii). Both the polarization and depolarization processes affect the bending of the energy band, consequently affecting the carrier transfer in the material (Fig. 4C). In a polarized semiconductor, the piezoelectric potential gradient generated in the material attracts the flowing charge carriers in opposite directions to the crystal surface based on the opposite attraction principle. However, when sufficient external shielding charge accumulates on the surface to balance the polarization charge, the piezo-potential decreases to zero. Thus, the driving force of carrier transfer is suppressed, and the oxidation–reduction reaction is delayed by a new potential equilibrium. Gradually, the new potential equilibrium in the polarized crystal breaks down with the weakening external strain, leading to the reversal of the carrier transfer direction.

In summary, piezotronics and piezophototronics both regulate the energy band bending and carrier transfer process by a piezo-potential. This is based on the tuning effect of the piezoelectric effect on the carrier transfer behavior of semiconductors, and thus the piezo-potential is their core and foundation. A piezoelectric potential is generated either by mechanical force or temperature stimulation, or by spontaneous polarization. Varying degrees of band bending obtained by adjusting the direction and strength of external stimulus strain will lead to different surface carrier transfer dynamics, consequently affecting the reaction on the material surface. Also, the driving force for the target reaction (redox potential of the charge) can be manipulated in a certain ionic solution.

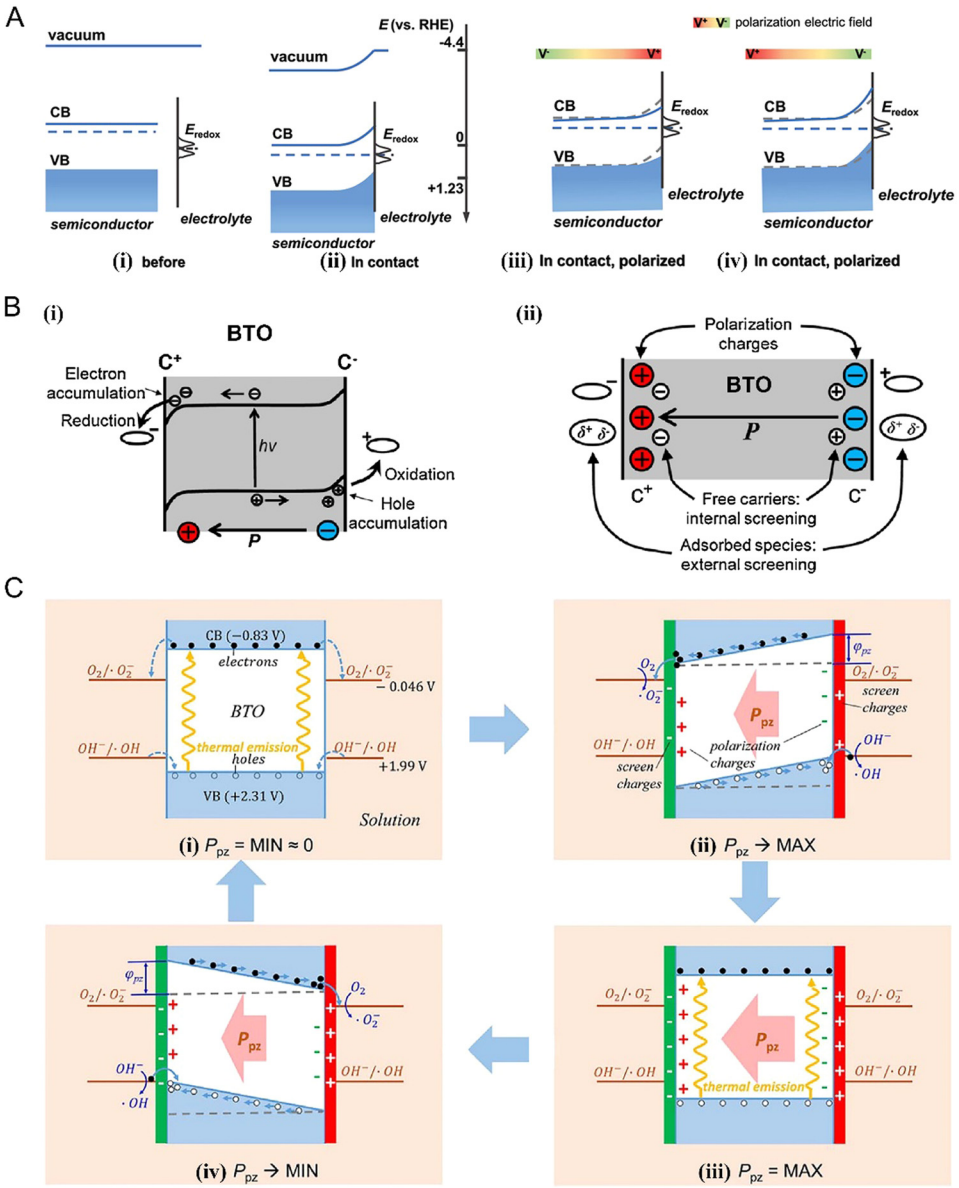

Fig. 4 (A) Band structure diagram of n-type semiconductor/electrolyte interface before and after contact or under positive and negative polarization. The gray dashed line and blue solid line represent the strip edges without strain and under strain, respectively.[43] Copyright 2020, Wiley. (B) Change in the band structure of ferroelectric $BaTiO_3$. (i) Polarization and depolarization fields. (ii) Effect of piezo-potential on the aggregation of carriers and redox reactions in valence bands. (C) Band bending as a function of polarization strength.[36] Copyright 2019, Elsevier.

3 Method of forming piezo-potential

As mentioned above, the piezo-potential can form an internal electric field to improve the separation rate of photogenerated carriers. However, a static built-in electric field can easily lead to saturation of free carriers due to electrostatic shielding, which reduces the carrier separation rate. The piezo-potential is attributed to the generation of positive and negative charges on opposite surfaces of the material. However, the pathways for generating the charges are different, and thus there are various ways to generate a piezo-potential. Nowadays, the common methods to generate a piezoelectric potential in piezoelectric materials for antitumor applications include external electric field, ultrasonic vibration, mechanical stress, and thermal expansion.

When an electric field is in the outer substances, interaction will occur. Dielectrics are formed under the action of an external electric field, with the repulsion of the same charge, whereas attraction between heterogeneous charge. The dielectric surface will contain positive and negative induced charge, dielectric internal along the electric field direction of the induced electric dipole moment, the dielectric surface phenomenon of bound charge, dielectric polarization phenomenon, and then produce a piezoelectric potential. From the perspective of the microscopic mechanism of polarization, four basic

forms of dielectric polarization can be summarized, as follows: (1) electron polarization. This refers to the small displacement of the negatively charged electron cloud of the constituent particles (atoms, ions, or molecules) of the dielectric under the action of an external electric field relative to the positively charged nucleus. The positive and negative charge equivalent centers of electrically neutral atoms are separated, forming a small electric dipole and generating an induced electric dipole moment. (2) Atomic or ionic polarization. This refers to the relative displacement between electrons and nuclei in atoms or between different ions along the direction of the electric field under the action of an external electric field. It also forms a small electric dipole with positive and negative polarity, which generates an induced electric dipole moment. (3) Steering polarization of a dipole. This refers to the chaotic distribution of inherently polar molecules in a dielectric under the action of an external electric field, which will twist or align along the direction of the electric field. Consequently, a macroscopic induced dipole moment is produced. (4) Space charge polarization or interfacial polarization of interlayer media. The dielectric permittivity and conductivity are different between layers because of the heterogeneous dielectric medium composed of two or more materials. The charge at the interface of the layers must move under the action of an electric field. The migration process may be captured by defects in the medium or the interface between different media. To adapt to the potential redistribution, the electric charge accumulates on the interface, forming positive and negative poles, and a macroscopic-induced electric dipole moment is generated. If this piezoelectric happens to be a semiconductor, the free charge in the conductor is redistributed by the electric field and an induced charge appears on the surface of the conductor to achieve electric field polarization. A dielectric differs from a semiconductor in that the quantity of the polarized charge on the dielectric is much less than the induced charge on the semiconductor because the activity of the bound charge cannot extend beyond the atomic range.

Periodic sound pressure is generated during the propagation of ultrasonic waves in the medium and high strength local limit pressure is formed by the collapse of the acoustic cavitation wall (>100 MPa), given that stress can cause deformation of the dielectric, and then affect its polarization strength.[47] The strength of internal polarization and piezoelectric potential can be easily changed by varying the working power and frequency of the ultrasonic wave, and thus the applied stress. Therefore, ultrasonic vibration is the most widely employed method in piezoelectric photoelectric catalysis. The charge carriers are separated by means of ultrasonic-induced alternating internal electric fields. This is expected to improve the material efficiency. However, the ultrasonic wave acts on the dielectric non-directionally. The bending or deformation direction of the dielectric changes with the direction of the ultrasonic wave and the polarization electric field. It is not easy to control the polarized electric field to be unidirectional. In this case, the piezoelectric effect may be cancelled throughout the dielectric.

The water pressure caused by mechanical agitation can also act as external stress, leading to the deformation of the piezoelectric material and the corresponding piezoelectric potential. A simple agitated dielectric flow can apply continuous pressure in a single direction of the material, creating a continuously piezoelectric field. Moreover, by adjusting the direction and speed of mechanical stirring, the polarization direction and strength of the material can be affected. Mechanical stirring is a simple way to enhance the piezo-potential. However, it is necessary to exclude the mass transfer effect of ultrasonic vibration and mechanical stirring through comparative tests when studying the promotion effect of piezoelectric potential strength on material application properties under ultrasonic vibration and mechanical stirring.

In pyroelectric and ferroelectric materials, temperature fluctuations trigger polarization and the generation of positive and negative charges for redox reactions. Given that thermal expansion is equivalent to tension, and pyroelectric crystals are necessarily piezoelectric crystals, thermal expansion polarizes the crystal through a positive piezoelectric effect, and the change in temperature causes a slight spatial movement of atoms in the crystal structure, leading to a change in polarization inside the pyroelectric body and a sensible pyroelectric charge on the surface of the pyroelectric material. The pyroelectric effect is divided into two levels, *i.e.*, the primary pyroelectric effect is the heating in the mechanically clamped state, where the volume and shape of the crystal are forced to remain constant. The secondary pyroelectric effect is heated in the mechanical free state and the crystal is strained by thermal expansion, and this strain is superimposed on the first type of effect by generating a potential shift through the piezoelectric effect, and the additional pyroelectric effect is generated due to the coupling of thermal expansion through the piezoelectric effect. Thus, this additional effect is not a true pyroelectric effect, which is called the secondary pyroelectric effect. At lower temperatures, the thermal vibrational energy of the metal ions is reduced due to thermal fluctuations, the ions with particularly low thermal vibrational energy do not have sufficient to overcome the oxygen ion electric field effect, and it is possible to deviate from the equilibrium position to a certain close oxygen ion. Also, the interaction between the dipole moment to deviate from the equilibrium position of the ion in the new equilibrium position is fixed, causing this oxygen ion to exhibit strong polarization, and thus the crystal lengthens in that direction and the cell undergoes a slight distortion. At higher temperatures, the metal ions have a higher thermal vibrational energy, and thus it is difficult to fix them at a position away from the center. Also, the chances of approaching six oxygen ions are equal, the crystal maintains a high symmetry, and the spontaneous polarization is zero, and thus the ferroelectric material loses polarization above the Curie temperature.

Another method to achieve deformation is physical bending. In this case, a piezoelectric material is attached to a cantilever to and stress applied such as periodic external forces and vibrations. This method is more complex than the ultrasonic vibration and mechanical stirring methods. Nonetheless, it provides an accurate model for a mechanistic understanding of the interrelation between piezoelectric electronics and reactivity.

4 The strategies for boosting piezoelectric performance

As mentioned above, the piezoelectric, pyroelectric and ferroelectric properties of piezoelectric materials contribute greatly to the improvement of material performance. Thus, to date, many strategies have been developed to specifically improve these properties, such as nanostructure design, microstructure modulation and surface modification.[48] By promoting a series of studies on the theory and properties of piezoelectric materials, ferroelectric materials have been widely employed in bioapplications.

4.1 Microstructure modulation

4.1.1 Morphological control. In general, microstructure modulation mainly includes the modulation of the microscopic morphology, phase composition, phase transition, microregion, phase interface, surface chemical composition distribution, crystalline segregation, crystal mechanism, molecular structure, chemical state of elements, spatial distribution, electronic energy state, chemical environment around ions and bonding in a material. By adjusting the composition and key parameters of the reaction system, such as acidity and alkalinity, reactant concentration, solvent type, addition of surfactant, use of templates, and calcination temperature, various materials with optimal structures can be obtained. For example, Patrick Braeutigam *et al.* investigated the interdependence among particle size, polarization, and thermocatalytic activity *via* the dichlorofluorescein redox method and demonstrated that the polarization effect of pyroelectric catalysts increases with an increase in particle size and changes in size-dependent phase composition and domain structure, which in turn leads to a size-dependent increase in pyroelectric catalytic activity (Fig. 5A).[49] Bao *et al.* investigated the pyroelectric catalytic performance of $BaTiO_3$ nanowires prepared *via* the template hydrothermal method. Compared with equiaxed nanoparticles, nanowires with elongated polar axes have better pyroelectric catalytic performance, which was verified by finite element simulations. It was shown that the maximum output voltage of nanowires is proportional to their length (Fig. 5B).[50] The length of pyroelectric materials along the polar axis is closely related to the voltage at both ends of the material, and preparing materials with longer dimensions in the polar axis direction is a good way to promote pyroelectric-induced charge carrier separation and improve pyroelectric redox properties. This work provides a research idea for improving the material performance by extending the length of pyroelectric bodies along the polarity axis. The magnitude of the pyroelectric current and potential difference is important for the generation, separation and transfer of pyroelectric charges.

Given that mechanical properties are highly correlated with geometry, the well designed and optimized morphology of a material can positively influence its overall piezoelectric response.[51] In general, microstructural modulation helps to form higher specific surface area and more surface active centers to optimize the effective contact between reactants and materials, thus improving their response performance (Fig. 5C and D).[52] Jia *et al.* demonstrated the decomposition ability of bismuth clathrate nanosheets, nanoflowers and nanospheres under cold and hot excitation at 25–65 °C depending on their surface to volume ratio. The experimental results demonstrated that the nanosphere morphology of bismuth clathrate results in an excellent dye decomposition performance and the hysteresis lines verified its excellent pyroelectric properties. However, according to the combination of mass spectrometry simulations and theoretical analysis by Tang *et al.*, the dependence of nanopiezoelectricity on the shape, size and properties of the surface layer is not entirely responsible for the excellent performance. The atomic fraction of the strain-sensitive Zn–O dipole, the initial volume contraction due to residual surface stress and the surface piezoelectricity are the main physical causes of the shape dependence of the piezoelectric coefficient (cross section). When subjected to small-scale effects, it decreases with an increase in the characteristic size or specific surface area of ZnO nanostructures. Moreover, the higher sensitivity of the nanoribbon volume variation to axial strain has a significant effect on its piezoelectric effect, which is independent of its specific surface area. The above-mentioned results suggest that the nano-piezoelectric properties cannot be completely controlled by the specific surface area (Fig. 5E and F).[53]

4.1.2 Structural control. Generally, it is believed that ideal piezoelectric single crystals exhibit a better performance than piezoelectric ceramics with the same components because they are not affected by grain size, grain boundaries and void fraction. Therefore, the single crystallization of materials is an effective method to improve their piezoelectric performance. However, single crystals are costly and difficult to prepare with a large size. Consequently, the textured synthesis of piezoelectric materials has emerged. Texturing is the use of certain microstructure control to achieve the regular arrangement of the anisotropic grains in the microstructure of structural ceramic materials along specific directions or increase the chance of orientation in these directions, causing them to grow in an orientated way. Essentially, the texturing of lead-free piezoelectric ceramics is an effective means to optimize the microstructure of piezoelectric ceramics by changing their ferroelectric domains from a disordered to ordered arrangement, similar to that of a single crystal, which exhibits anisotropy. Consequently, dense, highly structured ceramics with a controlled microstructure can exhibit superior dielectric and piezoelectric properties in specific directions compared to conventional polycrystalline ceramics. The preparation of textured ceramics has become a unique method to improve the properties of traditional structural ceramics and new preparation technology instead of single crystallization. In the review by Toshio KIMURA, he classified the development characteristics of microstructures into four categories according to their preparation methods including directional solidification of unequal-axis particles, template grain growth, reactive template grain growth, and heterogeneous template grain growth.[54] For example, Peng *et al.* prepared a ⟨001⟩ highly oriented

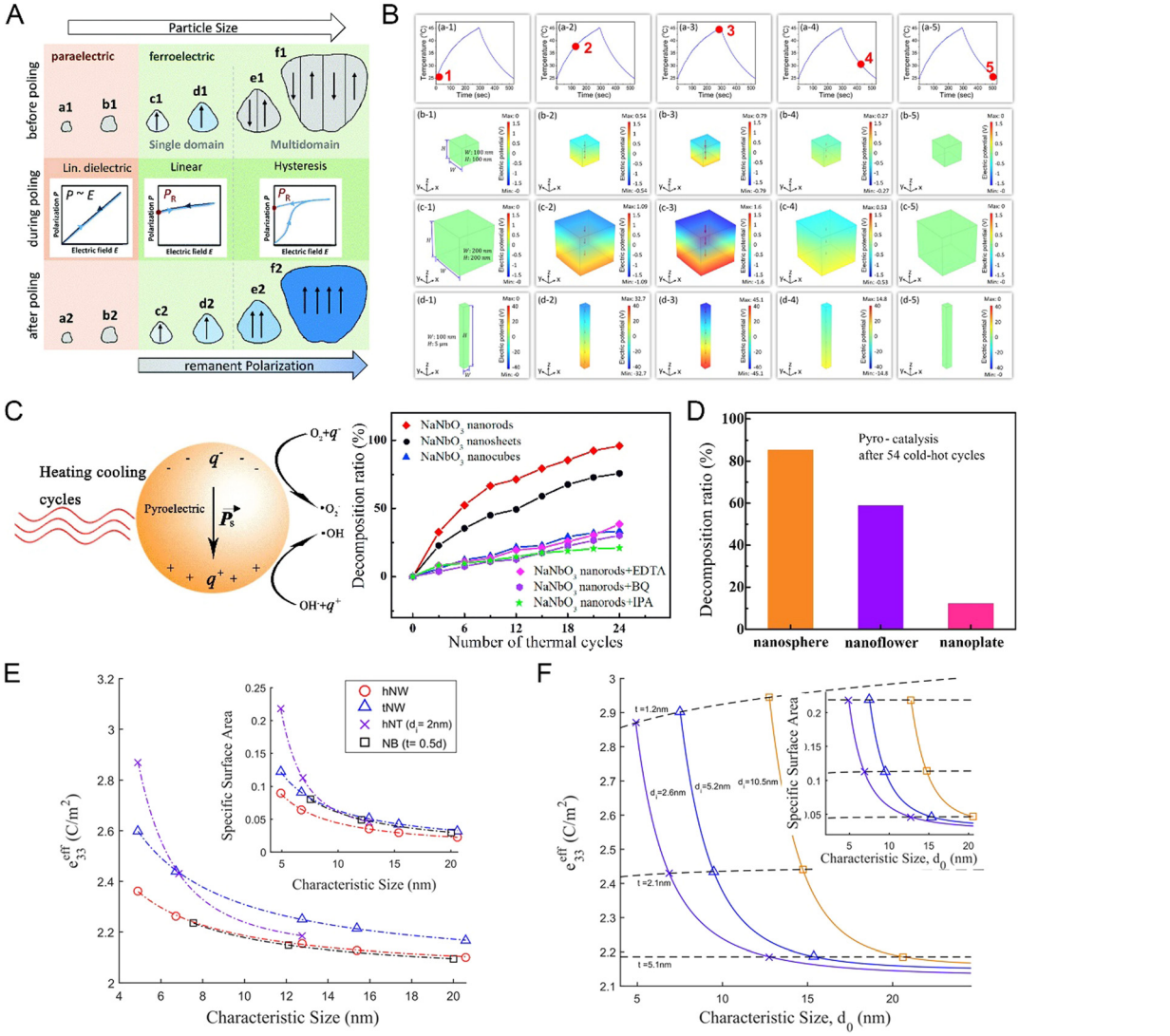

Fig. 5 (A) Schematic diagram of the relationship among particle size, polarization, crystal and domain structure.[49] Copyright 2020, The Royal Society of Chemistry. (B) Pyroelectric potential distribution of BTO nanocrystals with different sizes and morphologies at different temperatures during periodic thermal cycles.[50] Copyright 2018, The American Chemical Society. (C) Effects of $NaNbO_3$ nanoparticle shape and scavenger type on decomposition rate (23–50 °C).[51] Copyright 2018, Elsevier. (D) Pyroelectric catalytic capacity of BiOCl with three morphologies.[52] Copyright 2020, Elsevier. (E) Variation in e_{33}^{eff} and surface area with morphology and size. (F) Variation in e_{33}^{eff} and surface area with size for h-NTs.[53] Copyright 2018, Elsevier.

textured $BiFeGaO_3$–$BaTiO_3$ system *via* the reactive template grain growth method. The effective piezoelectric coefficient, d_{33}, of the textured sample reached 685 pm V^{-1} at 180 °C. The ⟨001⟩ optimally oriented grains reduced the angle between the external electric field and the spontaneous polarization of the sample and decreased the stress difference between adjacent grains, thus enhancing the ability of steering ferroelectric domains under an electric field. The textured sample had more *R3c* phase content than the non-textured sample and a high density of nanodomain structures. The high *R3c* phase content facilitated large lattice displacements under an external electric field, which resulted in higher strain in the textured samples. The high density of nanodomains helped to reduce the domain wall potential barrier, which made the steering of ferroelectric domains easier. In summary, these microstructural modulations finally enhanced the ferroelectric properties of the textured $BiFeGaO_3$–$BaTiO_3$ system.[55]

Polyvinylidene fluoride (PVDF) and its copolymers are typical organic piezoelectric materials. Their unique piezoelectricity, high flexibility, manufacturability, and chemical stability make them candidates for self-powered flexible piezoelectric sensors or energy harvesters, which show great potential for applications in the medical, electronic skin, and motion monitoring fields. However, the piezoelectric constant, d_{33}, of PVDF and its copolymers is only about −30 pCN^{-4}, which is 1/20–1/8 of that of common inorganic piezoelectric materials such as lead zirconate titanate, and thus its piezoelectric performance is still not comparable to that of inorganic piezoelectric materials. To improve the piezoelectric performance of PVDF-based flexible piezoelectric sensors, researchers have

proposed many improved methods. In this case, the main methods include increasing the piezoelectric constant, d_{33}, by improving the crystallinity, β-phase content and molecular chain orientation of PVDF and its copolymer films, or to compounding with inorganic piezoelectric materials, retaining the high flexibility of PVDF and improving the piezoelectric constant.

4.1.3 Doping. Doping is a major tool used to alter the properties of materials and satisfy the specific need for piezoelectric properties in practical applications, where piezoelectric materials are modified by appropriate doping in their basic composition.[56,57] The guest molecules encapsulated in the crystal usually reduce their symmetry by generating polar domains, which enhance the polarization in the doped crystal, where the various impurities added are mostly transition metal ions. For example, Li *et al.* used scanning Kelvin probe force microscopy (SKPM) to compare the surface potentials of potassium–sodium niobate (KNN) and KNNSe, as well as that of KNN and polarized KNN (P-KNN). The results showed that the polarization process enhanced the intensity of the internal electric field (Fig. 6A). Meanwhile, the piezoelectric properties of P-KNN and Se-doped KNN (P-KNNSe) were measured using a piezoelectric d_{33} detector, which detected an increase in the piezoelectric constant of P-KNNSe compared to P-KNN under the same polarization condition. It indicated that the addition of selenium enhanced the piezoelectric properties and natural electric field strength of the surface of P-KNN, which exhibited piezoelectric stability in physiological solution (Fig. 6B). This can be attributed to the optimized phase composition and the construction of a homomorphic phase boundary. Therefore, polarization and Se doping are beneficial to improve the surface potential, and their combination results in a synergistic effect. The results of anti-cancer experiments revealed that a strong electric field increases the cellular membrane permeability. The anti-cancer element selenium may be released at this time, leading to an increase in intracellular reactive oxygen species, mitochondrial damage, and eventually activation of the caspase-3 apoptotic pathway, resulting in the effects of wireless

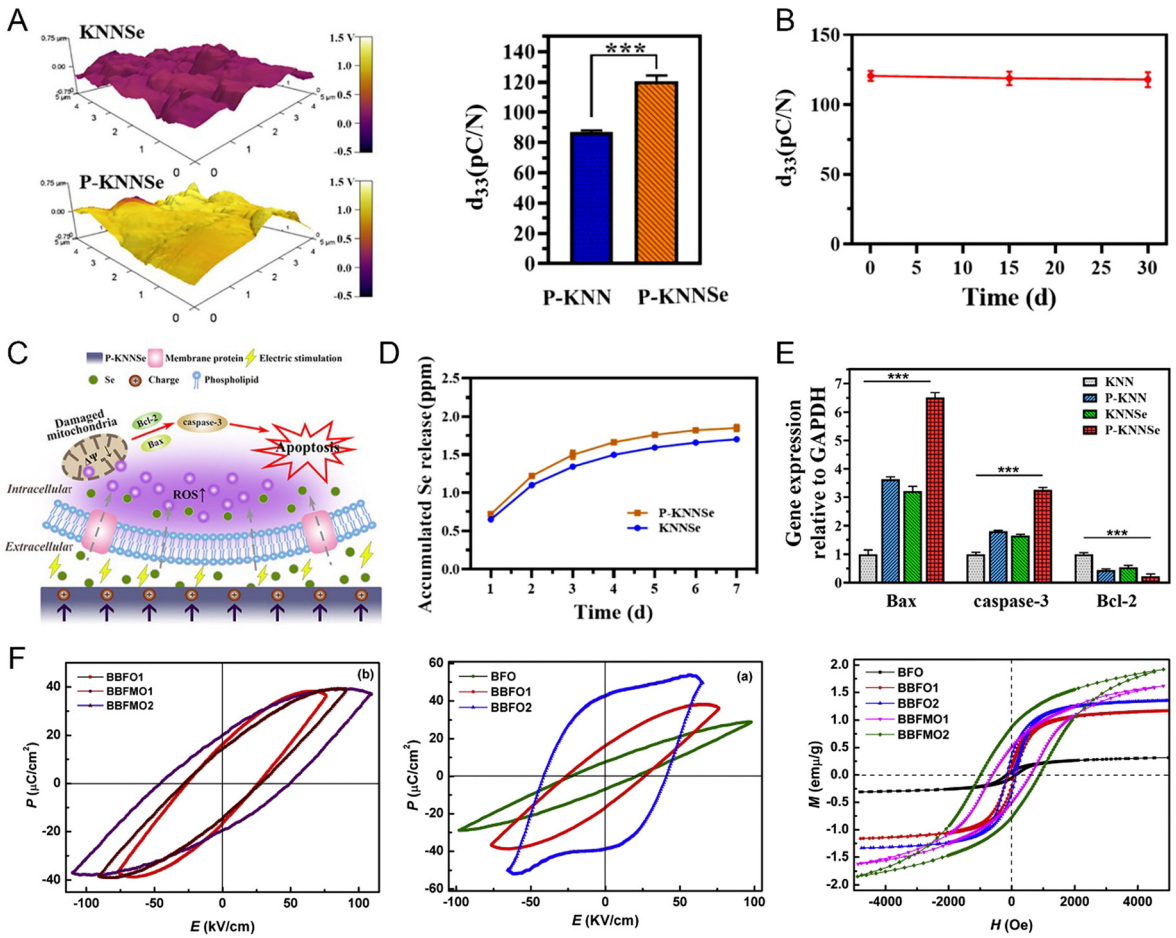

Fig. 6 (A) Surface potential before and after polarization examined using SKPM, and piezoelectric coefficient before and after Se doping measured using piezoelectric d_{33} tester. (B) Piezoelectric constant of P-KNNSe immersed in cell culture medium for 0, 15, and 30 days. (C) Schematic diagram of anti-tumor effect of wirelessly controlled P-KNNSe piezoelectric ceramics. (D) Accumulated Se release curve in neutral PBS buffer (pH 7.4). (E) Gene expression relative to GAPDH in tumor cells after 2 days of incubation with different samples.[58] Copyright 2020, the American Chemical Society. (F) Ferroelectric hysteresis loops and magnetic hysteresis loops of pure $BiFeO_3$ (BFO), Ba-doped BFO ceramics (BBFO), and Mn-doped BBFO (BBFMO).[61] Copyright 2016, Elsevier.

electrotherapy and chemotherapy (Fig. 6C). The released Se induced intracellular ROS production. The cumulative release curve of Se in PBS buffer (pH 7.4) showed that polarization contributes to Se release (Fig. 6D). The detection of apoptosis-related genes showed the decreased expression of the antiapoptotic Bcl-2 gene, increased expression of the pro-apoptotic Bax gene, and enhanced caspase-3 activity of the downstream Bax gene. This indicates that the addition of selenium and the action of a strong electric field contribute to inducing apoptosis (Fig. 6E). Moreover, the cytotoxicity results showed that the functionalized implant is not toxic to normal tissue cells and has good biocompatibility.[58] Both the A- and B-site of KNN-type piezoelectric systems can be doped, where the low energy level and conduction band of the KNN system are shifted to a lower energy direction and the band gap is narrowed after A-site ion doping. When the A-site ion is replaced by a smaller radius ion or a complex ion cluster in the KNN lattice, the Nb–O octahedron collapses toward the center. However, after B-site ion doping in the KNN system, the whole energy band shifts to the high-energy direction, and when the B-site ion is replaced by ions with a larger radius or composite ion group, the Nb–O octahedron will expand. The structural transformation of the KNN system from orthogonal to tetragonal phase makes the shifting the electric domain wall easier and enhances the piezoelectric properties of KNN.[59] Astita Dubey *et al.* synthesized barium–Mn co-doped $BiFeO_3$ nanoparticles *via* a modified sol-gel method, which induced limited coupling of $BiFeO_3$ by doping reagents, while the nano-size constraint could also limit the formation of magnetic pendulums in BFO. The doped nanoparticles still possessed a chalcogenide structure with *R*3*c* symmetry, retaining their ferroelectric behavior and with an increase of 1 order of magnitude in the residual magnetization intensity. The combination of the enhanced magnetization intensity with the large ferroelectric polarization increases the possibility for the application of these nanoparticles in spintronics or cell and tissue stimulation, enabling their feasible application in computer memory and thermal cancer therapy.[60] Wen *et al.* also verified that ionic co-doping is an effective way to modulate the room temperature ferroelectric and ferromagnetic properties of $BiFeO_3$ (Fig. 6F). Also, they demonstrated that the appropriate doping ratio of Ba and Mn ions has an important contribution to the microstructural distortion and transformation of $BiFeO_3$, which can improve its ferroelectric properties.[61] Cui and Park *et al.* doped Na^+ in $KNbO_3$ to form $Na_{1-x}K_xNbO_3$ hybrid powder. Firstly, they polarized the material before and after doping by the corona polarization method, and then obtained the effect of different Na^+ doping amounts on the ferroelectricity of $Na_{1-x}K_xNbO_3$ powder by pressure electric microscope (PFM) test of the hysteresis echo line. The maximum polarization intensity was obtained when the Na^+ doping amount was 0.5 mol, indicating that the best ferroelectricity of $Na_{0.5}NbO_3$ was achieved.

It is well known that defect engineering is a general method to adjust the electronic structure and properties of materials. Lu *et al.* induced the reorientation of hydroxyl dipoles in hydroxyapatite (HAP) through oxygen vacancies (OV), and the number and orientation of hydroxyl groups in the HAP lattice directly led to the enhancement of its piezoelectric properties. The piezoelectric current output signals of HAP and OVHAP driven by mechanical stirring were tested using an electrochemical workstation.[62] As shown in Fig. 7A–D, OVHAP produced a more obvious piezoelectric discharge signal than HAP under magnetic stirring. Notably, OVHAP-2 h had the highest electrical signal output among the catalysts. Meanwhile, the catalytic experimental results showed that the piezoelectric catalytic removal efficiency of bisphenol A by hydroxyapatite with a moderate oxygen vacancy concentration (OVHAP-2 h) was 98.43% within 12 min, and its degradation kinetic constant was almost 4 times higher than that of the pristine HAP. This is related to the parallel arrangement of oxygen vacancies and hydroxyl dipoles at moderate concentrations. Wang *et al.* developed efficient acoustic sensitizers based on barium titanate for ultrasound (US) stimulation against ovarian tumor cells,[63] with the idea of reducing the band gap by oxygen defect engineering and bismuth (Bi) modification of Schottky junctions, consequently improving the piezoelectric properties and electron–hole separation of barium titanate (BTO). The oxygen defects and Bi doping in OB and OBB and their resulting disorder in the BTO lattice, were confirmed by XRD spectra, electron paramagnetic resonance (EPR), XPS full spectra, and O 1s spectra. OB is a BTO-doped oxygen vacancy and OBB is a BTO-doped oxygen vacancy and Bi element. The results of the piezoelectric characterization of nanoparticles (NPs) showed that the hysteresis return line of OBB was relatively narrow compared to that of BTO, indicating that the phase reversal of OBB could be caused even when the relative voltage change was small. Meanwhile, the smaller the voltage change of the butterfly curve of the OBB, the larger the amplitude (Fig. 7E–H). These results suggest that oxygen defect engineering reduces the band gap and bismuth (Bi) modification of Schottky junctions improves the piezoelectric performance of BTO. In addition, atomic-scale-thick $Bi_4Ti_3O_{12}$ nanosheets with abundant surface oxygen vacancies were prepared by Huang *et al.* Piezoelectric force microscopy, piezoelectrochemical tests and finite element simulations showed that the atomic-scale thickness and oxygen vacancies increased the piezoelectric coefficient, which enhanced the piezoelectric polarization and accelerated the charge separation and reaction kinetics.[64,65]

4.2 Surface and interface regulation

The separation of charge carriers and the adsorption of reactants are crucial for the generation of radicals during oxidation–reduction reactions. Therefore, modification strategies to modulate surfaces and interfaces can also improve the polarization of materials. Thus far, the main approaches to modulate the surface and interface of materials include surface conditioning, precious metal deposition, heterostructure building and surface modification of organic molecules. Due to the plasma effect and high functionalities of metals, the deposition of noble metals on the surface of piezoelectric semiconductors can improve the charge separation efficiency, which leads to excellent redox reaction performances.[66–68]

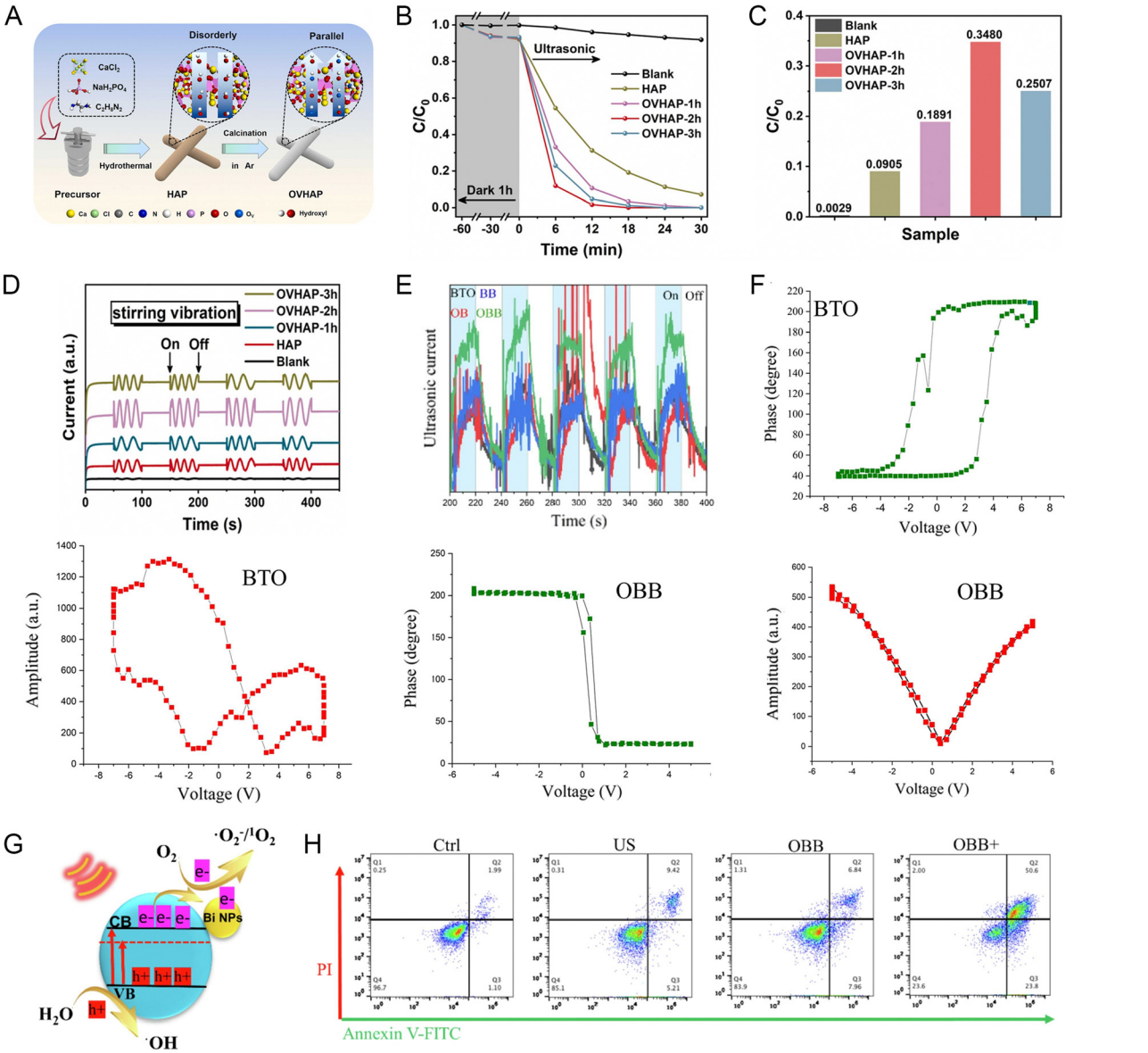

Fig. 7 (A) Schematic diagram of OVHAP synthesis process. (B) Degradation efficiency of bisphenol A and (C) corresponding degradation kinetic rate constants (min^{-1}). (D) Piezoelectric discharge signal under agitation (1200 rpm).[62] Copyright 2020, Elsevier. (E) Photocurrent density curves under US. (F) Phase and amplitude curves measured by PFM. (G) Mechanism diagram of enhanced acoustic catalytic activity of OBB. (H) Flow cytometry results.[63] Copyright 2022, Elsevier.

It is well known that $BiVO_4$ has piezoelectric properties, but its piezoelectric properties are weak, and thus the $BiVO_4$ material alone has not been widely developed. Long *et al.* used a urea-assisted deposition–precipitation method to modify nano-Au on the surface of bismuth vanadate (Au/$BiVO_4$) to produce a piezoelectric catalyst (Fig. 8).[67] Au/$BiVO_4$ has different polarization directions and possess distinct and randomly distributed ferroelectric domains. This was confirmed by piezoelectric force microscopy tests. In addition, the tests yielded distinct butterfly-shaped amplitude loops, a well-known property of ferroelectric materials, which also demonstrated the excellent ferro/piezoelectric properties of Au/$BiVO_4$. Thus, noble metal deposition is an effective strategy to enhance the activity of piezoelectric catalysts.

The selection of semiconductors with suitable energy band structure to construct heterojunctions also seems to be a more desirable approach than the use of noble metals to prevent the compounding of positive and negative charges generated at high temperatures and to extend the charge lifetime. To improve the piezoelectric properties of bio-piezoelectric polymers, the integration of nanofillers such as barium titanate, zinc oxide, metal nanoparticles, graphene oxide and carbon nanotubes in the polymer matrix has been proven to be an effective approach. For example, the addition of nanofillers to polyvinylidene fluoride produces electrostatic interactions with the surrounding polyvinylidene fluoride chains and affects the chain orientation, thereby improving the overall piezoelectric

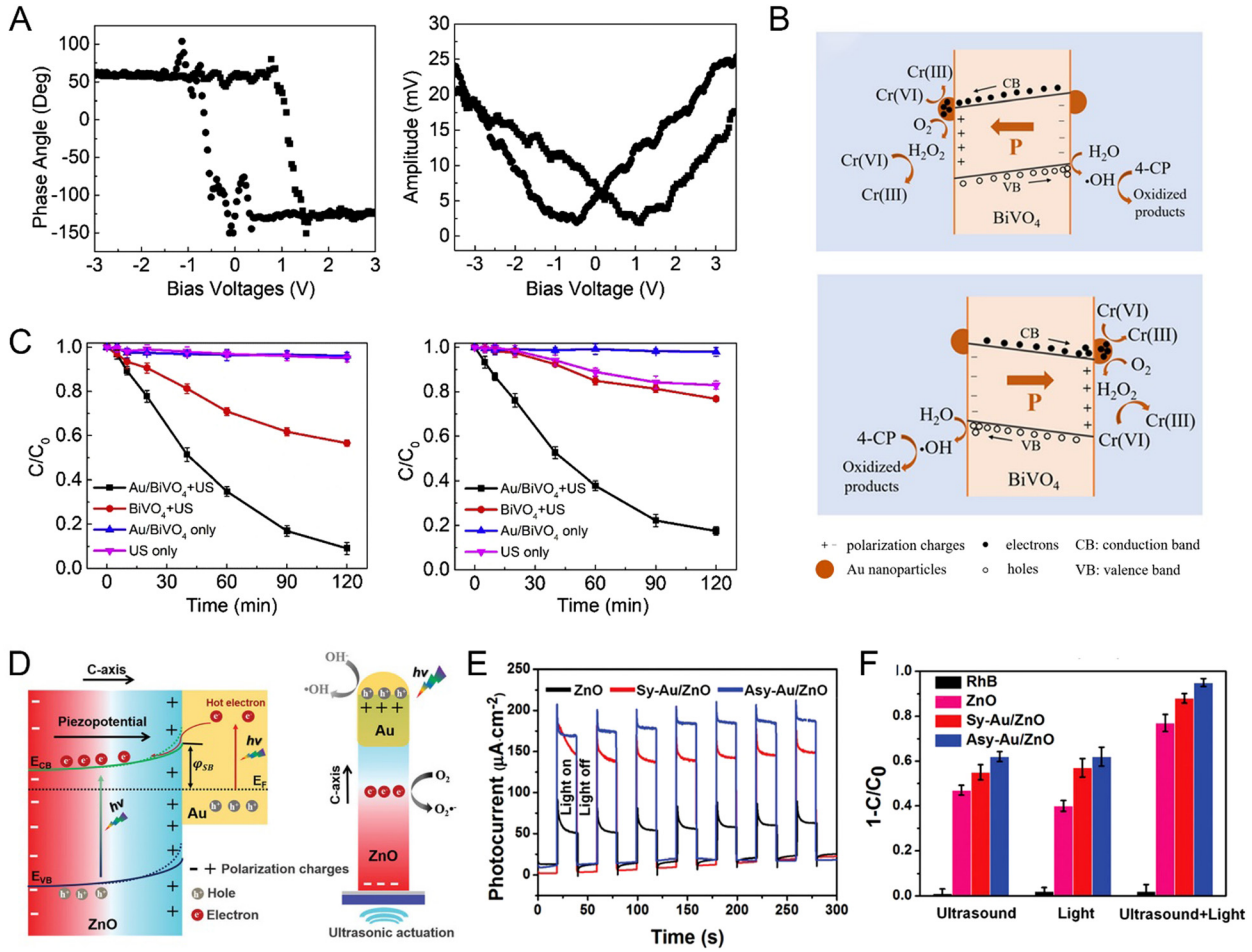

Fig. 8 (A) Phase hysteresis loop and amplitude butterfly loop for Au/$BiVO_4$. (B) Effect of energy band bending in Au/$BiVO_4$ piezoelectric catalysis and the proposed mechanism. (C) Removal of 4-CP and Cr(VI) in different processes.[67] Copyright 2019, Elsevier. (D) Enhanced catalytic mechanism of piezoelectric effect and heterojunction structure induced by light and US. (E) Photocurrent density under full-spectrum irradiation. (F) Degradation performance after different treatment processes.[66] Copyright 2020, Wiley-VCH.

response of the composite. For example, Deng *et al.* improved the piezoelectric properties of PVDF films by wrapping ZnO nanospheres in PVDF nanofibers. The ZnO nanospheres not only enhanced the local electric field during the electrostatic spinning process and increased the proportion of β-phase polyvinylidene fluoride crystals, but also had a synergistic effect with the polyvinylidene fluoride nanofibers to promote the piezoelectric properties of the composite. In addition, the piezoelectric properties of the composites could be easily controlled by adjusting the weight ratio of ZnO nanospheres and polyvinylidene fluoride polymers. Moreover, organic molecular decoration is also a feasible strategy to improve the piezoelectric properties. Li *et al.* used a simple oil bath method to modify 2-mercaptobenzimidazole (2MBI) with strong hole acceptor ability on the surface of hexagonal cadmium sulfide (CdS) nanorods with the pyroelectric effect. 2MBI can amplify the pyroelectric response of CdS due to its good bonding properties and strong hole acceptor ability (Fig. 9).[69] The interfacial interaction increased the piezoelectricity of CdS, which caused the piezoelectricity of CdS-2MBI to be stronger than that of CdS and enhanced the separation of pyroelectric charges. The mechanistic analysis showed that the thermocatalytic hydrogen precipitation activity of CdS-2MBI was significantly increased by about 5 times that of CdS alone under the thermal cycling conditions of 25–55 °C, where a large number of holes was attracted by 2MBI to release protons after lactic acid oxidation.

Numerous studies have demonstrated that microstructural modulation is an effective strategy to improve the piezoelectric, pyroelectric and ferroelectric properties. This approach is mainly focused on material design, while piezoelectric, pyroelectric and ferroelectric performance enhancement can also be achieved through the development of technological methodologies such as corona polarization, annealing post-treatment, chemical-pressure, and introduction of an electron-blocking layer between the negative tribomaterial and electrode.[70,71]

4.3 Polarization enhancement

As mentioned above, the degree of polarization plays a crucial role in the redox reaction process, given that it is the driving force for the separation of electrons and holes.[72] All materials

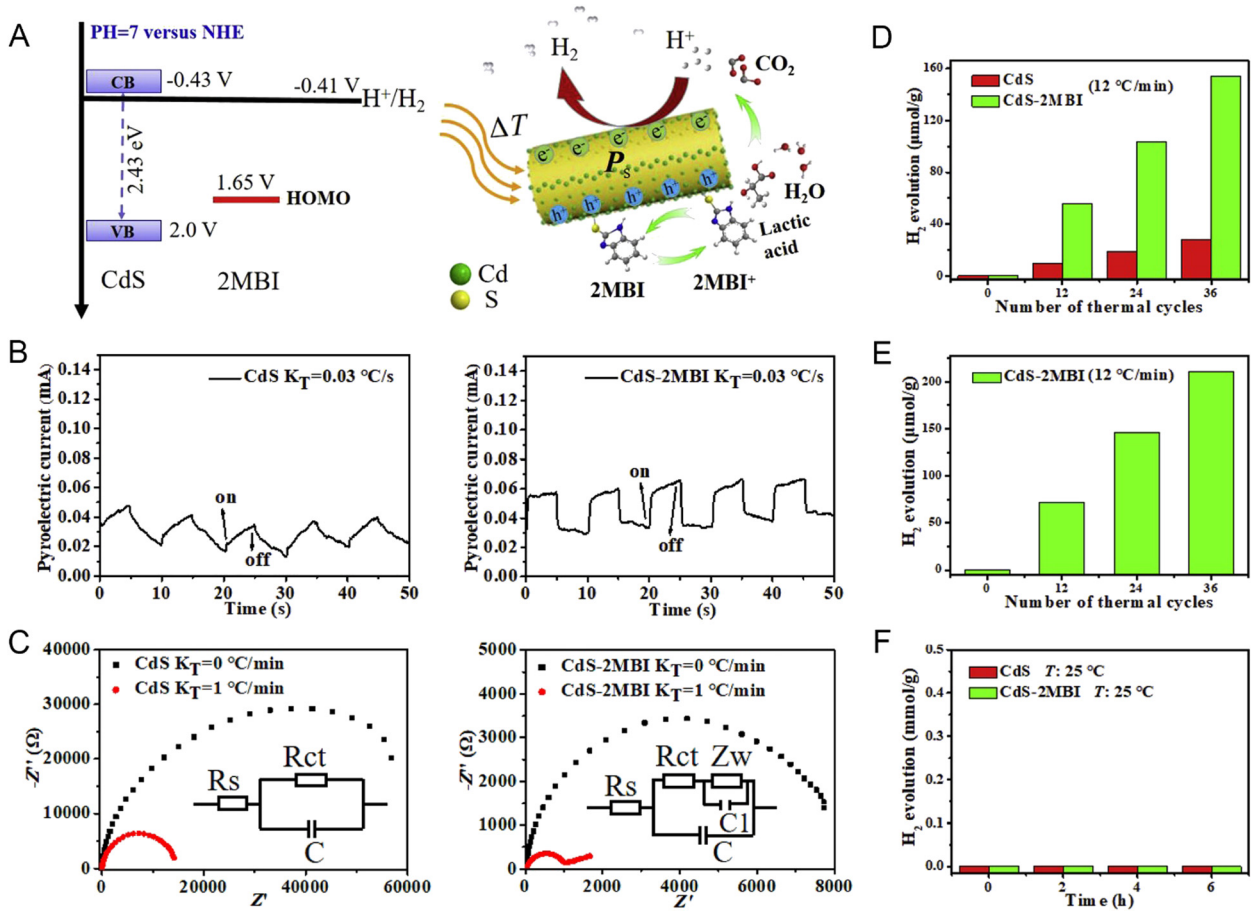

Fig. 9 (A) Energy level diagram for CdS nanorods and 2MBI and schematic of pyroelectro-catalytic hydrogen evolution. (B) Time-dependent pyroelectric currents of CdS and CdS-2MBI. (C) Electrochemical impedance spectra Nyquist plots of CdS and CdS-2MBI at the heating rate of 0 and 1 °C min^{-1}, respectively. Pyroelectro-catalytic H_2 evolution of (D) CdS and CdS-2MBI at 25 −55 °C, (E) CdS-2MBI at 25 −70 °C, and (F) CdS and CdS-2MBI at 25 °C under irradiation with a light intensity of 0.05 mW m^{-2}.[69] Copyright 2020, Elsevier.

can be polarized by an external electric field. Also, pyroelectric and ferroelectric materials can be spontaneously polarized under certain conditions. However, the bound polarization charge is readily shielded by compensating charge carriers, leaving the remaining polarization of the material almost zero. Changing the temperature and applying an external electric field can increase the polarization intensity, which increases with temperature and electric field, thus promoting redox reactions.[73] Therefore, appropriately controlling the degree of polarization is an effective way to enhance redox reactions. There are two types of polarization enhancement approaches, where the first type is to pre-polarize the material before application, including corona polarization and post-annealing treatment to increase its residual polarization. For example, Li *et al.* compared the dye decomposition rate of barium titanate before and after electric field polarization (Fig. 10A–C).[74] The results showed that the dye decomposition rate of the polarized $BaTiO_3$ catalyst reached about 56% under a 5.00 kV mm^{-1} polarization electric field, which was more than 7 times that of the unpolarized $BaTiO_3$. This proved that the polarization treatment has a great influence on the effect of pyroelectric catalysis. The residual polarization will survive for some time. Vaisha *et al.* also verified that polarization significantly affects the electron–hole pair separation in the catalytic reaction and the polarized samples performed much better in the catalytic reaction than the unpolarized samples.[75] In the processing and preparation of ferroelectric ceramics, the accompanying cooling process can result in a decrease in the saturation and residual polarization intensity and piezoelectric coefficient of the material due to the internal stresses generated in it. The annealing treatment homogenizes the material structure and composition, effectively releasing and reducing the internal stresses and making it easier for the ferroelectric domains to stretch and rotate under an alternating electric field, thus increasing the saturation polarization intensity and piezoelectric coefficient. Alternatively, the composition of the material tends to be homogeneous after annealing treatment and the original 1:1 ordered chemical microdomains due to chemical inhomogeneity will be reduced in scale due to the improvement in chemical homogeneity. Also, the polarization vectors of the reduced scale microdomains will be more easily oriented and distributed under the action of an external field, thus enhancing the polarization of ferroelectric materials. For example, the Ichiro Fujii group verified the significant enhancement in the piezoelectric and ferroelectric

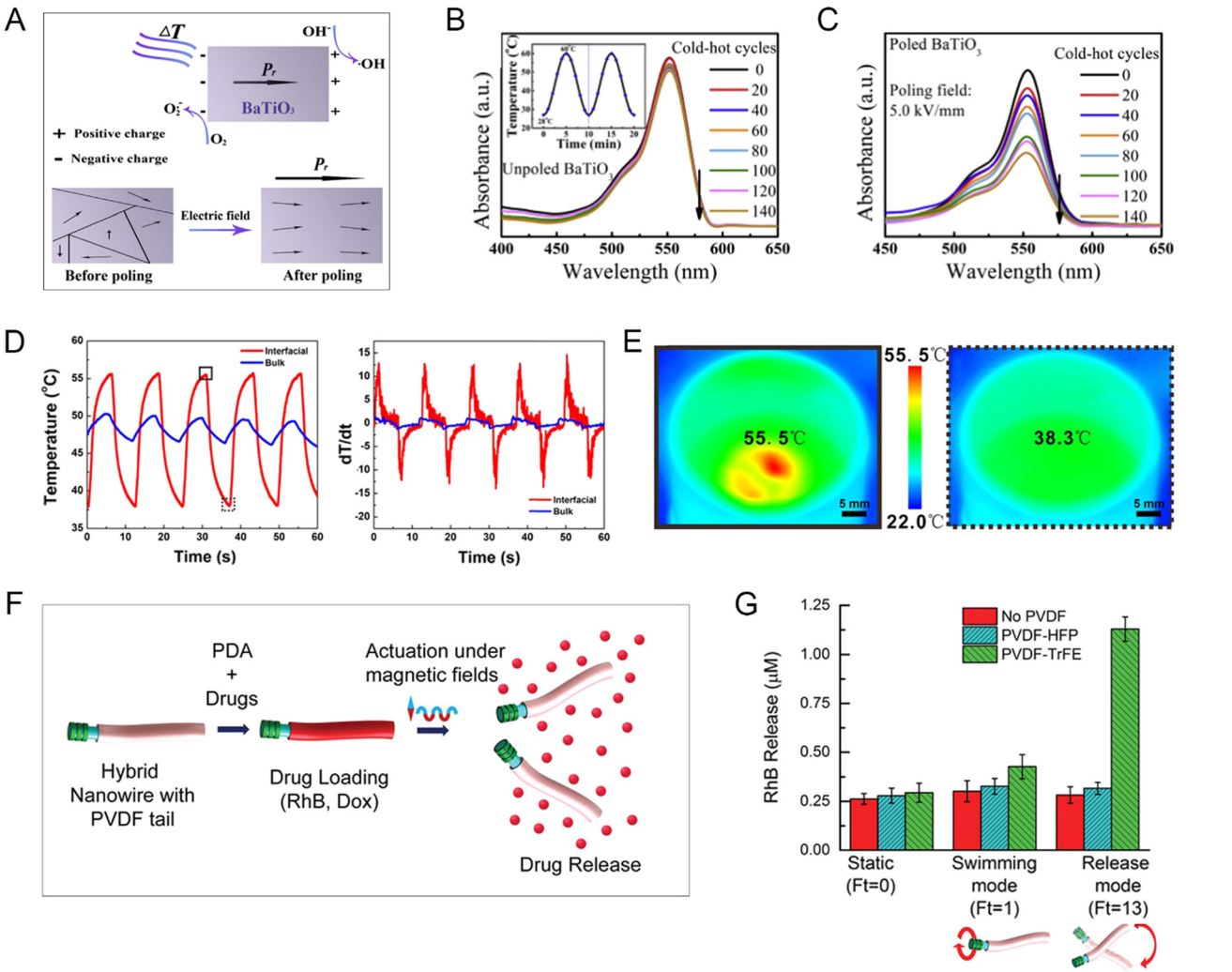

Fig. 10 (A) Pyroelectric catalytic mechanism of $BaTiO_3$. Degradation of RhB dye by $BaTiO_3$ before and after polarization (B) 0 kV mm^{-1} and (C) 5.0 kV mm^{-1}. The inset in (B) shows the relation curve of dye temperature and time.[74] Copyright 2020, Elsevier. (D) Temperature cycle curves of pyroelectric materials and the corresponding dT/dt curves. (E) IR images of the maximum and minimum temperatures in the interfacial system.[77] Copyright 2018, the American Chemical Society. (F) Synthesis and functionalization of hybrid nanoeel for magnetically triggered controlled drug delivery. (G) Release of RhB under different magnetic actuations (n = 5).[79] Copyright 2019, Wiley-VCH.

properties of Bi-based lead-free piezoelectric ceramics by heat treatment.[76] The piezoelectric properties of pure KNN ceramics are poor and attempts can be made to improve their sintering behavior to improve specific properties such as piezoelectricity or coupling constants, such as hot-pressure sintering and discharge plasma sintering processes. The second category is to modulate the polarization intensity of the material during its application by modulating the temperature, US or electric field by certain means. For example, Deng *et al.* prepared composite nanopreparations by compounding pyroelectric materials with a photothermal component of low thermal conductivity, and then used an optical chopper-modulated solar light source periodically to regulate the dT/dt of the materials, confirming that rapid temperature fluctuations increased the polarization of the pyroelectric materials. Further, to fully utilize thermal energy and improve the efficiency of pyroelectric redox reactions, pyroelectric material systems that are more sensitive to changes in temperature are required (Fig. 10D and E).[77] In addition, Zhang *et al.* reported for the first time that $Bi_4Ti_3O_{12}$ generated abundant superoxide radicals and hydroxyl radicals under US irradiation with generation rates of 6.4 and 2.4 μmol g^{-1} h^{-1}, respectively, and that US can drive the material to produce a piezoelectric semiconductor coupling process that converts mechanical energy into electrical energy.[78] The positively correlated ultrasonic frequency-enhanced piezoelectric properties are responsible for the efficient degradation of $Bi_4Ti_3O_{12}$. These findings undoubtedly unveil a new horizon of materials with the potential environmental applications of photocatalysis and piezoelectric catalysis. The piezoelectric catalytic properties and morphology-dependent catalytic activity of $Bi_4Ti_3O_{12}$ were also revealed in this work, and photocatalytic degradation experiments on phenol showed that the $Bi_4Ti_3O_{12}$ microspheres prepared *via* the hydrothermal method exhibited optimal photodegradation. The degree of binding of a material to the

surface reactants depends largely on its electronic structure and an external electric field can not only polarize a dielectric material and enhance its polarization, but also affect its semiconductor electronic structure and electric dipole. Therefore, the electronic structure of a material can be effectively modulated by an external electric field, which in turn enhances its redox reaction performance. In additional, an alternating external electric field can be coupled with a magnetic field to jointly tune the polarization of the system. For example, Fajer Mushtaq *et al.* simulated electric eels to develop soft hybrid nanorobots (Fig. 10F and G), using piezoelectric soft tails deformed by a rotating magnetic field to cause changes in their polarization.[79] The magnetic coupling piezoelectric effect was used to enhance the electrostatic field to achieve the on-demand release of therapeutic drugs.

5 Applications of piezoelectric nano-biomaterials in diagnosis and treatment

Attempts to address the biomedical challenges faced by traditional antitumor medical approaches have led to the development of everything ranging from nanomedicine carriers to novel nanomedicines, which hold great promise for improving the efficacy and reducing the toxic side effects of drugs. As an emerging product generated by the combination of nanotechnology and medicine, nanomedicines play an inescapable role in the fields of tumor prevention, diagnosis and treatment. Nowadays, piezoelectric nanobiotics have great potential for new drug synthesis, drug delivery and medical imaging based on their unique physicochemical properties, which have provoked extensive and in-depth research.[80]

5.1 Drug delivery

Chemotherapy nanodrug carriers are usually made of natural or synthetic inorganic/organic materials, which have the following advantages over traditional chemotherapy monodrugs: (1) they protect monodrugs from the physiological environment during distribution and prolong the blood half-life of drugs. (2) They reduce the impact of monodrugs on normal tissues and reduce drug side effects. (3) They precisely respond to changes in the local environment, deliver drugs on demand and prevent the release of non-target drugs. (4) They maximize the drug efficacy. (5) They achieve precise and minimally invasive or non-invasive treatment. (6) They achieve co-delivery of multiple drugs or contrast agents for the purpose of treatment integration. These advantages are also the goals and challenges pursued by researchers for the development of new nanodrug carriers.

In view of these goals, piezoelectric materials are also promising in the field of multi-functionalized drug carrier development to further address the challenges of systemic toxicity, improved internal transport stability, targeted delivery, and postoperative relapse of traditional chemotherapy monotherapeutics (Table 2). The surface charge of a material regulates the cell membrane permeability or activates immune pathways to induce cell death, *etc.*[81–83] For example, Peng *et al.* developed a piezoelectric single crystal ultrasonic transducer (mass 0.076 g) with a diameter of only 2.2 mm based on piezoelectric ceramics. The transducer based on the laminar flow model generated acoustic flow, and then promoted the release of drugs at specific locations in the GI tract through the generated acoustic waves combined with an endoscope.[84] The transducer exhibited an electromechanical coupling coefficient

Table 2 Application of piezoelectric materials in drug delivery

Materials	Size	Operating principle	Outcome	Ref.
Nutlin-3a-ApoE-P(VDF-TrFE) (PNPs)	Spherical nanoparticles (115 ± 20 nm)	US stimulation activates remotely, induces drug release, and transmits anticancer electrical signals locally.	Chemotherapy + chronic piezoelectric stimulation activates apoptotic and anti-proliferative pathways in drug-resistant GBM cells, induces cell necrosis, inhibits tumor migration, and reduces cell invasiveness.	85
P(VDF-TrFE)/Ni nanoring-PPy nanowires	Piezoelectric Nanoeels	Magnetic manipulation for locomotion (5–15 mT, 1–16 Hz) and pulsatile drug release (10 mT, 7 Hz)	35% Human epithelial breast cancer cell death	79
FeGa@P(VDF-TrFE)	Core–shell nanowires (≈250 nm)	3D propulsion actuated by conical rotating magnetic field	≈40% Cancer cell death	86
$CoFe_2O_4$@$BaTiO_3$-PTX	Core–shell nanosphere (≈30 nm)	Drug delivery to cancer cells *via* DC electric field (≈100 Oe), AC electric field (≈50 Oe, 100 Hz) release on demand	Only the mice treated with PTX-loaded magneto-electric nanoparticles (15/200 μg) in a field for three months were completely cured.	87
BTO–DOX nanoparticles	Nanosphere (≈285 nm)	Co-Incubation of DOX–BTO or DOX alone with SH-SY5Y neuroblastoma cells at different concentrations.	Enhanced doxorubicin internalization due to complexation with BTO nanoparticles. Significant cytotoxicity on SH-SY5Y cells. Enhanced cellular internalization of free drug, showing significant cytotoxic effects on SH-SY5Y neuroblastoma cells relative to free DOX, and excellent biocompatibility.	88
ZnO–Gd–DOX	Nanodots (≈3.5 nm)	DOX release in tumor acidic environment; imaging with strong red emission at 600–800 nm.	Remarkable decrease in tumor volume in BxPC-3 nude mice.	89
BTO-TfR	300 nm diameter size	US stimulation activates remotely (1 W cm^{-1}, 1 MHz). Single ultrasound stimulation was performed for 1 h for 4 days.	US remotely interferes with Ca^{2+} and K^+ homeostasis and affects mitotic spindle organization, reducing multidrug resistance in cancer.	90

of 0.36, center frequency of 6.9 MHz, and 6 dB bandwidth of 23%. The results of *in vitro* ultrasound permeation experiments showed that the ultrasound transducer activated at a duty cycle of 60% at 40 Vpp, and the gastric mucosal permeability to bovine serum albumin increased by approximately 5.6-fold, demonstrating that the ultrasound transducer promoted drug permeation in the gastric mucosa. This work provides an ideal treatment option for patients with coagulopathy or unresectable tumors and addresses the obstacle that existing targeted drug release medical devices are too large to be used in gastric endoscopy due to the fact that the tissue biopsy channels are less than 3 mm in diameter. Accordingly, the piezoelectric single crystal ultrasound transducer offers the possibility to improve the drug concentration and bioavailability at the location of lesions in major gastrointestinal diseases.

However, the inconvenience of carrying external devices and the secondary damage to the patient by inserting electrodes limit their application in internal diseases. Therefore, radiochemotherapy using a combination of anticancer drugs and intrinsic electric fields may be a good candidate to solve these problems. The most representative aggressive primary brain tumor, glioblastoma multiforme (GBM), was used as a model due its complex genetic heterogeneity, drug resistance and blood-brain barrier (BBB) limitations. Ciofani *et al.* proposed an anticancer approach based on US-responsive drug-loaded organic piezoelectric nanoparticles (Fig. 11A–C).[85] Piezoelectric hybrid lipid–polymer nanoparticles were developed, with which a non-genotoxic drug (Nutlin-3a) was encapsulated and functionalized by peptides (ApoE) to enhance its ability to cross the blood-brain barrier. This anticancer nanoplatform could be remotely activated by ultrasonic mechanical stimulation to induce drug release and local delivery of anticancer electrical signals. Under US stimulation, the nanocarrier combined chemotherapy with chronic piezoelectric stimulation to activate apoptotic and anti-proliferative pathways in drug-resistant glioma cells, induce cell necrosis, and promote apoptotic and necrotic events, while inhibiting tumor migration and reducing cell invasiveness. Moreover, the important GO terms involved in this combination therapy are also the inhibition of cytokinesis and promotion of autophagy and cell adhesion pathways, as shown by the results of proteomic analysis. This wirelessly activated anticancer effect paves the way for a less invasive, more focused and effective therapeutic strategy, a finding that will open up new perspectives in nanomedicine for the remote treatment of brain cancer and neurodegenerative diseases. This combination of piezoelectric pulses and anti-cancer drugs is known as electro-chemotherapy, which is currently used in clinical practice to treat different types of skin and subcutaneous cancers. Based on its high anticancer activity and therapeutic localization, more efforts have been recently devoted to

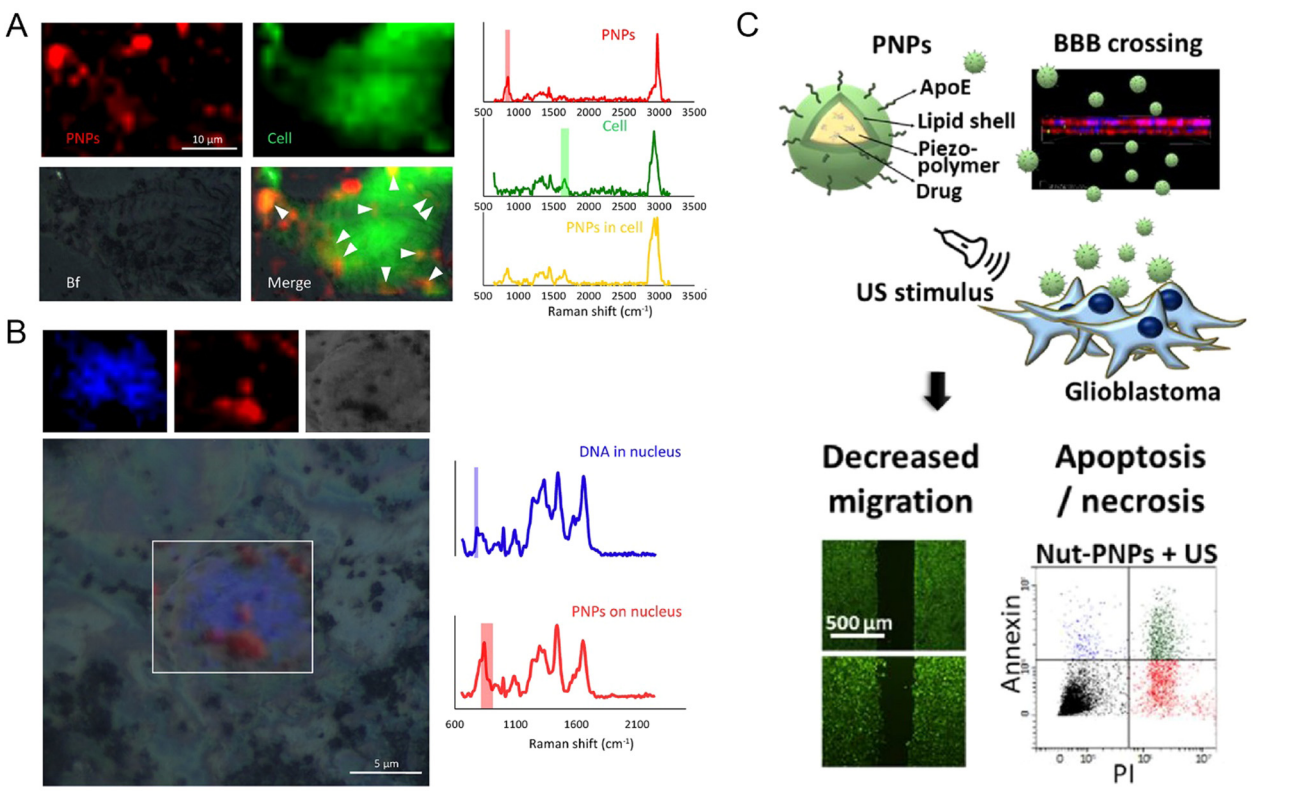

Fig. 11 (A) Imaging of piezoelectric nanoparticles (PNPs) and T98G cells by confocal Raman microscopy without label-free interaction after incubation for 24 h. Arrows indicate internalized nanoparticles. (B) High-resolution confocal Raman microscopy imaging and Raman spectra of PNPs and nuclei. (C) Schematic diagram of PNP structure. Laser confocal images and flow cytometry results of T98G cells stained with calcein for 0 and 24 h.[85] Copyright 2022, Elsevier.

electrochemotherapy. Under electrochemotherapy, the permeability of cell membranes is altered by the additional application of an electric field through appropriate electrodes to improve the uptake of drugs by the cells. This approach ensures a lower drug dose and achieves better therapeutic results. Also, Ning *et al.* were motivated to develop implantable biomaterials with anti-cancer ability and good bioactivity by preventing tumor underway to expand its use for the treatment of internal recurrence after surgery and repairing the defects caused by surgery.[58] The doping of potassium sodium niobate piezoelectric ceramics with the effective anti-cancer element selenium successfully realized the wireless combination of electrotherapy and chemotherapy. It was demonstrated that the selenium-doped piezoelectric implant could significantly promote the apoptosis of osteosarcoma cells *in vitro* by increasing intracellular reactive oxygen levels, causing mitochondrial damage, and thus triggering the caspase-3 pathway. This method uses piezoelectric materials for chemotherapy by additionally applying an electric field through appropriate electrodes to alter the permeability of cell membranes, thereby improving the uptake of drugs by cells. This method ensures a lower dose of drug and achieves a better therapeutic effect. It overcomes the inconvenience of carrying an external electrical device for electrochemotherapy and the secondary damage to patients by inserting electrodes. Thus, electrochemotherapy (EchT) achieved by combining anti-cancer single drugs with piezoelectric materials and inherent electric field stimulation provides an excellent solution for precise low-dose and efficient anti-tumor therapy.

In addition to improving tissue penetration by the US remote activation of piezoelectric materials, identifying tumor cells based on membrane potential and increasing precise drug deposition, Mushtaq *et al.* developed intelligent nanorobotic systems, similar to natural sperm and electric eels, which were capable of propulsion based on chemical driving forces and transformational activation by electrical, magnetic, optical, or acoustic stimulation, prompting wave-like or spiral motion in biofluids navigation.[79] Essentially nanorobots mimic the flagellar or ciliary motions of prokaryotes and eukaryotes by building asymmetric chiral or helical structures and asymmetric driving through field manipulation. Mushtaq *et al.* developed nanorobots with coaxially aligned P(VDF-TrFE) tails and nickel (Ni) ring-polypyrrole (PPy) nanowires using coaxial lithography for the sustained release of adriamycin (DOX). The piezoelectrically responsive P(VDF-TrFE) flexible tail generated an induced spontaneous polarization–depolarization cycle as the strength and frequency of the magnetic field changed, forming a wave-like motion acting as a thruster, and the rotating magnetic field stimulated the translational motion of the entire nanorobot to achieve a swimming movement pattern. At the target site, the drug release mode was achieved by adjusting the magnetic parameters (10 mT and 7 Hz) to obtain pulsed drug release by electrostatic desorption. As shown in the figure, DOX delivery to cancer cells resulted in 35% cell death in the drug release mode, whereas only 10% cell death in the swimming mode. However, the large size and biodegradability of this smart nanorobot limit the space of its clinical application, and its size is expected to break through the limitation of 3D printing technology in the intelligent bionic sensing and drug delivery fields.

5.2 Dynamic therapy

Shi and colleagues at the Shanghai Institute of Ceramics, Chinese Academy of Sciences (CAS) first introduced the new concept of ''nanocatalytic medicine'' in the international authoritative review journal *Chem. Soc. Rev.* in 2018.[91] The application of this new approach for the efficient and safe treatment of tumors opens up a new research field for the development of nanomedicine and clinical medicine and provides a new and less toxic and effective solution for cancer treatment in personalized biomedicine. This will be an important guiding significance for the intersection of chemistry, materials, biology and medicine. This concept has led to an explosion of research in this direction, where nanoparticles with bioactive components and catalytic activities of different intensities are used as catalytic nano-agents or reactants in the tumor region to generate reactive oxygen species (ROS) for cancer therapy under exogenous stimuli (*e.g.*, laser, US, ionizing radiation and electric current) or endogenous tumor microenvironment (*e.g.*, mild acidity, H_2O_2 excess and hypoxia). Novel ROS-mediated therapeutic modalities include photodynamic therapy (PDT),[92,93] sonodynamic therapy (SDT),[94,95] chemodynamic therapy (CDT),[91,96,97] radiodynamic therapy (RDT),[98–100] and electrodynamic therapy (EDT).[101,102] Recently, the reported development of these therapeutic modalities in parallel to the above-mentioned piezoelectric dynamic therapy (PZDT) and pyroelectric dynamic therapy (PEDT) concepts, which first appeared in the review by Chen *et al.* on nanodynamic therapy, refer to therapeutic approaches with similar catalytic processes involving piezoelectric and pyroelectric effects as PZDT and PEDT.[103–107] Furthermore, when designing photosensitizers based on bioapplication theory, the selection of photosensitizers that can directly generate a piezoelectric potential should be considered as the best strategy. Piezoelectric photosensitizers can enhance the redox reaction processes in bodies and surfaces by polarizing charges, which promote the movement of different types of carriers to different locations in space. This controllable property allows the extension of piezoelectric photonics in the field of medical therapeutic research to complement traditional photodynamic therapy with new working principles (Table 3), which is an example of multidisciplinary cooperation in solving practical scientific problems.

5.2.1 Piezoelectric dynamic therapy (PZDT). Piezodynamic therapy is a process that directly converts mechanical energy into chemical energy. Shi's team described that ultrasound can generate microscopic voltage potentials by acting as a microscopic pressure source for piezoelectric tetragonal barium titanate. Additionally, the electrons and holes were continuously separated and accumulated through the built-in electric field created by the piezoelectric potential. It eventually bended the conduction band and valence band under piezoelectric catalysis to favor the generation of $^{\bullet}O_2^-$ and/or $^{\bullet}OH$ for tumor

Table 3 Application of piezoelectric materials in nanodynamic therapy

Materials	Size	Operating principle	Outcome	Ref.
PZDT				
$MnTiO_3$ nanodisks	The average diameter is about 170 nm and the thickness is about 19 nm	US irradiation (1 MHz, 1.75 W cm^{-2}, 40% duty cycle, 3 min)	Compared with traditional artificial enzymes, $MnTiO_3$ enzyme activity is only ultrasonically activated, and pH can control triple enzyme activity switching to achieve programmed tumor killing.	110
$Cu_{2-x}O$–$BaTiO_3$ nanocubes	The average diameter is 162.3 ± 3.5 nm	US irradiation (1.0 MHz, 1.0 W cm^{-2}, 50% duty cycle, 5 min)	A combination of CDT and SDT treatment with a further enhancement of carrier separation by heterogeneous junctions.	103
Bi doped oxygen-deficient $BaTiO_3$	The average diameter is about 100 nm	US irradiation (1.5 W cm^{-2}, 50% duty cycle, 1 MHZ, 3 min)	Oxygen defect engineering reduces the energy band gap, and the Bi nanoparticle-modified Schottky junction promotes carrier transfer and separation, which inhibits the compounding under ultrasonic irradiation. All properties are higher than $BaTiO_3$.	63
Tetragonal $BaTiO_3$	The average diameter is 106.91 ± 49.72 nm	US irradiation (1.0 MHz, 1.0 W cm^{-2}, 50% duty cycle, 3 min)	Compared with typical SDT, it is a more stable sensitizer and can dynamically control redox reactions. The built-in electric field can regulate the band bending, which is conducive to the generation of ROS from an energy perspective.	108
Ultrathin 2D Bi_2MoO_6–PEG nanoribbons	About 79.26 nm long, 19.95 nm wide, and 6.03 nm thick	US irradiation (40 kHz; 3 W cm^{-2}; 50% duty cycle; 5 min)	GSH-activated Bi_2MoO_6 NRs with oxygen-deficient sites and US-induced polarization inhibit the recombination of electron–hole pairs and significantly increase the efficiency of ROS production in SDT.	128
Polarized KNNSe	—	After sintering and gradient polishing, KNNSe is subsequently polarized with a high electric field polarization device.	Selenium-doping and poling processing enhance the built-in electric field strength of KNN for increased generation of intracellular ROS, which in turn triggers the caspase-3 apoptotic pathway. In addition, the built-in electric field also increases the permeability of the cell membrane,	58
Black phosphorus nanosheet	The average thickness and average lateral dimension of 5.3 ± 3.7 nm and 162.4 ± 99.4 nm	US irradiation with different output power density and time for animal and cells studies	Ultrasonic excitation does not cause off-target toxicity. US causes mechanical strain on BP nanosheets, which induces piezoelectric polarization and makes the BP conductive band more negative than $O_2/{}^{\bullet}O_2^-$, accelerating ROS production.	109
PEDT				
mPEG-Au@$BiTiO_3$	Hydrodynamic sizes of 112.7 ± 7.0 to 205.6 ± 9.0 (in water) and 158.7 ± 4.6 to 301.8 ± 12.5 nm (in cell culture medium)	Under 808 nm laser irradiation at different power densities (0.50.75 W cm^{-2}) for various durations (5–10 min)	Generates temperature-mediated non-O_2-dependent PDT for synergistic PTT and PDT treatment of hypoxic tumors.	111
Nb_2C MXene/CdS-HA	The average diameter is about 200 nm	1064 nm laser (1.0 W cm^{-2}, LSR-1064H-2W-19031303C, China) for 5–10 min	PTT and tumor interstitial fluid decomposition are achieved under NIR-II laser irradiation, which reduces intercellular pressure and enhances tumor penetration. Meanwhile, ROS generated during pyroelectric dynamic therapy can further damage the deep tumor stem cells.	112
SnSe-PVP	The average diameter of about 250 nm and an average length of about 100 nm	The laser condition *in vivo* is 1064 nm-wavelength laser (1.0 W cm^{-2}), the effect *in vitro* was compared with 808 nm laser and 1064 nm at different power intensities.	SnSe-PVP nanorods generate enough heat for thermal therapy and photoacoustic imaging under NIR-II light. In addition, the temperature difference between the	129

Table 3 (*continued*)

Materials	Size	Operating principle	Outcome	Ref.
			photothermal and cooling processes caused the surface potential difference of SnSe-PVP nanorods. This produces ROS to attack HSPs and cancer cells.	
MEDT				
$CoFe_2O_4$–$BiFeO_3$	The average diameter is about 45 nm	The magnetic field intensity is 1.6 mT	The magnetically driven and piezoelectric catalytic reactions within the tumor are initiated under an alternating magnetic field, generating ROS to effectively induce tumor cell death and local solid tumor ablation.	114
Thermal therapy				
Triglycine sulfate (TGS)	The preferred size of TGS is between 1 and 100 μm. The TGS@PLGA particle size is about 15 microns.	Electric field with applied power of 20 W and 30 W	Ferroelectric material TGS has better biocompatibility than ferromagnetic materials and degrades slowly in body fluids. Biocompatibility is further improved by biodegradable non-ferroelectric coatings such as PLGA, PGA and PLA. T_c in the range of 41.5 °C to 50 °C to prevent overheating.	116
$(La,Sr)MnO_3$ nanoparticles and films	Nanoparticles with the average size of 30–40 nm. Films with the thickness of 250–500 nm	Alternating magnetic field (300 kHz, 7.7 kA m^{-1})	The temperature increased up to 72–75 °C within the first 10 min of AMF action.	117
$BiFeO_3$	Micro-meter scale	Alternating current electric field of 5 kHz.	A rapid increase in temperature upon the application of an alternating electric field. The heating power efficiency of $BiFeO_3$ for electrothermal therapy materials was also characterized as 33.85 W g^{-1}.	119
$Bi_{0.95}Ba_{0.05}Fe_{0.95}Mn_{0.05}O_3$	The average diameter is approximately 44 nm for the pure BFO, 35 nm for 5% Mn-doped NPs, and 29 nm for Ba co-doping	Alternating magnetic field with unclear frequency	The appropriate concentration and element doping change the local magnetic structure. It retains ferroelectric properties and the magnetization increases by about an order of magnitude.	61
Nano-piezoelectric immunotherapy				
PVDF	β-PVDF and α-PVDF films exhibit a flat and smooth morphology	Ultrasound with a frequency of 80 kHz	Local electrical signals mediated by piezoelectric materials can non-invasively enhance the proinflammatory response of macrophages with the assistance of ultrasound. Activation of the immune system by electrical signal modulation *via* nano-piezoelectric materials	120
Mobile health (mhealth)				
$BiFeO_3$-modified with TAT peptide (TAT–BFO)	An average size of around 100 nm	The smartphone controls pulse temperature fluctuations for exogenous stimulation	Under the control of a wearable heating device, TAT–BFO can be enriched at the tumor site by magnetic targeting, and then triggered by temperature fluctuations to produce ROS, thereby effectively treating tumors and inhibiting their recurrence.	121
Tumor-treating fields (TTFields)				
$BaTiO_3$ (BTO)	Two different sizes of fetal bovine serum-coated BTO (100 nm and 200 nm).	2 V cm^{-1} at 150 kHz with a current of 150 mA generated by inovitro TTFields generators	BTO enables TTFields-resistant breast cancer cells to respond to TTFields. In addition, the combination of TTFields with BTO showed anti-tumor activity by regulating apoptotic pathways associated with the cell cycle. BTO enhanced the anti-tumor effect of TTFields through the cytosolic accumulation in response to an electric field.	122

Table 3 (*continued*)

Materials	Size	Operating principle	Outcome	Ref.
Biotherapeutic devices ts-PENG based on β-PVDF	The overall size of ts-PENG is 2 cm × 6 cm × 0.5 mm, and its weight is just about 1.68 g.	A periodic external mechanical force by a linear motor	ts-PENG is constructed based on β-PVDF, serving as a wearable and implantable power source by converting the biomechanical energy of body movement into electrical energy. ICLS can provide intermittent intense radiation, which is suitable for initial effective killing of tumor tissue, while PLS provides continuous low-dose radiation, which is suitable for clearing residual small tumors. Patients could manage both treatment modalities autonomously.	28
Ablation needle A mm-scale piezoelectric receiver element based on PZT-5A	The wireless electrolytic ablation microprobe consists of a millimeter-sized piezoelectric ultrasonic receiver, a rectifier circuit, and a pair of platinum electrodes (overall size is 9 × 3 × 2 mm^3).	Low-intensity ultrasound of approximately 200 mW cm^{-2}	It allows for wireless remote control of turning devices on and off and can provide flexibility in treatment options, making it easier to assign doses over longer periods.	126

therapy. This process resembles piezoelectric catalysis, and thus it is also called piezoelectric-catalyzed dynamic therapy (Fig. 12A–C).[108] Electron spin resonance (ESR) technology verified that the reactive oxygen species generated during piezoelectric catalysis are $^{\bullet}O_2^-$ and $^{\bullet}OH$ (Fig. 12A). According to the finite element modeling simulation, the piezoelectric potential of BTO increased with an increase in pressure (Fig. 12B). According to the band gap of about 2.56 eV and flat band potential of 0.16 V, T-BTO was theoretically disadvantageous for the formation of $^{\bullet}OH$ and $^{\bullet}O_2^-$ in terms of energy (Fig. 12C). However, the built-in electric field regulated the energy band tilt, which was more conducive to generating toxic reactive oxygen species. These results indicate that it is a promising way to exploit the piezoelectric effect of materials to develop new nanomedicine for dynamic therapy. Subsequently, Yang *et al.* similarly validated the possibility of black phosphorus as a piezodynamic therapy sensitizer under the action of US (Fig. 12D–F).[109] Ultrasonic waves introduce mechanical strain to the BP nanosheets, resulting in piezoelectric polarization (Fig. 12D). After ultrasound treatment, the intrinsic energy band of BP was tipped, and thus the negativity of the BP conduction band was greater than that of $O_2/^{\bullet}O_2^-$, accelerating ROS production (Fig. 12E). Moreover, the reactive oxygen species produced by BP under ultrasound were determined to be $^{\bullet}O_2^-$ and $^{\bullet}OH$ using specific fluorescent probes (Fig. 12F).

Some individual piezoelectric materials also have properties as nanoenzymes themselves, which were defined as piezoenzymes by Chen *et al.* Piezoelectric potentials were generated on $MnTiO_3$ nanosheets only when US stimulated the nanozymes to initiate the enzymatic reaction with the surrounding glutathione, avoiding drug side effects on normal tissues (Fig. 13).[110] In addition, the peroxidase (POD) mimetic activity and catalase (CAT) mimetic activity of $MnTiO_3$ nanosheets shifted with the environmental pH.

The acidic environment of tumors exhibited significant POD activity, catalyzing the accumulated H_2O_2 into oxidized $^{\bullet}OH$. In contrast, under neutral conditions in normal tissues, the CAT activity of $MnTiO_3$ nanosheets decomposed H_2O_2 into O_2, thus minimizing the toxicity of the accumulated H_2O_2 to normal cells. The authors proposed a novel idea of programmed tumor killing by exploiting the controllability of multi-mimetic enzyme activity, using US and the tumor microenvironment as input signals and calculated output cytotoxicity based on the Boolean logic algorithm. Therefore, the piezoelectric dynamic therapy paradigm combines piezoelectric catalysis, US and tumor therapy, providing a novel and promising strategy for noninvasive lateral abdominal tumor therapy using nanocatalytic drugs. Future work will focus on piezoelectric catalysis for the treatment of tumors *in situ* or patient-derived tumor xenografts, which has important implications for potential future clinical translation. Notably, the current PZDT paradigm is still in its preliminary stages, with only a few proven examples showing the feasibility of this therapeutic modality. However, the feasibility and efficacy of the developed PZDT are encouraging, facilitating further development and implementation of PZDT in a variety of biomedical applications.

5.2.2 Pyroelectric dynamic therapy (PEDT). Pyroelectric dynamic therapy is a method that uses pyroelectric materials to generate pyroelectric positive and negative charges located in the electronic surface state when the thermodynamic equilibrium is disturbed by temperature changes, which directly or indirectly induces ROS production for anti-tumor therapy. This approach was developed due to the increasing emphasis on pyroelectric catalysis. Pyroelectric materials can be activated by different degrees of temperature changes depending on the material properties, and pyroelectric catalysis can work in the dark using residual heat or natural heat to induce the production of reactive oxygen species for tumor therapy, which is

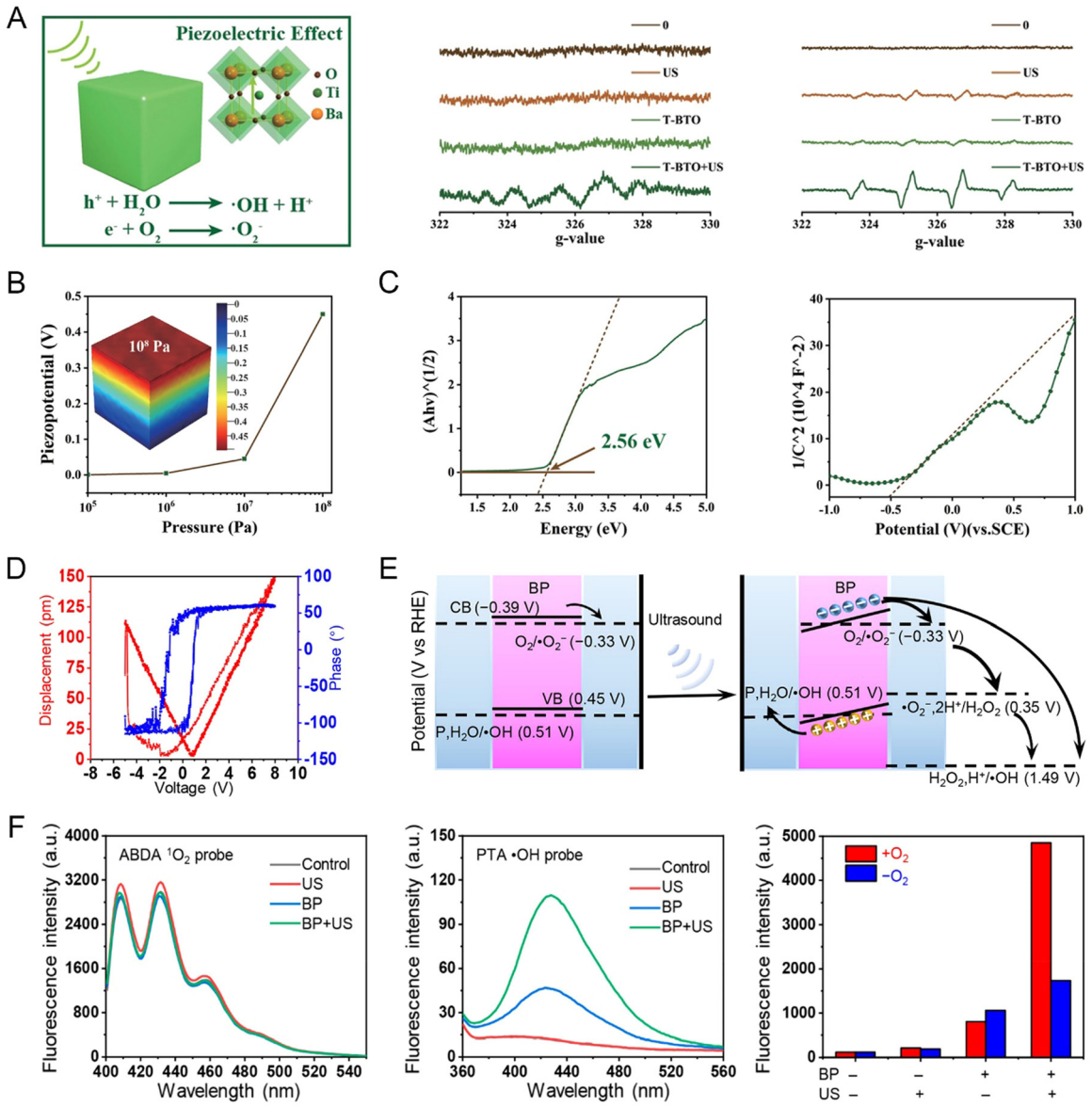

Fig. 12 (A) Schematic and ESR spectra of $^{\bullet}O_2^-$ and $^{\bullet}OH$ generation by tetragonal $BaTiO_3$ (T-BTO) nanoparticle-mediated piezoelectric effect. (B) Cavitation pressure-dependent piezo-potential of $BaTiO_3$ nanocrystals and COMSOL simulation for piezopotential distribution. (C) Bandgap and Mott Schottky spectra of T-BTO nanocrystals.[108] Copyright 2019, WILEY-VCH. (D) Height phase hysteresis loop and amplitude butterfly loop for BPs. (E) Changes in the inherent energy band of BP nanosheets after ultrasonic excitation. (F) Assessment of ROS production capacity.[109] Copyright 2020, the American Chemical Society.

more universal and portable than other dynamic sensitization therapies.

The majority of the dynamic therapy process still requires electron–hole or charge redox reactions with oxygen and water adsorbed on the material surface to generate ROS, but the hypoxic and necrotic zones in solid tumors can account for more than half of the tumor volume, which does not guarantee sufficient oxygen supply for the dynamic therapy process. Although there are studies on the development of devices that can deliver or generate oxygen at the tumor site, the slow O_2 diffusion rate usually cannot catch up with the rapid O_2 consumption rate during PDT, leading to unsatisfactory PDT efficiency. Zhang *et al.* synthesized plasma pyroelectric Au@BTO core–shell nanostructures for generating temperature-mediated O_2 non-dependent PDT to achieve tumor growth inhibition under low-oxygen conditions (Fig. 14A–D).[111] Under 808 nm laser conditions, the plasma of Au nuclei could achieve high temperature for the elimination of cancer cells for photothermal therapy (PTT), while a portion of heat is transferred to the pyroelectric BTO shell layer, and the temperature increase can reduce the spontaneous polarization of BTO. This results in the release of a large number of holes on the BTO surface in an O_2-independent manner to promote the formation of hydroxyl radicals. Under hypoxic conditions, O_2-dependent PDT and PTT cause damage to tumor cells and significantly inhibit tumor growth in mice. ESR spectra confirmed that polyethylene glycol (PEG)-modified

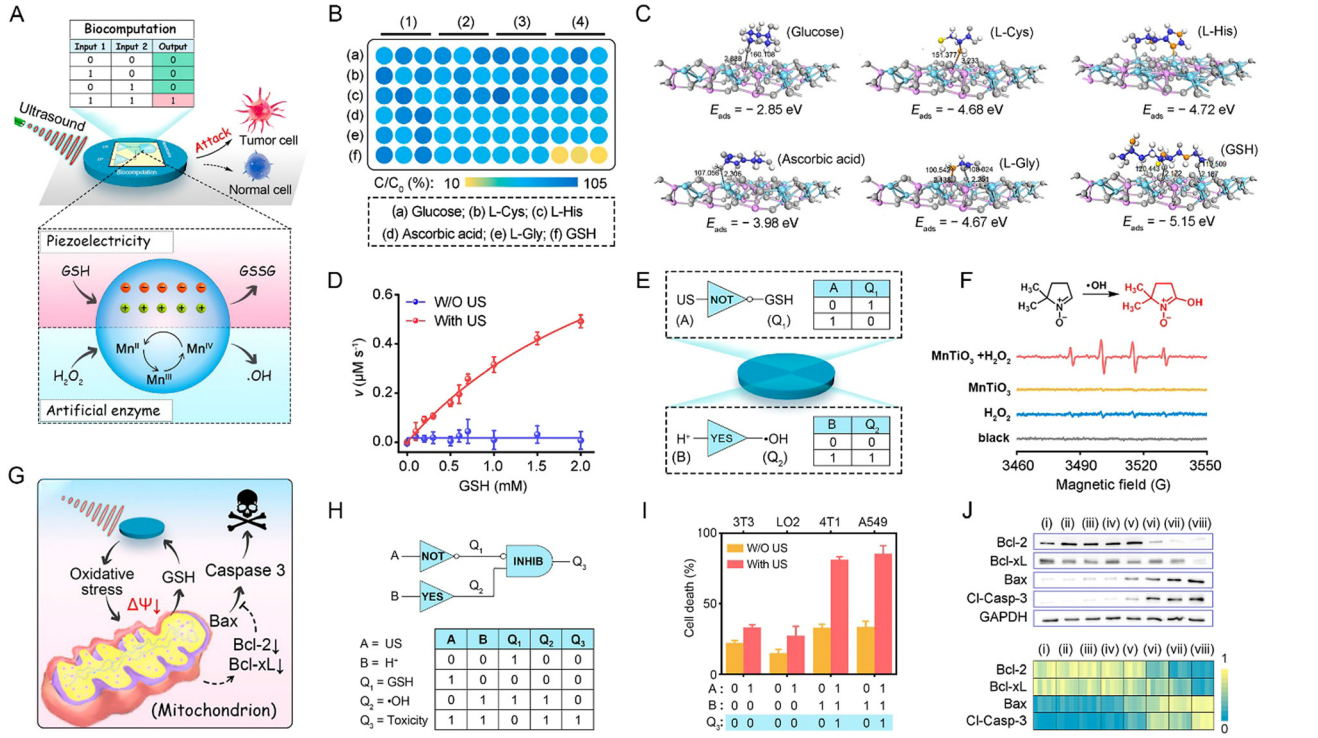

Fig. 13 (A) Schematic diagram of $MnTiO_3$ nanosheets for precise cell killing in biocomputing programs. (B) Selective oxidation of GSH by $MnTiO_3$ nanodisks under US. (C) Adsorption energy of $MnTiO_3$ nanodisks for reduced biomolecules was compared by thermodynamic calculation. (D) GSHOx-like enzyme kinetics of $MnTiO_3$ nanodisks with or without US. (E) Biocomputational programming for GSH consumption and •OH generation by $MnTiO_3$ nanodisks. (F) ESR spectra for •OH generation. (G) Schematic diagram of apoptosis mechanism induced by ultrasonic stimulation of $MnTiO_3$ nanodisks. (H) $MnTiO_3$ nanodisks for tumor killing by biocomputing programs. (I) Cytotoxicity of biocomputation programs to normal and tumor cells. (J) Expression of apoptosis-associated proteins was analyzed by western blot after different treatments: (i) blank control, (ii) pH 6.0, (iii) US, (iv) pH 6.0 + US, (v) $MnTiO_3$ nanodisks, (vi) $MnTiO_3$ nanodisks + pH 6.0, (vii) $MnTiO_3$ nanodisks + US, and (viii) $MnTiO_3$ nanodisks + pH 6.0 + US. With GSH as an output signal, the left GSH $>50\%$ and $\leq 50\%$ were defined as 1 and 0, respectively. With •OH as an output signal, the signal-to-noise ratios of •OH >5 and ≤ 5 were defined as 1 and 0, respectively. With cytotoxicity as the output signal, cell death rate $>50\%$ and $\leq 50\%$ were defined as 1 and 0, respectively.[110] Copyright 2022, the American Chemical Society.

Au@BTO (pAu@BTO) could produce reactive oxygen species under both hypoxic and normal oxygen conditions (Fig. 14B). The pAu@BTO water suspension demonstrated a substantial photothermal performance with a photothermal efficiency of 45.61% after being exposed to an 808 nm laser (0.75 W cm^{-2}) for 10 min (Fig. 14C). The increased intracellular ROS induced hierarchical oxidative stress responses, including the lower tier of NF-E2-related factor-2 (Nrf2)-mediated phase II enzyme overexpression, such as Nrf2 and HO-1. western blot showed that under hypoxia conditions and 808 nm laser irradiation, pAu@BTO could induce the enhanced abundance of Nrf2 and HO-1 (Fig. 14D). Meanwhile, cell hyperthermia also enhanced the expression of heat shock proteins (HSP), a potential biomarker that triggers high-temperature stress. This indicates that pAu@BTO has the ability to generate ROS and photothermal in cells.

Also, the pyroelectric effect enhances the tumor tissue penetration of drugs, as described in Section 5.1. Gao *et al.* enhanced the drug tissue penetration by reducing the tumor interstitial pressure through the pyroelectric material CdS-assisted nano-Nb_2C MXene. Photothermal therapy and tumor interstitial fluid decomposition were achieved under NIR-II laser irradiation (Fig. 14E).[112] This process relieved 52% of the tumor interstitial pressure (TIP), resulting in enhanced tumor penetration and effective inhibition of tumor proliferation (93.75%) and recurrence. The decomposition of the tumor interstitial fluid was evaluated by detecting the water content of the tumor. The tumor interstitial fluid could only be dissociated by the laser-irradiated M/CdS-HA, which also had a pyroelectric catalysis and photothermal effect (Fig. 14F). This demonstrates the feasibility of the strategy of reducing TIP by splitting water in the tumor. The decrease in TIP improved the blood perfusion. In addition to increasing the oxygen content in the tumor, it also caused the nanomedicine to accumulate there. The depletion of lactate in tumors implies that lactate reacts with the positive charge generated by pyroelectric catalysis, facilitating the reduction of the negative charge, and thus enhancing the generation of ROS. M/CdS-HA could damage the deep tumor stem cells under light irradiation, and thus the possibility of tumor recurrence after drug withdrawal was minimal.

5.2.3 Magnetoelectrodynamic therapy (MEDT). A magnetic field, as an external stimulus, is not limited by penetration depth, mechanical damage, thermal damage, or surgical

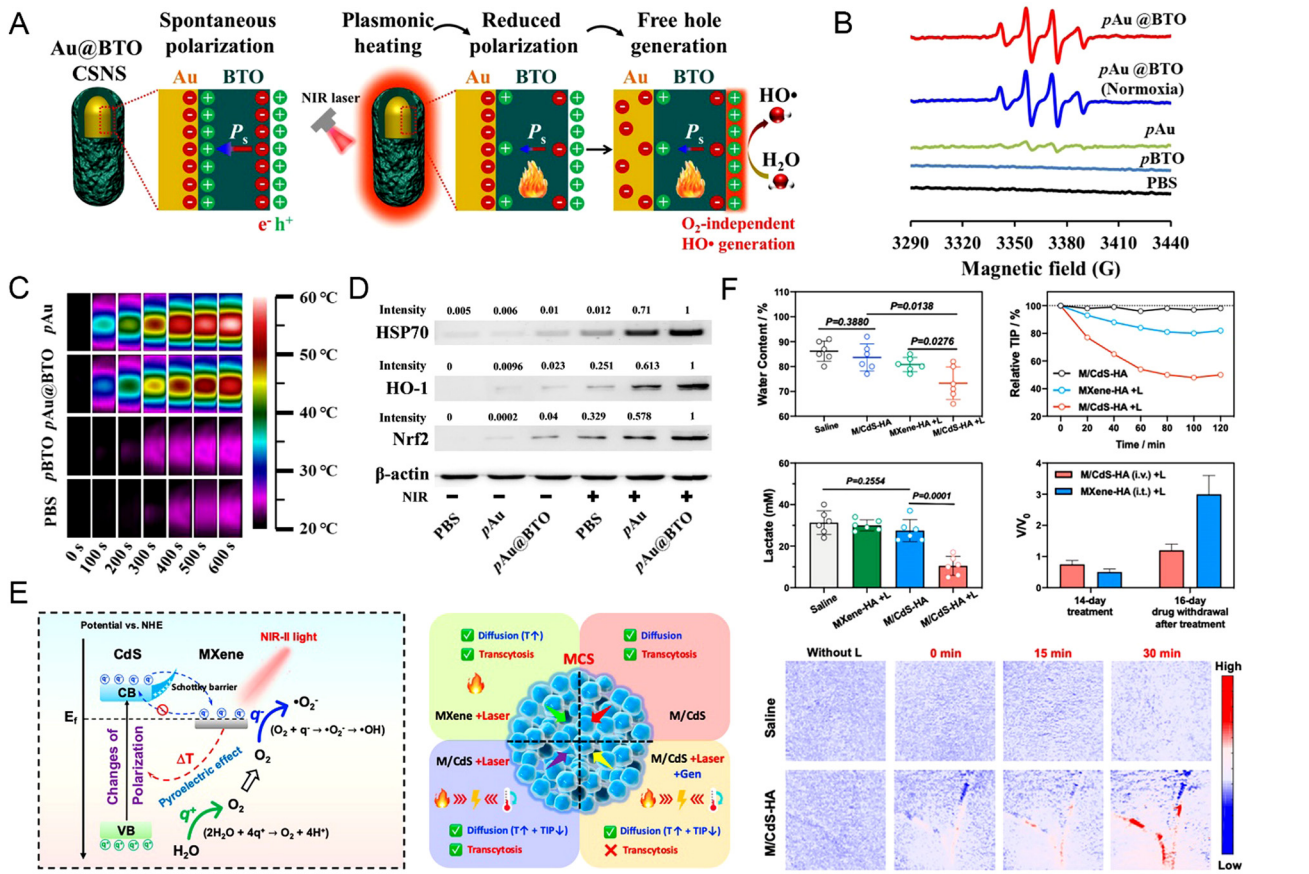

Fig. 14 (A) Mechanism of pyroelectric dependent synergistic light therapy in Au@BTO. Au@BTO-related (B) ESR spectra, (C) infrared thermal images, and (D) western blot analysis.[111] Copyright 2021, Elsevier. (E) Pyroelectric catalysis of M/CdS for ROS generation and penetration mechanism. (F) Water content, relative TIP, and lactate content in the tumor. Tumor recurrence after drug discontinuation. Oxygen content in blood vessels at different times after treatment.[112] Copyright 2020, the American Chemical Society.

intervention, and has characteristics such as noninvasiveness, depth of tissue penetration, and ease of remote control. Benefiting from magnetically correlated hysteresis energy loss and Neal or Brownian relaxation, studies have focused on magnetothermal therapy, magnetron drug delivery, and in-depth exploration of magnetic resonance imaging (MRI).[86,113] Shi *et al.* combined magnetic physics and nanocatalytic chemistry to investigate magnetoelectrocatalytic chemical reactions of core–shell-structured $CoFe_2O_4$–$BiFeO_3$ magnetoelectric nanoparticles (CFO–BFO NPs) triggered by exogenous alternating magnetic fields (Fig. 15A).[114] A magnetic field, as a non-invasive, highly controllable and penetrating external stimulus, is used to generate ROS for the exploration of nanocatalytic tumor therapy. Magnetostrictive CFO cores and multiferroic piezoelectric BFO shells integrated with core–shell-structured $CoFe_2O_4$–$BiFeO_3$ magnetoelectric nanoparticles form a magnetoelectric engine that generates positive and negative polarization charges on the material surface by triggering an electrical process through magnetic commitment. The magnetic field-induced polarization process on the surface of CFO–BFO NPs was verified by theoretical modeling. The simulation results showed that the CFO nuclei undergo magnetostriction and generate significant microscopic stresses due to the magnetic confinement effect in the presence of a magnetic field. Consequently, this triggers the polarization of the multiferroic BFO and the formation of an electric potential on the surface (Fig. 15A–D). It catalyzed the oxidation of water and the reduction of oxygen molecules *in vitro* and *in vivo*, generating two types of ROS, *i.e.*, hydroxyl radical ($^{\bullet}OH$) and superoxide radical ($^{\bullet}O_2^-$), to induce cell death and local solid tumor ablation in tumor models, respectively. In addition, Shi *et al.* proposed a new concept of cancer therapy in this work, named magnetostrictive piezoelectric nanocatalytic medicine (MPE-NCM) or magnetoelectrodynamic therapy (MEDT), further extending the concept of nanocatalytic drugs.

The novel therapeutic modalities developed based on piezoelectric and pyroelectric materials are mostly the synergistic effect of multiple therapeutic modalities, such as piezodynamic + US dynamic therapy, piezodynamic + ultra-sonic + photodynamic therapy, piezodynamic + chemodynamic therapy, pyroelectric dynamic + photothermal therapy, and piezo/pyrodynamic + chemotherapy. These therapeutic modalities are complementary and mutually reinforcing, aiming to achieve a more efficient anti-tumor effect. However, there are no reports about the dynamic therapeutic modalities of ferroelectric materials.

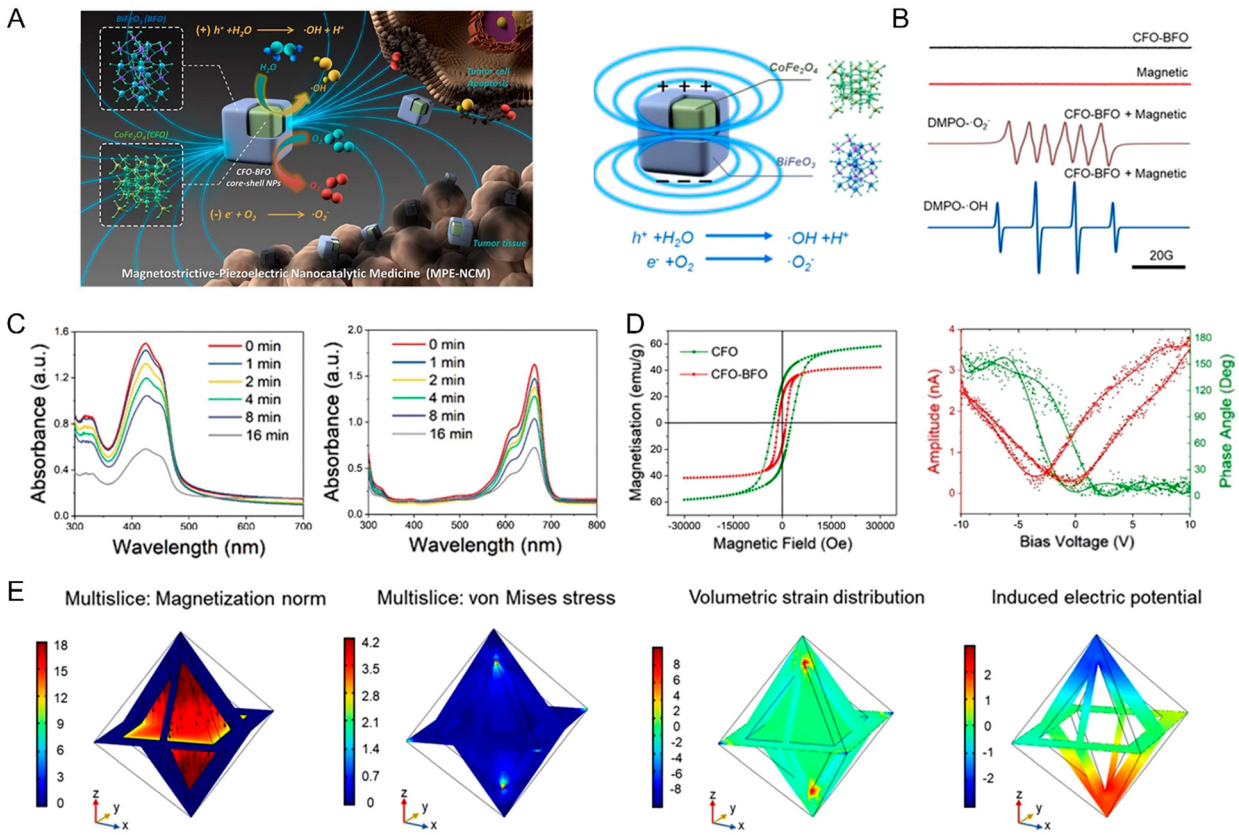

Fig. 15 (A) Schematic diagram of the antitumor cellular process of CFO–BFO NPs mediated by the magnetostrictive-piezoelectric effect. (B) ESR spectra. (C) DPBF and MB degradation efficiency. (D) Magnetic and piezoelectric properties. (E) Piezo-potential distribution simulated by COMSOL at 1.6 mT magnetic field.[114] Copyright 2021, the American Chemical Society.

5.3 Thermal therapy

Tumor thermotherapy is an age-old treatment method applied by local or systemic heating of tumor tissues for therapeutic purposes. Compared with normal cells, cancer cells are more sensitive to temperature fluctuations, and thus the core of thermotherapy is to deliver heat selectively to deep tumors, which can reduce side effects. However, despite its long history, its application is still in its infancy. Also, magnetic and ferroelectric particles should be present in the developed nanotherapeutic drugs. Both ferromagnetic particles and superparamagnetic particles generate heat after the application of an alternating magnetic field, where the former is due to hysteresis loss, while the latter is due to magnetic moment relaxation. A magnetic field can penetrate deep in tissues without being absorbed by the living tissue and with few side effects.[115] The best candidates for use in thermal therapy are magnetic materials with Curie temperatures in the range of 42–60 °C. The Curie temperature enables wireless switching control of the therapeutic device to avoid overheating. In 2006, Flores *et al.* invented a method for the non-toxic interstitial thermotherapy of local tumor cells using ferroelectric particles by introducing them in the target area of a patient and applying a time-varying electric field in the target area.[116] Ferroelectric materials have better biocompatibility compared to ferromagnetic materials and can be degraded slowly in body fluids. These particles have a preferred size of between 1 and 100 μm and a Curie temperature of between 41.5 °C and 50 °C. Three years later, they further improved this approach by using non-ferroelectric coatings such as PLGA (poly(lactic-*co*-glycolic acid)), PGA (polyglycolic acid) and PLA (Poly lactic acid) on the ferroelectric core. The coatings further improved the biocompatibility and were biodegradable, and thus at least one drug-active agent was contained under the coating layer with a particle size of about 15 μm, an approach that reduced the minimum concentration for ferromagnetic material efficacy.

The same results were obtained by Sergej Osinsky *et al.* after verifying the effect of nanotherapeutic chemical modifications on cisplatin. The results demonstrated that the combination of nano-hyperthermia and cisplatin chemotherapy achieved the best tumor inhibition *in vitro* and *in vivo*. It was also found that the particle size, coating and organic matrix all have an effect on the therapeutic properties.[117] According to the work by Professor Wang Xun in 2007, if a material reaches the sub-nanometer level in a certain dimension, the proportion of atoms on its surface is close to 100%. Thus, its interaction with the external field will be greatly enhanced, which will greatly enhance its photothermal effect. Also, the cytotoxicity, genotoxicity, antioxidant activity and antiviral activity tests

using (La, Sr)MnO_3 ferromagnetic nanoparticles (30–40 nm) with a calcium titanite structure were performed at the cellular and mouse level. This study showed that (La, Sr)MnO_3 nanoparticles at concentrations of 0.1–1 mg mL^{-1} do not exhibit any genotoxic activity. (La, Sr)MnO_3 sols at concentrations ranging from 0.65 to 5.0 mg mL^{-1} showed antioxidant activity with a percentage of live cells of 109%. Injection of magnetic fluid and subsequent application of an alternating field (at frequencies of 100–400 kHz) in the mouse model resulted in tumor arrest. These results suggest that thermal therapy with (La, Sr)MnO_3 nanoparticles as thermal media has some anti-tumor capacity.[118] Bismuth ferrate is equivalent to *Drosophila* in the study of multiferroic materials, which is one of the few multiferroic materials that is both magnetic and ferroelectrically ordered at room temperature. It can exhibit magnetoelectric coupling, which allows a magnetic field to modulate its magnetic properties, or conversely an electric field to modify its electrical properties.

Although $BiFeO_3$ has been intensively studied in the form of ceramics, single crystals and thin films, little is known about its powder properties.[119] Dai *et al.* prepared $BiFeO_3$ crystals *via* the solid-phase method and selected aqueous suspensions of $BiFeO_3$ particles with stable dielectric constants (at frequencies of 10–1000 kHz) for heating experiments, which showed a rapid increase in temperature upon the application of an alternating electric field, suggesting the possibility of using $BiFeO_3$ crystals for tumor electrothermal therapy. The heating power efficiency of $BiFeO_3$ for electrothermal therapy materials was also characterized to be 33.85 W g^{-1}. The main influencing factor of the thermal effect of $BiFeO_3$ suspensions is the dielectric properties of the suspension. This approach overcomes the tissue penetration limitations of *in vitro* heating methods including the use of hot water, light and microwaves. However, it cannot be ignored that $BiFeO_3$ crystals are simultaneously antiferromagnetically ordered at room temperature, which practically counteracts the magnetization and magnetoelectric coupling of the crystals. Doru C. Lupascu *et al.* introduced suitable concentrations of dopants in bismuth ferrate to induce limited coupling, which successfully disrupted part of the spin pendulum and increased the spin tilt.[60] The particle size could be reduced by the appropriate concentration and combination of doped nanoparticles. The temperature of the magnetic phase transition was also controlled at a lower temperature. While maintaining ferroelectric properties, the residual magnetization increased by an order of magnitude, making its application for cancer hyperthermia possible.

5.4 Nano-piezoelectric immunotherapy

Nano-piezoelectric immunotherapy is another extension of nanotechnology and immunotherapy. It is a therapeutic approach involving the activation of the immune system through the modulation of electrical signals from nano-piezoelectric materials. Electrical signals can directly edit the behavior of immune cells in an electrically mediated way, which are an important physical stimulus, and thus they have great potential in the biomedical field. For example, as one of the most important innate immune cells, macrophages play an important role in the treatment of many diseases and biological processes. Finding rapid and efficient methods to regulate the phenotypic polarization of proinflammatory macrophages M1 can help kill cancer cells or inhibit tumor growth. Liu *et al.* non-invasively enhanced the pro-inflammatory responses of macrophages with US assistance through local electrical signals mediated by piezoelectric materials (Fig. 16).[120] This strategy relies on the microvibrational deformation of piezoelectric β-phase polyvinylidene fluoride (β-PVDF) films driven by US irradiation, which induced the release of local charges after spontaneous polarization of the crystal phase. Voltage-sensitive receptors on macrophages could detect these local electrical signals (Fig. 16A), consequently causing the selective production and secretion of pro-inflammatory chemoattractant molecules TNF-α and IL-1β. Thus, the polarization of macrophage M1 was significantly enhanced or regulated. During wireless ultrasound treatment, ultrasonic stress induced a voltage potential to cause Ca^{2+} influx through voltage-gated channels and the establishment of the Ca^{2+}-CAMK2A-NF-κB axis to promote a proinflammatory macrophage response (Fig. 16B). This conclusion was validated by a multi-omics approach. Differential gene screening, a heat map of differential clustering of voltage-sensitive channel-related genes, Kyoto Encyclopedia of Genes and Genomes (KEGG) analysis, and gene ontology (GO) functional enrichment analysis were performed to determine the details of the signaling pathways significantly enriched in the differentially expressed genes between the TCP group and the betas + US group (Fig. 16C). Omics studies confirmed that the active component of this process is the electric potential rather than ROS. This conclusion was further verified by a calcium influx experiment and analysis of calcium/calmodulin kinase family expression. western blot analysis and immunofluorescence staining showed that the piezoelectric material mediated the electrical signal-induced macrophage inflammatory response depending on the ability of the potential-Ca^{2+}-CAMK2A-NF-κB signaling pathway. It showed that electrical impulses mediated by piezoelectric materials can controllably trigger inflammatory reactions with the help of noninvasive ultrasonography. Additionally, an electrogenic strategy to control immune cell destiny and achieve tumor immunotherapy was presented. The colony formation experiment intuitively showed that the macrophages in the +US group had the best inhibitory effect on the proliferation of HepG2 cells (Fig. 16D). It is also worth noting that the authors suggested three areas that can be further explored in the future based on their results including pericyte therapy, postoperative therapy, and nanovaccines.

5.5 Mobile health (mhealth)

As smartphones, the Internet, and EPC network become increasingly relevant in daily life, it has become an inevitable trend to integrate advanced medical technologies and mobile health to manage disease. mHealth is the practice of medicine and public health supported by the use of mobile Internet communication technologies and portable mobile devices. Today, mHealth is used in many areas of healthcare, including disease surveillance, health assessment management, and health

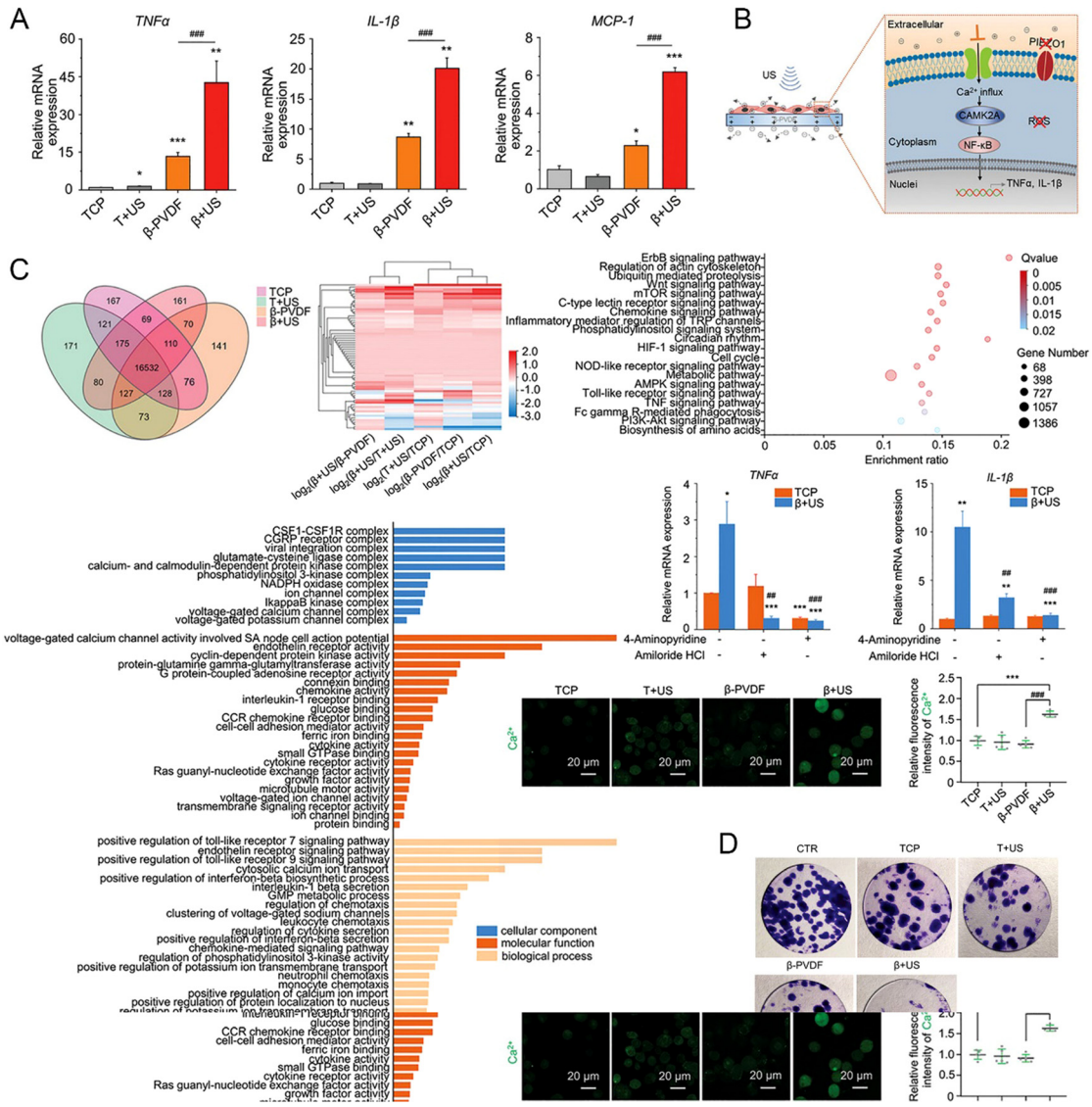

Fig. 16 (A) Relative mRNA in typical markers of M1 macrophages TNF-, IL-1 and MCP-1 expression after treatment with different materials and stimulation conditions. (B) Schematic diagram of the inflammatory reaction driven by electrical signals mediated by piezoelectric materials with the assistance of non-invasive ultrasound. (C) Multi-group approach to explore the molecular mechanism of piezoelectric effect. (D) Coculture of macrophages and tumor cells.[120] Copyright 2021, Wiley-VCH.

education. Mhealth technology developments inspire innovation in oncology treatment by simplifying the treatment process and will also provide the basis for changes in traditional oncology treatments in the clinical setting, thereby improving the comfort and convenience of oncology treatment, and also reducing barriers to patient and family participation in treatment. In this case, Zhang *et al.* integrated a TAT peptide-modified ferroelectric $BiFeO_3$ nanogenerator (TAT–BFO) and a wearable device to develop a smartphone-controlled healthcare platform.[121] TAT–BFO could be enriched at deep tumor sites by magnetic targeting after mobile phone-controlled wearable device administration (Fig. 17A). Perovskite-type bismuth ferric acid is a typical ferroelectric and pyroelectric material. Smartphone-controlled pulsed temperature fluctuations resulted in exogenous stimulation. The conversion of temperature fluctuations into electrical energy through the pyroelectric effect could trigger the generation of reactive oxygen species for effective tumor treatment through temperature fluctuations. As shown in Fig. 17B, BFO could output current under thermal cycling changes (dT/dt), which proved the pyroelectric effect of BFO. This system strived to achieve charge balance, followed by an increase and decrease in temperature. It leads to a change in the direction of the dipole, forming a current in the opposite direction. Similarly, the COMSOL simulations visually reflected the relationship between temperature fluctuations and potential distribution (Fig. 17C). A thermal imager monitored the time curve of the temperature of the opisthenar on the heating device to assess the good penetration depth of heat (Fig. 17D). The results showed that the temperature of the opisthenar increased by nearly 8 °C in the 10.24 mm posterior degree region after 8 min, proving that heat had a good

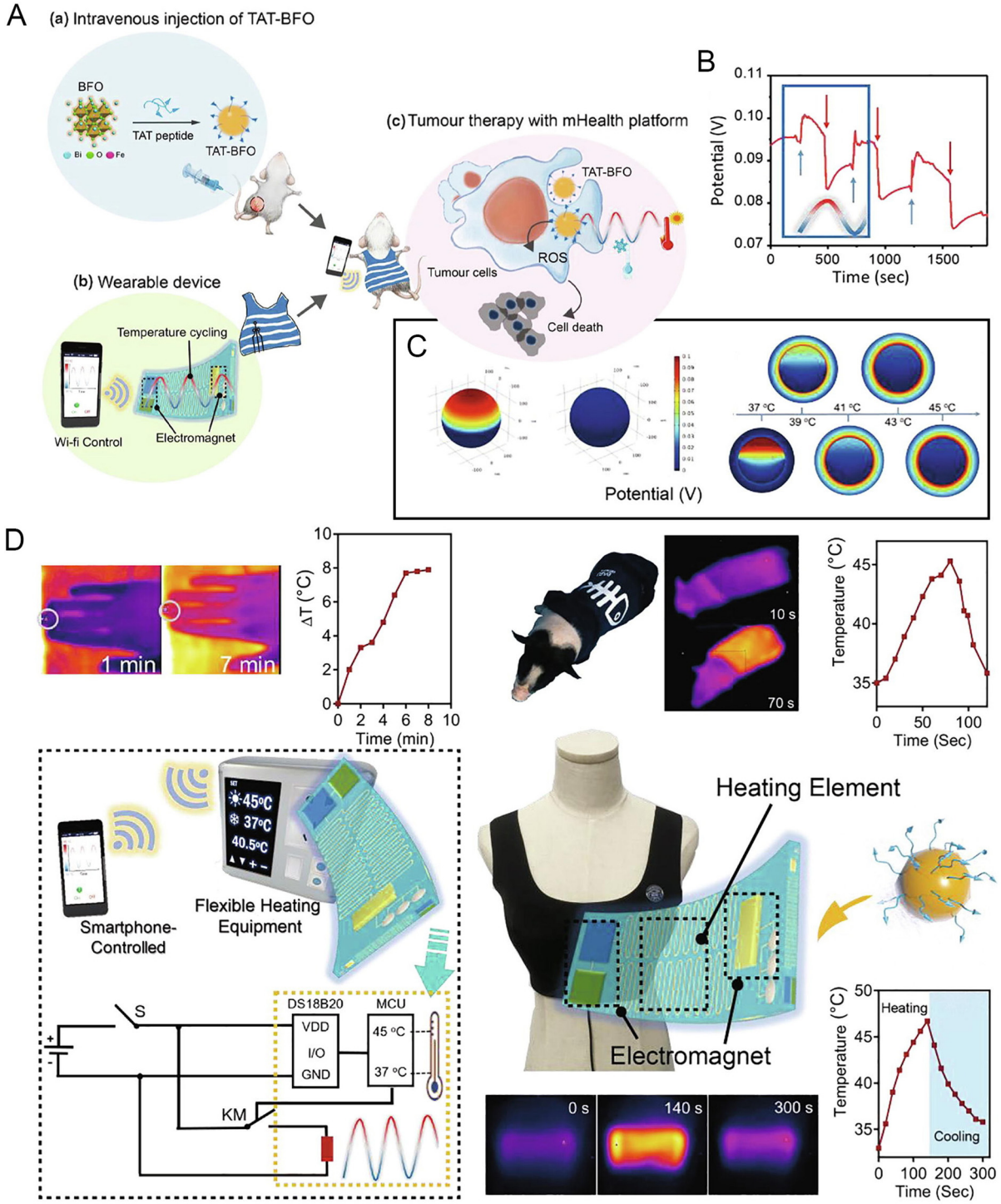

Fig. 17 (A) Schematic diagram of the nano-effector, controller and treatment design plan based on TAT–BFO mobile health platform. (B) Temperature-dependent output voltage conditions of BFO. (C) Temperature-dependent BFO electric field distribution simulated by COMSOL. (D) Thermal images and temperature cycle curves of the mobile health platform under different placement conditions as a function of heating time: opisthenar, piglets and people with heating by the temperature control program in a smartphone.[121] Copyright 2020, Elsevier.

penetration depth. Besides, this platform was shown to significantly inhibit tumor growth at a depth of centimeters from the skin and prevent tumor recurrence in unresectable mice with *in situ* mammary tumors and resectable breast tumor models. The healthcare platform was controlled by wearable devices developed in that study. The number of temperature cycles (37 °C and 45 °C) and switches of the heating device could be controlled *via* the smartphone wireless Wi-Fi. The feasibility of this model was verified in pig and human breast cancer models. This work integrated exogenous stimulation and magnetically targeted

nanomedicine in mobile health. It was safe, non-invasive, easy to use, and controllable, providing new ideas for novel treatment modalities. There are many reports on mhealth detection devices, but the mhealth-based experience is not mature and mhealth oncology treatment devices are still scarce.

5.6 Tumor-treating fields (TTFields)

Tumor-treatment fields (TTFields) is a new minimally invasive physical therapy method that works by creating an alternating electric field in the area of a lesion, which is capable of outputting low intensity (1–3 V cm^{-1}) and medium frequency (100–300 kHz), affecting the mitotic process of cancer cells and resulting in their in their death during their proliferation. This process causes the spindle filaments with electrode properties to rotate with the electric field, disrupting the dipole arrangement during cytoplasmic division, and the spindle filaments cannot reach the correct environment to meet the requirements of the division stage to maintain a normal structure, eventually collapsing for anti-cancer purposes. In 2019, the U.S. Food and Drug Administration (FDA) approved the combination of TTFields and chemotherapy for the treatment of locally advanced or metastatic malignant pleural mesothelioma (MPM), which has been proven to be effective in primary and recurrent tumors that are resistant to physical therapies. Because TTFields target ''dividing and proliferating'' cancer cells, they have little effect on the body's normal, terminally differentiated, and therefore no longer dividing and differentiating healthy cells. Therefore, they do not need to be based on specific targets like targeted therapy or immunotherapy and do not tend to accumulate doses in the patient's body like radiotherapy. Although TTFields are a promising non-invasive physical therapy modality, little is known about the sensitizers that respond to TTFields. As described in Sections 5.1 and 5.2, in the field of nano-oncology, ferroelectric nanomaterials can improve the cell and tissue penetration through remote electrical stimulation, and also mediate photodynamic and magnetothermal conversion. Barium titanate nanoparticles are representative ferroelectric materials with a high dielectric constant and suitable piezoelectric properties. Kim *et al.* verified that barium titanate nanoparticles (BTO) can be used as a novel TTFields responsive sensitizer (Fig. 18).[122] BTO showed excellent cytocompatibility in two breast cancer cell lines, *i.e.*, MCF-7 and BT-549, according to the cytocompatibility and clonogenic assay, and they found that BTO alone had no cytotoxic effect on breast cancer cells. However, in the presence of TTFields, it could sensitize TTFields-resistant MCF-7 breast cancer cells to realize the antitumor effect of TTFields, and the effect of 200 nm was superior to that of 100 nm. In addition, it was demonstrated by fluorescence-activated cell sorting (FACS), transmission electron microscopy analysis (TEM), and bright field images of cells stained with methylene blue that the combination of BTO and TTFields contributed to the accumulation of BTO in the cytoplasm of cancer cells. Nano String nCounter TM Pan-Cancer pathway

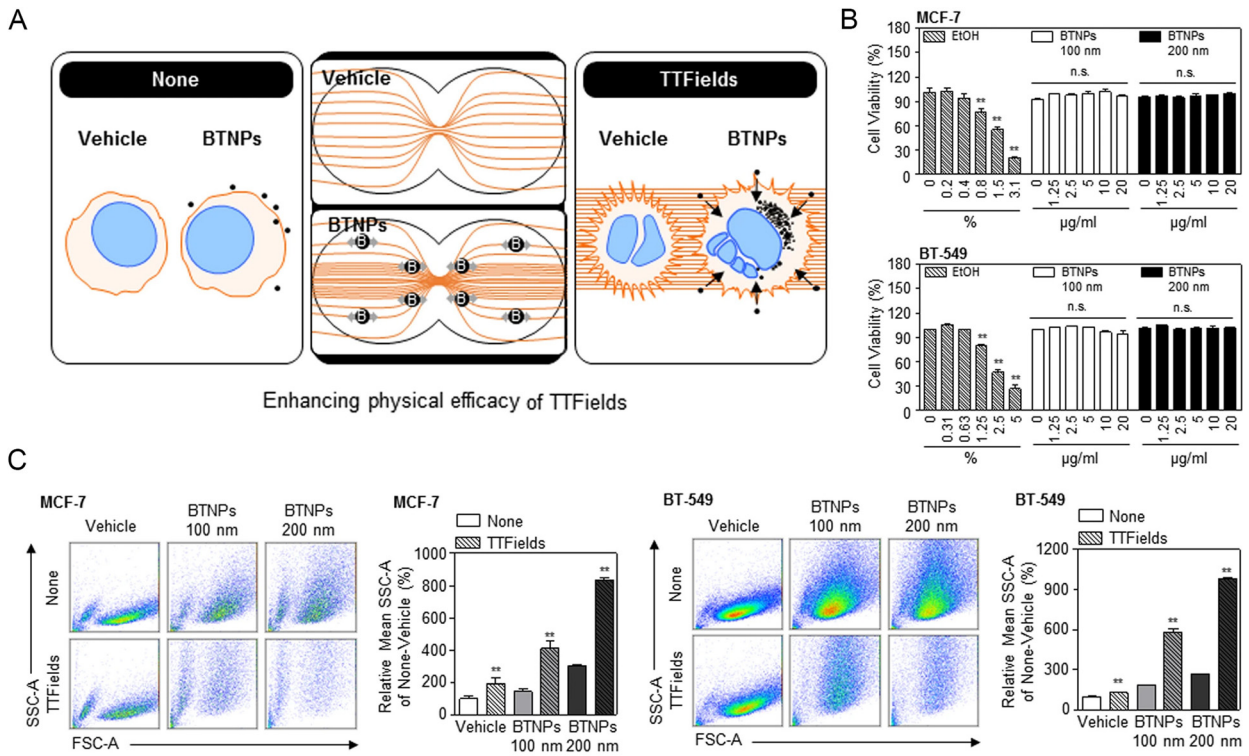

Fig. 18 (A) Schematic representation of BTNPs (they are equivalent to $BaTiO_3$ nanoparticles, BTO) enhancing the sensitization of cancer cells to TTFields. (B) Biocompatibility evaluation of BTNPs on MCF-7 and BT-549 cells. (C) Cytoplasmic accumulation of BTNPs before and after TTFields treatment.[122] Copyright 2020, Nature.

analysis containing probes targeting 700 transcripts related to 13 types of cancer pathways and FACS analysis for cell cycle demonstrated that TTFields, when bound to BTO, can exhibit antitumor activity by regulating cell cycle-related apoptotic pathways. Therefore, BTO enhanced the antitumor effect of tumor therapeutic fields through cytoplasmic accumulation of electric field response, thus establishing BTO as a tumor therapeutic field response sensitizer.

5.7 Biotherapeutic devices

The photodynamic therapy procedure directly determines the effectiveness of the treatment due to the physical nature of light. For most tissues, the effective depth of PDT varies from a few millimeters to 1 centimeter. Therefore, in the actual clinical photodynamic therapy procedure, the light source is usually delivered to the deep lesion location with the help of optical fibers and endoscopes to provide efficient short-term treatment. However, a downside is that the high light intensity during photodynamic therapy may cause thermal damage to the surrounding normal tissues, especially nerves and blood vessels, leading to undesirable organ dysfunction.[28] Nevertheless, the tumor suppression efficiency is insufficient if the light radiation intensity is reduced. Therefore, reducing the damage caused by the radiation dose and improving the removal efficiency of tumor cells are the key problems to be solved in photodynamic therapy. A research group utilized batteries and driving light-emitting diodes as wireless charging power sources for electroluminescent systems to continuously supply energy for long-term low-dose photodynamic therapy.[123,124] However, power components may cause inconvenience and additional potential risks during treatment. Furthermore, the rapid development of telemedicine and mobile health has put forward higher requirements for existing treatment methods, such as better patient compliance and autonomous management. Li *et al.* developed a self-powered photodynamic therapy (s-PDT) system with two different irradiation modes, pulsed light stimulation (PLS) and intermittent continuous light stimulation (ICLS), for antitumor therapy. As shown in the Fig. 19, the s-PDT system is formed based on the energy-harvesting unit of ts-PENG, photosensitizer, mLED and PMU. Considering its advantages simple structure, portability and flexibility, it meets the requirements of wearable medical devices. This system is driven by the conversion of biomechanical energy obtained from the motion of human joints into electrical energy. The long-term stability and longevity of the system were guaranteed compared to other power supply units such as microbatteries and wireless charging. In addition, the combination of two irradiation modes (PLS and ICLS) has good compliance for the

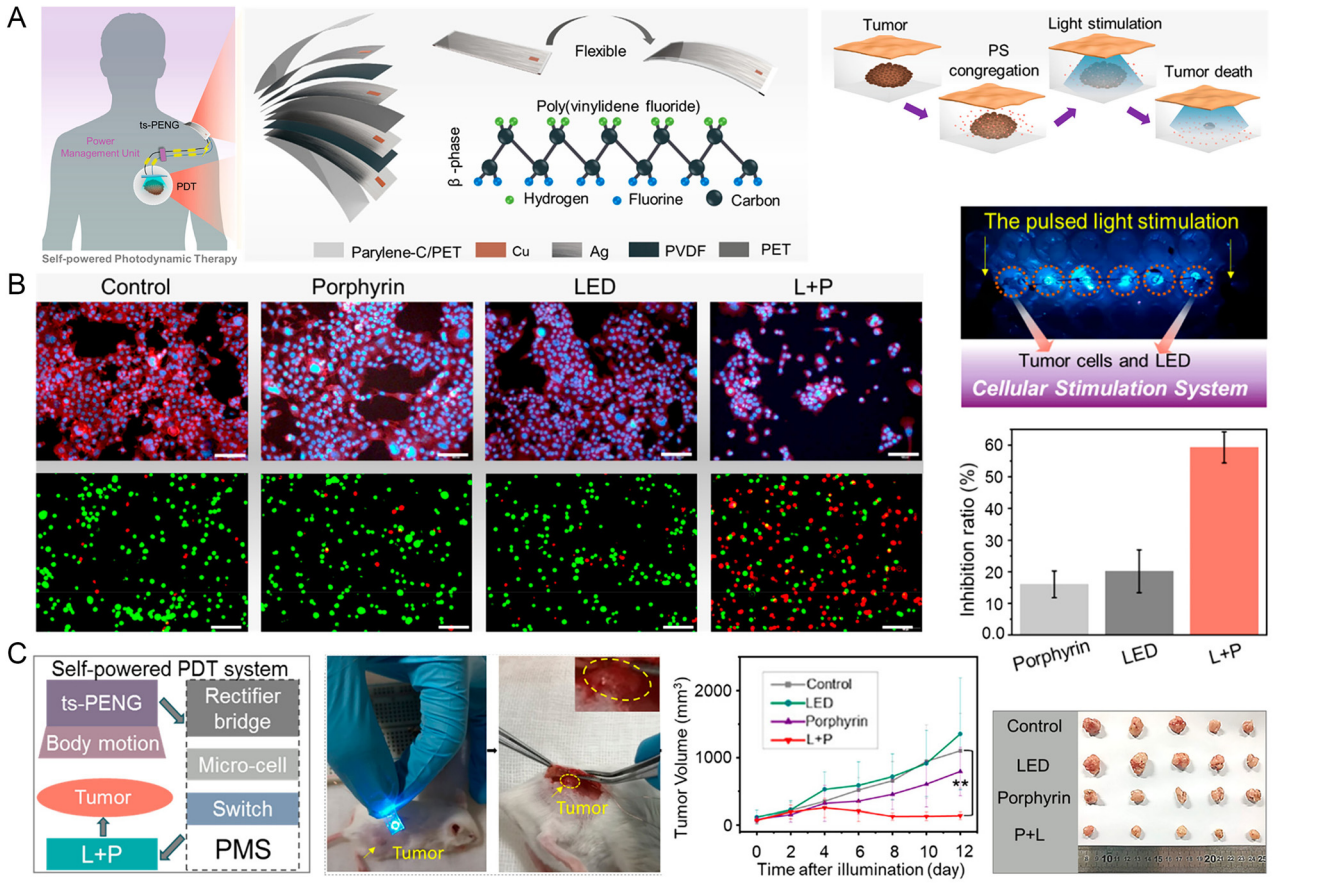

Fig. 19 (A) Composition and 3D structure of S-PDT system. Apoptotic process of subcutaneous tumor tissue. Anti-tumor efficiency *in vitro* (B) and *in vivo* (C).[28] Copyright 2020, the American Chemical Society.

treatment of tumors with different developmental levels through a well-designed power management unit. This gives the s-PDT system the advantage of good compliance, allowing patient autonomy in managing both treatment modes. ICLS can deliver intermittent intense radiation and is suitable for the initial stage of tumor treatment or effective killing of extensive tumor tissue, while PLS provides continuous low-dose irradiation and is suitable for removing residual microscopic tumors. The experimental results at the cellular level preliminarily verified that the s-PDT system had a significant inhibitory effect on tumor cell growth under pulsed light stimulation mode. The s-PDT system also produced significant anti-tumor effects with 87.46% tumor inhibition when micro light-emitting diodes were implanted subcutaneously in transplanted tumor-bearing mice and irradiated by intermittent continuous light stimulation mode for 12 days. This system has great potential for clinical application in various diseases requiring long-term treatment, such as diabetes, Parkinson's disease and cardiovascular disease. It also provides inspiration for the development of wearable/implantable and self-contained devices for long-term photodynamic therapy.

5.8 Ablation needle

Ablation is a minimally invasive procedure, which includes microwave ablation and radiofrequency ablation. The principle is the same for both, which is the insertion of a radiofrequency or microwave probe in a benign or malignant tumor. Generally, the temperature of tumor cells increases to about 80 °C, while sometimes reaching more than 100 °C. This causes the degeneration and coagulative necrosis of tumor cells, achieving the purpose of killing tumor cells. At present, the development and clinical trials of ablation needles are in different stages, with piezoelectric materials playing the role of transducers in most methods. For example, Gregory Scott Fischer *et al.* developed an ACOUSTx NBTU ablator based on interstitial high-intensity therapeutic ultrasound, using materials with nuclear magnetic properties as a variant of an ablation instrument to achieve real-time and nuclear magnetic image monitoring of the ablator.[125] The ACOUSTx ablator contains one to four tubular ultrasound transducers made of piezoceramics with adjustable strength and heating time intervals. It was also fabricated into a fan shape to provide directional ablation of a specific angular sound area or the periphery of the target area, selectively destroying the target tissue, while preserving critical tissues. A bio-thermal and acoustic model of ultrasonic ablation was reported by Diederich, CJ *et al.*, describing how to control the ablation zone. Conformal directional ablation could be achieved using a sector transducer with greater control over the shape, size and volume of the ablation zone. This will improve the precision of treatment at the edge and reduce damage to nearby normal tissue.

However, although thermal ablation is clinically accepted, it faces limitations in cases where the tumor is located near major blood vessels because of the unacceptable collateral thermal damage. In this case, electrolytic ablation (EA) is a promising non-thermal tumor ablation technique that destroys malignant cells by inducing local pH changes. EA is usually performed by inserting a needle electrode inside the tumor, and then applying a direct current (DC), which induces electrolysis and produces a local pH change around the electrode. S. Islam *et al.* reported a US-driven implantable electrolytic ablation microprobe (Fig. 20), which allowed wireless controlled device on–off and fractionated doses over a longer time to improve the clinical relevance of electroacupuncture.[126,127] The wireless EA microprobe consists of a piezoelectric US receiver, a rectification circuit, and a pair of platinum electrodes. Once implanted *via* a minimally invasive procedure, the microprobe could remain in the solid tumor and be reused as needed. US efficiently delivered energy to millimeter-scale devices implanted deep in the soft tissues of the body, a size (millimeter-scale) that is not possible with traditional induction wireless powering methods. In addition, ultrasound had an operating range greater than 10 cm, which was more efficient in power delivery than conventional induction power at the millimeter scale and was less sensitive to angular deviations between the transmitter and receiver. Fig. 20B shows the relevant chemical reactions and pH changes around the microprobe after applying a direct current or ultrasonic-induced current. By exploring the relationship between the current and voltage of the microprobe under different ultrasound intensities, the optimal ultrasound intensity was found (Fig. 20C). The results showed that the microprobe is capable of generating a direct current of 90 A between the electrodes at 5 V at low-intensity ultrasound (about 190 mW cm^{-2}). The pH change measured by agarose gel simulating tissue was used to explore the effect of EA induced by ultrasound at the cellular level. A schematic diagram of the device is shown in Fig. 20D. The color change of phenolphthalein indicated that the microprobe formed an acidic environment around the anode (pH $<$ 2), while forming an acidic environment around the cathode (pH $>$ 12.9) after ultrasound treatment. The change in acidity and alkalinity caused the agarose gel-simulated tissue to expand to a volume of 0.8 cm^3 at a swelling rate of 0.5 mm^3 min^{-1} within 1 h (Fig. 20E). The ability of microprobe-mediated electrolytic ablation was demonstrated *in vitro* in cancer cells (Fig. 20F) and isolated mouse liver (Fig. 20G).

5.9 Imaging contrast agent

Numerous imaging techniques including X-ray computed tomography (CT), magnetic resonance imaging (MRI), nuclear medicine imaging (positron emission computed tomography, PET; and single photon emission computed tomography, SPECT), ultrasound imaging, optical imaging, and microwave imaging have been developed and applied in tumor diagnosis or guiding treatment. However, it has been clinically found that imaging signals of different tissues may overlap, such as between different normal tissues or between normal tissues and diseased tissues, leading to difficulties in diagnosis and guidance. Thus, they can only be detected when the lesion has developed to the extent that it has changed the organ morphology, location and enlarged itself to give abnormal sensation. The adoption of new techniques and methods to improve the contrast,

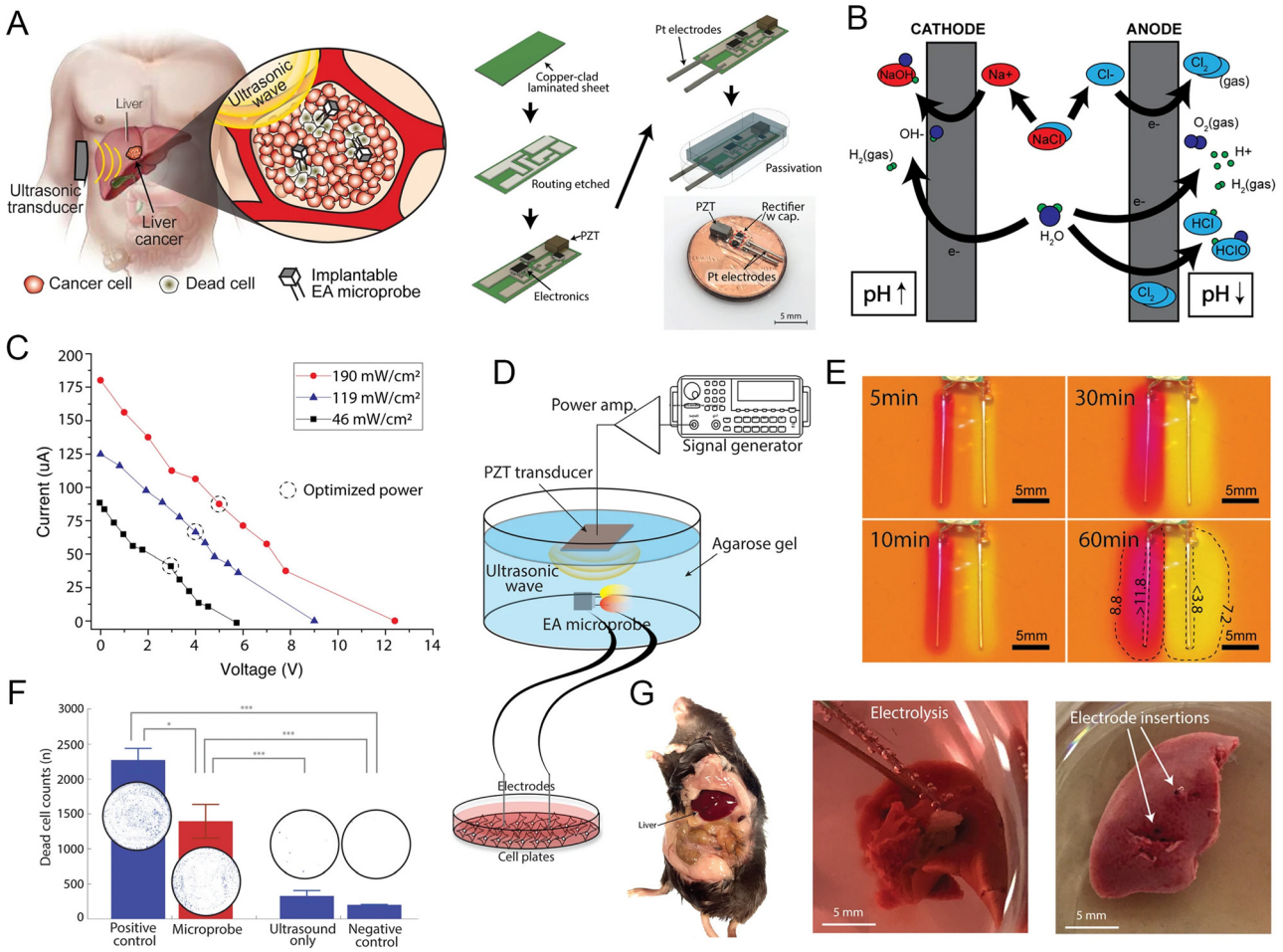

Fig. 20 (A) Schematic view and fabrication process of wireless electrolytic ablation microprobe. (B) Basic chemical reactions during electrolysis ablation. (C) Relationship lines between current and voltage at three ultrasonic intensities. (D) Schematic diagram of the experimental setup for the cell ablation process *in vitro*. (E) Phenolphthalein discoloration indicates the change in pH around the cathode (left) and anode (right) after sonication for different times. The extent of ablation zone extension was indirectly illustrated in a 20 G needle. (F) Cell viability of HMT3522 S1 breast cancer under different treatment: the positive control (electrolysis with DC power source), microprobe, and ultrasound-only and negative control (no action). (G) Mouse liver after electrolysis ablation: control group (left, no action) and microprobe group (ultrasonic for 30 min with 190 mW cm^{-2}).[127] Copyright 2020, Nature.

spatial resolution and temporal resolution of biomedical images is one of the biomedical engineering trends, the main approach of which is to improve the accuracy of diagnosis by injecting contrast agents to alter the local characteristics of tissues and improve the imaging contrast. Nevertheless, the diagnostic methods based directly on the inherent properties of these piezoelectric nanomaterials still need to be developed in current research. Here, we summarize the published work on piezoelectric materials in tumor imaging (Table 4).

5.9.1 X-Ray computed tomography (CT). According to the mechanism of CT imaging, X-rays collide with electrons outside the nucleus of material atoms, resulting in energy loss. By detecting the difference in energy before and after X-rays penetrate an object, the magnitude of the object's ability to absorb X-rays can be found, which is the magnitude of the attenuation coefficient. Therefore, the basis of CT imaging is attenuation coefficient imaging, where it can be simply stated that the larger the atomic number of the elements contained in a material, the greater its potential as a CT contrast agent. Our group reported the effect of the Bi_2MoO_6 piezoelectric material as an acoustic sensitizer and CT contrast agent (Fig. 21),[128] and the results of *in vitro* experiments showed a positive linear relationship between the Hounsfield unit (HU) value and Bi_2MoO_6 (BMO) concentration, and the deposition of the material at the tumor site over time and the metabolic process in the liver could be observed from the *in vivo* CT signal change. Stephen O'Brien *et al.* verified that the CT values of barium titanate (40–50 mg mL^{-1}) before and after citric acid modification were significantly greater than that of soft tissues, and both the solution and mice showed CT enhancement *in vivo*.[130]

5.9.2 Magnetic resonance imaging (MRI). Magnetic resonance imaging is a relatively new medical imaging technology, which was only first officially used internationally in 1982 and is now commonly used in clinical medical test imaging. It uses static and radiofrequency magnetic fields to image human tissues. Compared to CT and PET imaging, the imaging process has the safety of no radiation damage and the flexibility of

Table 4 Application of piezoelectric materials as imaging contrast agents

Materials	Size	Operating principle	Outcome	Ref.
X-Ray computed tomography (X-CT)				
Bi_2MoO_6–PEG	Ultrathin 2D nanoribbons approximately 79.26 nm long, 19.95 nm wide, and 6.03 nm thick	High atomic number elemental Bi with a K-edge of 90.5 keV, images obtained from ultrahigh X-ray attenuation (5.74 cm^2 kg^{-1} at 100 keV)	A positive linear relationship between HU value and concentration. Deposition in the tumor site and the metabolic process in the liver were observed from CT signal *in vivo*.	128
$BaTiO_3$	$BaTiO_3$ with size of 8 nm; $BaTiO_3$@-SiO_2 with size of 30–90 nm.	High atomic number elemental Ba with a K-edge of 39 keV	Significant CT enhancement of $BaTiO_3$ (40–50 mg mL^{-1}) before and after citrate modification.	130
Magnetic resonance imaging (MRI)				
$BiFeO_3$	An average size of 48.7 nm	MRI based on element Fe; CT based on element Bi.	A positive linear relationship between CT signal and concentration, the slope was 16.33 HU g L^{-1}, which was higher than the signal with the same concentration of iohexol.	132
ZnO–Gd–DOX	Approximately 3 nm	Element Gd with unpaired electron	Under a 0.55 T MRI system, the longitudinal relaxivity r_1 was 49.5 mM^{-1} s^{-1} and the transverse relaxivity r_2 was 63.0 mM^{-1} s^{-1}.	89
Second harmonic imaging (SHG)				
Bioharmonophores	Different bioharmonophores originating from protein self-assembly of pentalanines, triphenylalanines, and triphenylalanines. Spherical nanoparticles with a diameter ranging from 50 to 150 nm.	Excitation with a 1030 nm laser, pulse width 190 fs, and 200 kHz repetition rate, 60 mW power, over a 36 μm focal spot (30 mJ cm^{-2}). Signal was detected with a rotating PMT and filter (515 + 10, Chroma) at angles between −90 and 90.	Bioharmonophores functionalized with tumor cell surface markers can detect individual cancer cells in zebrafish embryos with high sensitivity.	136
$BaTiO_3$@Au	Spherical nanoparticles with a diameter of smaller than 100 nm.	Tumors or skin excited with 820 nm, 45 mW cm^{-2}, <100 fs pulse; images were acquired at a scanning frame rate of 4 s and 3 channels were used: 425 ± 30 nm for SHG imaging, 525 ± 45 nm for TPL imaging, and 607 ± 70 nm for TAMRA-dextran fluorescence imaging.	The dual-mode imaging of nanoparticles was used to observe the thermo-induced effect on tumor blood vessels and the distribution of tumor vasculature *in vivo* in real time.	137

tomography in various orientations. MRI imaging covers multiparametric features such as proton density, relaxation and weighted imaging, reflecting human organ malfunctions and early lesions from within the human molecule. Based on these advantages, MRI imaging has become one of the common tests in contemporary clinical diagnosis. However, it was found that the relaxation time between tissues interfered with each other. Therefore, the injection of contrast agent can improve the local relaxation characteristics of the tissue and improve the imaging contrast, thus improving the diagnostic accuracy. However, the existing contrast agent signal contrast and image resolution are poor. Therefore, researchers have investigated new MRI contrast agents to improve the image resolution and enhance signal contrast.

MRI contrast agents are a class of chemically synthesized substances with higher density than that of living tissue, which are usually paramagnetic or superparamagnetic substances such as Fe, Mn, and Gd with multiple unpaired electrons. The contrast agents themselves do not produce signals when they enter the animal body, and subsequently when they approach the hydrogen atoms in resonance, they can interact magnetically with the hydrogen nuclei, effectively changing the magnetic field in which the protons are located. By causing changes in the longitudinal relaxation rate ($1/T_1$) and transverse relaxation rate ($1/T_2$) of water protons in local tissues *in vivo*, the contrast with surrounding tissues is improved, thus achieving contrast purposes. Moreover, antimagnetic and paramagnetic contributions are additions in the presence of paramagnetic substances. For example, Zhang and Helmuth Möhwald *et al.* utilized Gd ions to act as MRI contrast agents (Fig. 22A and B), achieving synergy between fluorescence imaging and MRI, and MRI guidance for ultrasound and photothermal therapy, respectively.[89,131] The development of a fully driven robotic assistant for precise conformal ablation of brain tumors guided by MRI using interstitial high-intensity ultrasound ablation probes was reported. Our group explored bismuth ferrate as a nanocatalyst for MRI/CT/fluorescence multimodal imaging-guided ultrasound-enhanced tumor therapy (Fig. 22C).[132] The *in vitro* and *in vivo* imaging results showed significant signal changes in T_1/T_2-weighted MRI with the interaction of BFO with exogenous/endogenous hydrogen peroxide.

5.9.3 Second harmonic imaging (SHG). Fluorescence microscopy has profoundly changed the study of cellular and molecular biology, which can be used to track characteristic products that are labeled during and after interaction. The ability of fluorescent dyes to absorb and emit light at different wavelengths allows them to produce striking contrast, enabling single-molecule detection and tracking under ideal circumstances. However, in many experimental environments, fluorescent probes do not reach their theoretical values due to dye

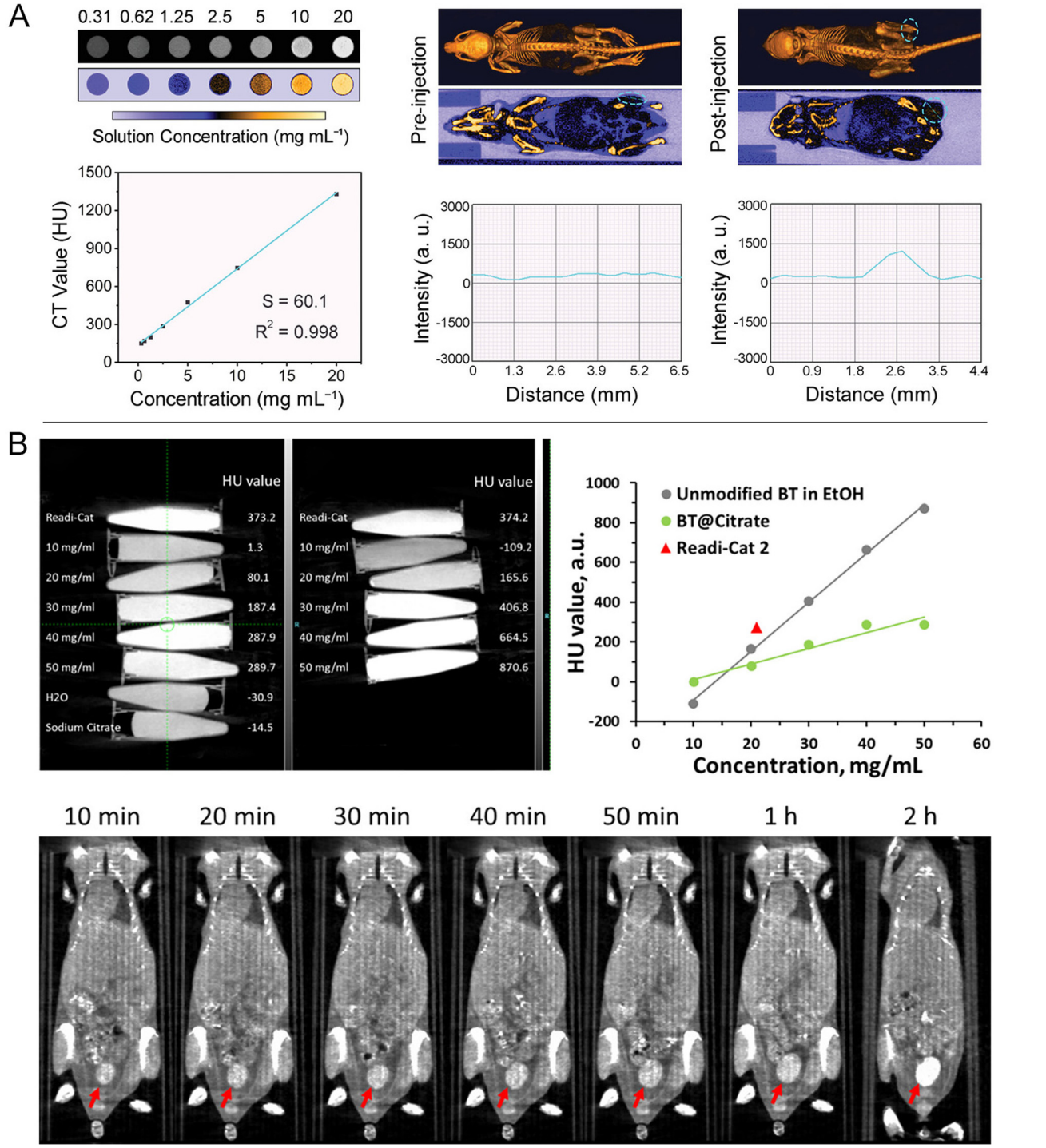

Fig. 21 *In vitro* and *in vivo* CT imaging of Bi_2MoO_6 NR (A) and $BaTiO_3$@citrate solutions (B).[128,130] Copyright 2020, Wiley-VCH and the American Chemical Society, respectively.

bleaching and saturation of the dye signal with the tissue's own fluorescence.[133] The interaction with the nonlinear material merges into a new photon of twice the frequency, and two photons of the same frequency (ω) excite the piezoelectric crystal to produce a precisely double-frequency (2ω) emitted light, *i.e.*, a new photon with half the wavelength (Fig. 23A).[134] For example, a laser with an output wavelength of 694 nm produces 347 nm UV light when passing through a quartz crystal. The imaging established using this emitted light signal is called second harmonic imaging, which is nonlinear optical imaging with high spatial resolution and high imaging depth and avoids the fluorescence bleaching effect in two-photon fluorescence imaging and allows for improved signal-to-noise ratio and unparalleled long-term photostability for imaging.[135]

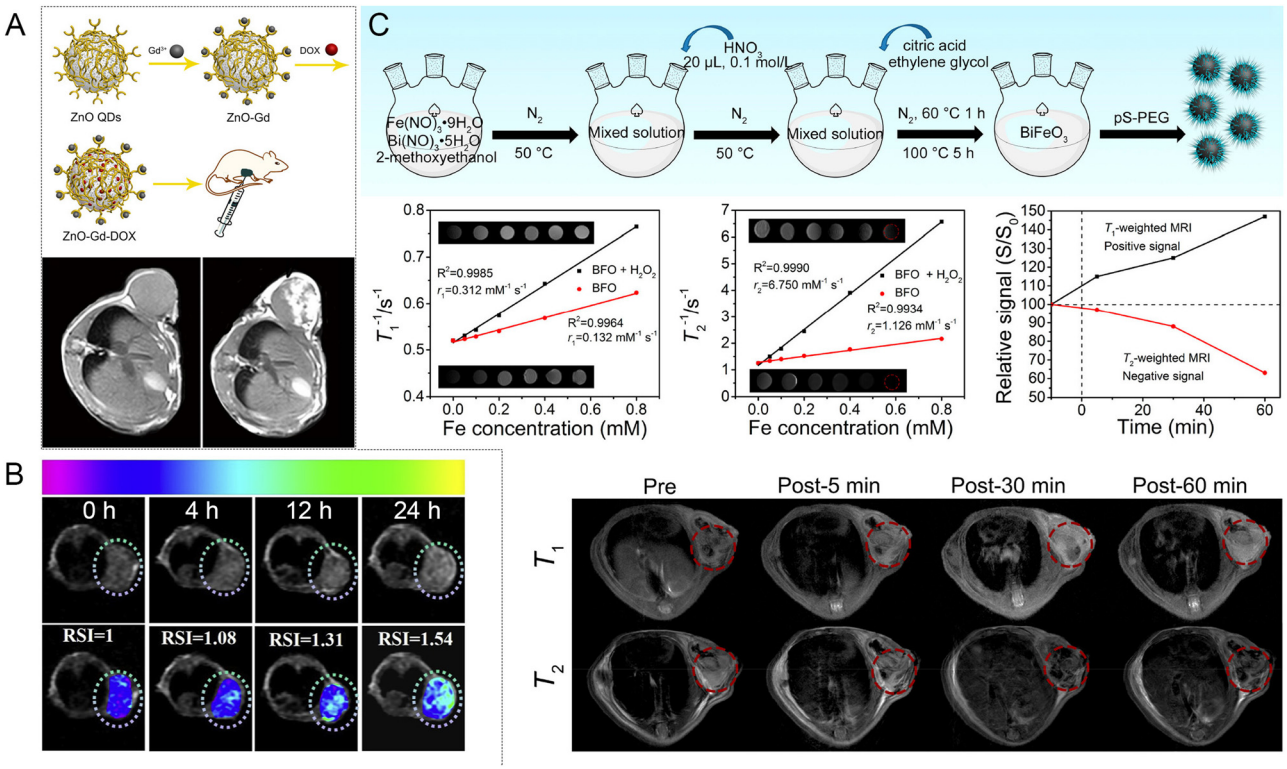

Fig. 22 *In vivo* MRI of ZnO–Gd–DOX (A) and D-ZnO_x:Gd NRs (B).[89,131] Copyright 2020, Wiley-VCH and Elsevier. (C) Schematic diagram of the process for the synthesis of BFO NCs and MRI results *in vitro* and *in vivo*.[132] Copyright 2020, the American Chemical Society.

Periklis Pantazis *et al.* demonstrated the above-mentioned advantages of nanoprobes generating second harmonics if used for *in vivo* imaging based on inorganic SHG nanoprobes, which can avoid many limitations of conventional fluorescent probes.[136] However, Periklis Pantazis' team had concerns about their long-term health, causing them to develop biodegradable harmonophores, which consisted of polymer-encapsulated, self-assembled peptides that produce strong SHG signals comparable to inorganic SHG nanoprobes (Fig. 23B). Moreover, the bioharmonophores, when functionalized with tumor cell surface markers, could detect a single cancer cell in zebrafish embryos with high sensitivity. We also propose future research perspectives to investigate its potential for image-guided surgery, detection of cancer stem cells, and improved sensitivity of deep tissue single-molecule detection. Piezoelectric materials have a non-centrosymmetric structure and are typical materials that can generate second harmonics. Daniel S. Kohane *et al.* reported that $BaTiO_3$@Au core–shell nanoparticles smaller than 100 nm convert a portion of photon energy into heat to ablate tumors upon NIR light irradiation, and simultaneously enable the combination of two-photon imaging and SHG imaging (Fig. 23C and D).[137] The dual imaging capability enabled the real-time *in vivo* tracking of the $BaTiO_3$@Au core–shell nanoparticles and observation of their thermally induced effects on tumor vasculature, and helped to investigate the distribution of the nanoparticles in relation to the morphology of the tumor vascular system during photothermal ablation. Piezoelectric nanoparticles (BTO and BFO) used as SHG-labeled probes provide ideal signal transmission, which is essential for *in vivo* imaging of deep tissues, owing to the fact that SHG imaging uses near-infrared incident light to produce contrast, which neither bleaches nor flickers and produces signals that do not saturate with increasing irradiation intensity.[81] SHG has a wide range of applications in imaging, but achievements in the field of anti-tumor are not common,[138–140] and thus the application of second harmonic imaging in the early diagnosis and diagnosis of tumors remains to be developed.

5.9.4 Microwave imaging (MWI). Microwave imaging is divided into microwave tomography (MWT) and microwave thermoacoustic tomography (MITT). Both tomography methods are realized with microwave excitation, but the tomography mechanism is different. The principle of MWT is that after low-power microwave excitation of the measured object, it detects the scattered field. The scattering field is related to the complex dielectric constant distribution inside the subject. Through the measurement of the scattered field, the relative permittivity and conductivity (*i.e.*, complex permittivity) of the measured object is obtained, and the corresponding information is processed to obtain an MWT image of the target inside the measured object. Therefore, the diagnostic potential of MWT is based on the comparison of dielectric properties between physiological and pathological tissues.[141] Consequently, MWT may be suitable for the non-invasive assessment of various soft tissue functional and pathological conditions, including malignant tissues, which generate a scattered field, and imaging is performed. However, considering the complexity of MWT, especially the

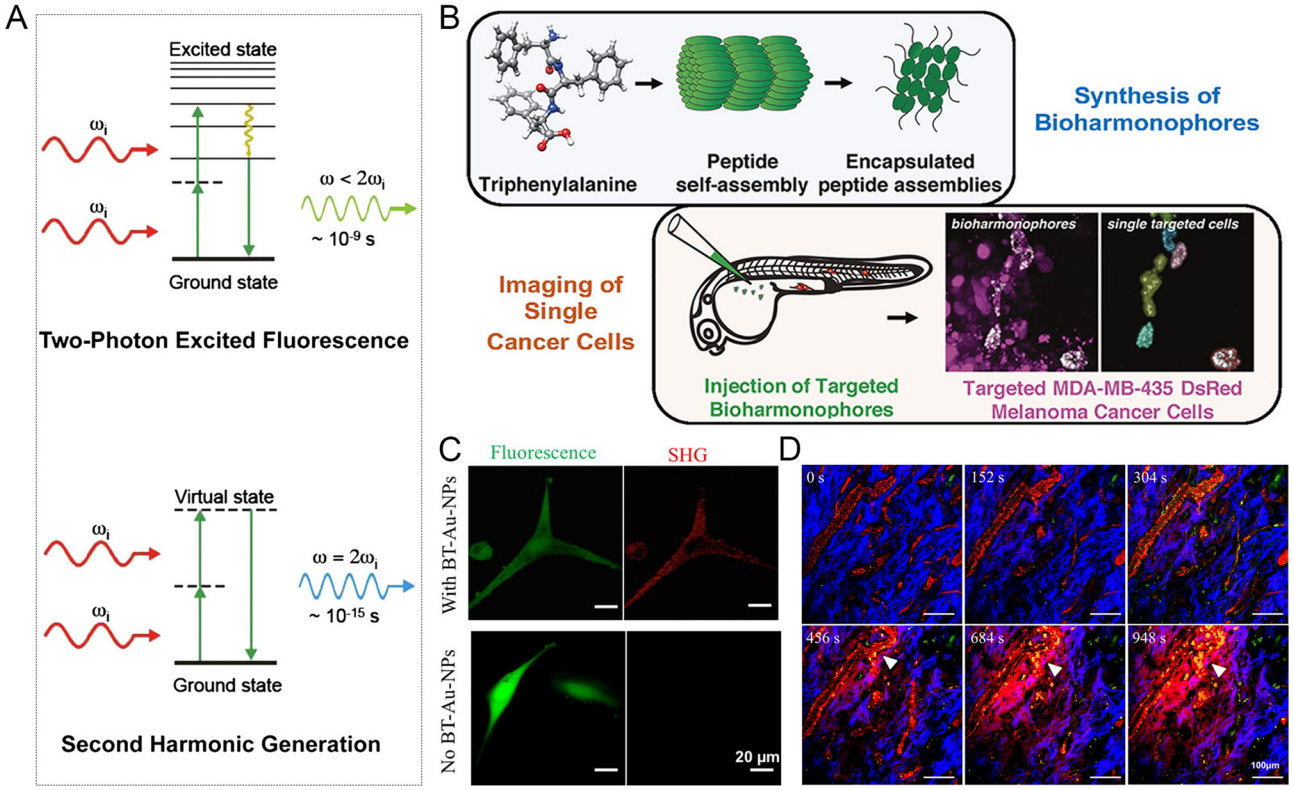

Fig. 23 (A) Two-photon excited fluorescence *versus* SHG.[134] Copyright 2010, National Academy of Sciences. (B) Synthesis process of bioharmonophores and imaging targeting single cancer cells *in vivo*.[136] Copyright 2021, the American Chemical Society. (C) Comparison results of fluorescence and SHG images. (D) Combination of TAMRA-dextran-labeled vascular distribution (red), SHG signal (blue) and two-photon luminescence (green) for BT-Au-NPs.[137] Copyright 2018, Elsevier.

heterogeneity of human tissues, which generates spurious interference largely affecting the effectiveness of microwave medical imaging, there is a need to enhance the original dielectric constant contrast. The dielectric constant is one of the main characteristic parameters of piezoelectric materials. Semenov, S. *et al.* used ferroelectric nanoparticles as contrast agents to improve the contrast of MWT by enhancing the dielectric constant at the tumor site. Based on a simplified model of thoracic pulmonary tumor with computer simulation, the preliminary experimental results demonstrated that the ferroelectric nanoparticles significantly enhanced the diagnostic ability of MWT. However, the delivery of the contrast agent to the tumor site in a targeted manner is also a problem to be solved. Chen *et al.* loaded a microblogging contrast agent in biocompatible flagellated magnetotropic bacteria (MTB) based on micro-nano-bio-robotic technology (Fig. 24), where externally generated magnetic field gradients guide the assemblies to travel along a pre-planned route to the tumor site in the body.[142] This strategy to detect and localize malignant tumors in breast tissue improves the contrast of MWT for better estimation of the tumor size. The feasibility of this tumor diagnostic approach has been demonstrated using an anatomical digital breast model as a platform.

The principle of MWTT is that after the microwave pulse irradiates an organism, its tissue absorbs part of the microwave energy rapidly and converts it into heat, thus increasing the temperature of the irradiated tissue. Since there are differences in dielectric constants between different tissues, the degree of microwave absorption varies, and a temperature gradient is formed on the surface of the relative tissues. Considering that electromagnetic waves travel much faster than sound waves, it can be assumed that the thermal expansion caused by microwave irradiation occurs instantaneously.[143] Biological tissues generate strain, which propagates thermal acoustic waves outward, and finally the thermal acoustic signal is detected and processed by an ultrasonic transducer. The basis of thermoacoustic imaging is to calculate the spatial distribution of the thermal acoustic source or microwave absorbance by the reverse of the thermoacoustic signal. The microwave thermoacoustic imaging process is similar to ultrasound imaging if optical radiation is used instead of microwave radiation, which is the photoacoustic imaging process. Wang *et al.* investigated MWTT over a wide range of electromagnetic frequencies and tumor locations to simulate the piezoelectric signal associated with thermoacoustic contrast.[144] The relationship between the imaging resolution and experimental parameters was investigated. Experimental enhancement of the image contrast was achieved using a gain compensation method based on electromagnetic attenuation. Microwave thermoacoustics combines the advantages of better contrast in microwave imaging and

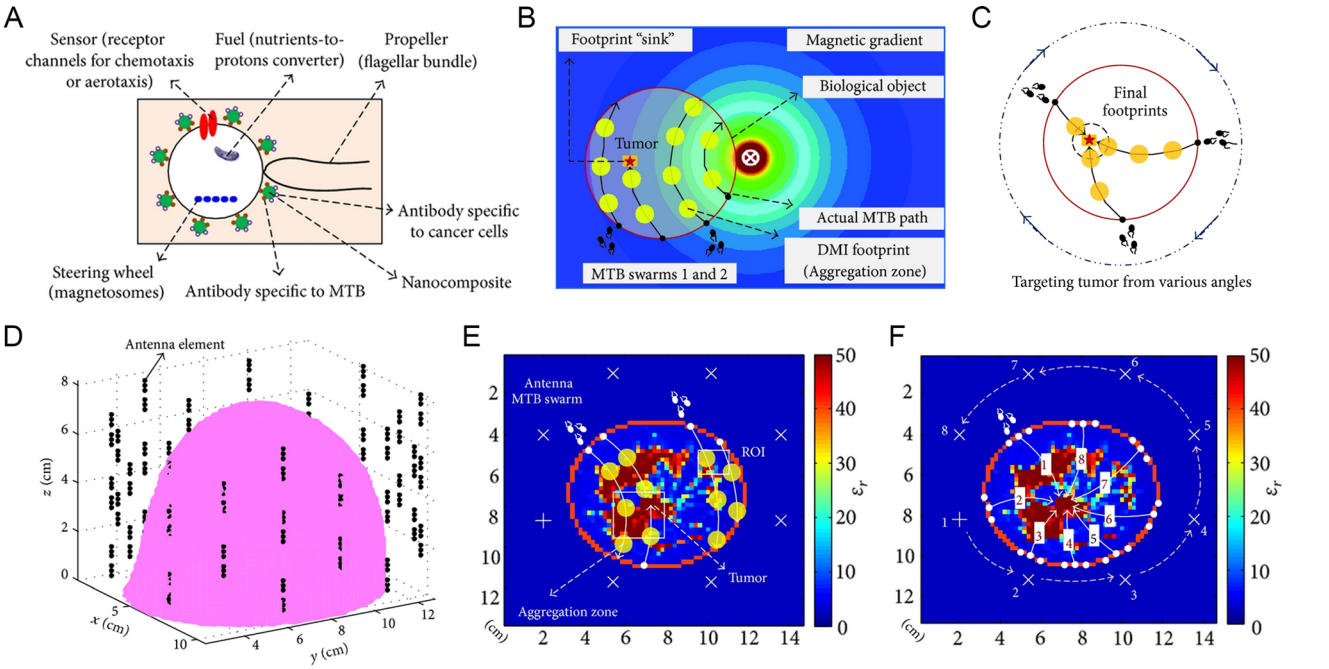

Fig. 24 (A) Key functional elements of MTB. Paths (B) and angles (C) of targeting the tumor by the functionalized MTB microrobot. (D) Illustration of the tumor sensing and diagnosis system using a configuration. (E) Dielectric profile for the coronal cross-section through the third antenna ring. (F) Size estimation of the tumor by targeting it from different angles.[142] Copyright 2013, Hindawi.

good spatial resolution in ultrasound imaging. In the current research progress, the study of piezoelectric materials as contrast agents is rare, but they are commonly used and exhibit an excellent performance as transducers. Thus, almost all diagnostic and therapeutic devices possess a signal conversion recognition part composed of a variety of piezoelectric materials. In addition, piezoelectric materials may also be present in the quantitative detection and signal emitting part, and developers usually choose the corresponding piezoelectric, pyroelectric or ferroelectric materials according to the desired properties. The rapid development of nanorobotics will promote the intersection of materials and intelligent control, which is expected to develop precise and intelligent therapies based on piezoelectric materials in the future.

6 Biosafety and metabolic pathways

Biosafety and metabolic pathways are primary concerns before novel nanomedicine research. Good biocompatibility and biosafety are prerequisites for the feasibility of employing piezoelectric materials in biomedical applications. In particular, research on piezoelectric series materials as nanomedicine has just started, and thus it is necessary to evaluate and discuss their biological safety. In the past, researchers have developed and optimized synthetic techniques to control the size and stability of materials. In this case, the biocompatibility of nanomedicine can be achieved by surface modification engineering. The pharmacokinetics and pharmacokinetics of nano drugs can also be improved and their toxicity reduced. Some piezoelectric materials are inherently biodegradable. The stability of a material is affected by the physiological environment, such as pH, and the concentration of hydrogen peroxide or glutathione, forming degradation phenomena in response to the tumor microenvironment. Piezoelectric materials can be rapidly cleared from the organism through a degradation process, which reduces concerns about their long-term retention and toxicity. Besides, the degraded ions can also play a therapeutic role. For non-biodegradable piezoelectric materials, nano-drugs can be PEGylated or electrically neutral by regulating their surface properties to achieve the "stealth" effect. Coating the surface of a toxic material with a biocompatible material increases the safety of the piezoelectric material. Adjusting the structure and properties of the coating also has an impact on the interaction of a piezoelectric material with an external stimulus field. However, Piezoelectric materials had no significant toxicity to mice in the short term, but their long-term effects on the main organ functions need to be discussed individually. This needs to be verified by hematology, serum biochemistry, and histopathology.

The morphology, aspect ratio, surface charge, and surface functional groups of materials can affect the penetration in the tumor and clearance time *in vivo*.[145] Metabolic studies have shown that the clearance behavior of materials from the organism mainly relies on two metabolic pathways, *i.e.*, the liver and kidney. The liver and kidney similarly remove materials and are both constrained by the physicochemical properties of the material, such as surface charge, size, and height of morphology. After administration and entry into the vascular circulation, the materials can be excreted through the kidneys

in the urine. Materials less than 6 nm in diameter can efficiently pass through the pores of the renal glomeruli, and thus rapidly removed from the circulation through the bladder and urine. The rate of removal depends on their surface charge, where particles with a positive charged are removed faster than negatively charged or neutral particles. After entering the liver through the blood circulation, materials are internalized by Kupffer cells, a specialized macrophage in the liver. Kupffer cells internalize materials of different sizes by phagocytosis or other endocytic mechanisms. Materials smaller than 200 nm can be metabolized by interaction with hepatocytes *via* endocytosis. Hepatocytes are efficient in the internalization of anionic materials, whereas Kupffer cells prefer cationic materials. The precise clearance mechanism depends on the interaction between the inorganic materials and intracellular components. Materials larger than 200 nm are filtered through the spleen and cleared by the reticuloendothelial system (RES). In the case of particles larger than 1 mm, they are trapped in the upper respiratory tract and rapidly removed by mucociliary transport. Therefore, the prerequisite for piezoelectric materials to be used as injectable nanomedicine is to meet the size of biological metabolism. The effect of the microscopic shape of a material on its metabolism is a consensus for inorganic materials. Conversely, there are no reports on the relationship between the morphology of piezoelectric materials and metabolism. The previous results on the biodistribution of silica after intravenous injection can be used as a reference. After entering the body of a mouse for some time, monodisperse silicon dioxide was mainly distributed in the lung, spleen, and liver, and its particle shape significantly affected its dispersion ratio. Short rod-shaped monodisperse silicon dioxide was increasingly found in the liver, while long rod-shaped monodisperse silicon dioxide was more common in the spleen. Monodisperse silicon dioxide was cleared from the body mainly through urine and feces, where its shape was the main reason for its clearance rate. The short rod-shaped monodisperse silicon dioxide was cleared faster than the long rod-shaped monodisperse silicon dioxide through both excretion pathways. We suppose that the micro-shape design of piezoelectric materials will also affect the biological safety and metabolism of piezoelectric materials. Future researchers must explore the effects of developing the morphology of piezoelectric materials on their metabolic profile. Finally, controlling the appropriate dosage is the purpose of the clinical medication. It is immoral to say that drugs are not toxic without reference to the amount used. For example, selenium released from P-KNNSe intake is safe at low doses below 5 ppm. Simultaneously, health authorities are placing materials under ''special'' observation, taking appropriate measures to assess their toxicological characteristics. This process also requires close collaboration among investigators, regulators, and clinicians.

7 Summary and outlook

Piezoelectric materials have attracted extensive attention in the medical field because of their electromechanical coupling properties. Applications in tissue regeneration, nerve stimulation, drug delivery, wound healing, dynamic therapy, and tooth whitening have been developed in eye-opening ways.[5,9,80,146–148] The electrical signals generated by piezoelectric materials were used for power supply, information transmission, electrical stimulation, control of valve channels, change in charge carrier behavior, and participation in redox reactions. Inspired by these research results, the construction of intelligent closed-loop anti-tumor systems based on piezoelectric materials integrating sensing, detection, treatment, diagnosis, and treatment has become a future development trend. It is noteworthy that piezoelectric materials can effectively integrate force, acoustic, magnetic, thermal, and electrical properties. This offers a solid material foundation for the future creation of intelligent therapeutic systems with powerful functions. However, the medical applications of the developed piezoelectric materials have mostly remained at the proof-of-concept or cellular and animal level. The realization of their excellent performance in the human body needs more exploration and practice. The first is if the current piezoelectric materials are safe for biomedical use, and the second is whether their properties are feasible. Additionally, it is necessary to clarify the connections among substances, outside stimuli, and the organism, while their pharmacological information at the cellular, animal, and clinical levels. Therefore, the use of piezoelectric properties for therapeutic applications remains a challenge.

(1) Clarification of the relationship between the material and the organism with a deeper investigation of the mechanism

The exploration of piezoelectric materials as therapeutic reagents in the field of antitumor therapy is still in its infancy, and the relationship between the interaction between biopiezoelectric materials and biological organisms is still uncertain. Thus far, most reports have focused mainly on the improvement of dynamic therapeutic effects, and the reactions involving electrons and holes or positive and negative polarized charges to generate reactive oxygen species are mostly oxygen-dependent. However, only a small portion of the tumor tissue contains oxygen, except for the hypoxic and necrotic regions, and therefore the lack of consideration of the complexity of the tumor microenvironment is the main reason why most nanomedicines have not been successful in clinical trials. The mechanism of the interaction between engineered materials and organisms, potential risks, drug toxicology, pharmacokinetics and pharmacodynamics are the areas to be explored in depth in the future.

(2) Improvement in performance of current materials and development of new piezoelectric biomaterials

The unique properties of piezoelectric, pyroelectric and ferroelectric materials offer promise for wireless minimally invasive therapies. However, the sensitivity, strength and stability of the response of the material device after entering the body are key issues in practical applications. For instance, most pyroelectric materials require a relatively large rate of temperature change to convert thermal energy into chemical energy. However, it is

Table 5 Challenges in the clinical application of piezoelectric materials and the pros and cons of the existing strategies

Problems	Existing strategy	Pros	Cons
Accurate measurement of piezoelectric properties of nanomaterials	PFM is a promising method for the detection and quantification the piezoelectric properties of nanomaterials.	High resolution, nondestructive imaging capability and the ability to measure local piezoelectric activity in nanomaterials with complex geometries.	Operating principle makes the PFM response lack of robustness and low accuracy for nanomaterials.
Energy conversion efficiency from external stimuli to electrical signals	(1) Internal cause: modify materials or explore new materials. (2) External cause: *in situ* measurements or simulation calculations.	(1) Radically improving performance. (2) Finding the optimal dose, clarifying the uncertainty of the exposure process, and increasing reproducibility and contrast.	Environmental complexity affects the prediction results.
Unclear mechanism of organism response to piezoelectric stimulation	Using control experiment and blank experiment, and multi-omics method to explore the mechanism.	Superimposition of biological interference was excluded.	Intracellular biochemical pathways triggered by the stimulus are not well defined.
Low efficiency of targeted delivery	According to the characteristics of the delivery barrier, the most suitable piezoelectric nanoarchitecture and augmentation targeting strategy for the treatment of specific diseases are found.	It helps to overcome obstacles and also maximizes the accumulation of drugs in a shorter period.	Increasing the complexity of nanomedicine
Biological safety	Selection of biocompatible or bio-non-degradable materials, or surface modification to increase biosafety.	Increasing the safety of nanomedicine.	Unclear long-term toxicity and organism specificity.

difficult to meet these temperature conditions in the temperature range tolerated by living organisms. Therefore, it is necessary to construct and design more piezo/pyro/ferroelectric biomaterials with tunable properties. Alternatively, new piezo/pyro/ferroelectric materials should be developed to circumvent the high temperature and pressure synthesis conditions and improve the electromechanical coupling performance and energy conversion efficiency of the materials.

(3) Development of new intelligent nanorobotic drug systems

Piezoelectric materials have mature achievements in the fields of sensing, driving and transduction. If the engineering material synthesis aims to integrate sensing, driving or transduction into biodegradable nanorobots, on the one hand, the piezoelectric photoelectric process can be analyzed in real time by *in situ* measurement to determine the electron transfer and reaction pathway, which is complementary to the investigation of the mechanism of material-biological action. On the other hand, it provides multifunctional nanomedicine to achieve precision therapy by leaps and bounds.

This review offers the fundamentals, materials, mechanism and related advances of pyroelectric catalysis, which is expected to serve as a useful guideline for future research in pyroelectric catalysis.

(4) The problems associated with the application of piezoelectric materials in oncology

Electrical stimulation has shown great promise in biomedical applications. The development of piezoelectric materials, pyroelectric materials, and ferroelectric materials in nanomedicine for anti-tumor therapy can broaden the application range of electrical stimulation therapy. Piezoelectric materials can convert energy in the form of force, light, electricity, magnetism, and heat into electrical signals, realizing local wireless control and minimally invasive treatment modalities. This overcomes the limitations of current electrical stimulation, requiring connectors and batteries.[149,150] However, the development of piezoelectric materials as smart nanomedicine is still in its infancy. There are still some challenges in the translation of piezoelectric materials into clinical applications, such as the measurement of piezoelectric properties of nanomaterials, the efficiency of energy conversion from external stimuli to electrical signals, the unclear mechanism of organism response to piezoelectric stimulation, the low efficiency of targeted delivery, and the biological safety. The pros and cons of the existing strategies are presented in Table 5.

This review offers the fundamentals, mechanism and related advances of piezoelectric materials for anti-tumor therapy, which is expected to serve as a useful guideline for future research in piezoelectric assisted anti-tumor therapy.

Author contributions

Y. W. and P. Z. contributed equally to this work.

Conflicts of interest

The authors declare no conflict of interest.

Acknowledgements

Financial supports from the National Natural Science Foundation of China (NSFC, 51972075 and 51902066), a General Financial Grant from the China Postdoctoral Science Foundation (2019M650063), Natural Science Foundation of Heilongjiang Province (ZD2019E004), Natural Science Foundation of Shandong Province (ZR2019ZD29), and the Fundamental Research Funds for the Central Universities are greatly acknowledged.

Notes and references

1 G. Bergers and S.-M. Fendt, *Nat. Rev. Cancer*, 2021, **21**, 162–180.
2 D. Hanahan and R. A. Weinberg, *Cell*, 2011, **144**, 646–674.
3 D. Hanahan, *Cancer Discovery*, 2022, **12**, 31–46.
4 J. S. Arya, M. M. Joseph, D. R. Sherin, J. B. Nair, T. K. Manojkumar and K. K. Maiti, *J. Med. Chem.*, 2019, **62**, 8311–8329.
5 K. Kapat, Q. T. H. Shubhra, M. Zhou and S. Leeuwenburgh, *Adv. Funct. Mater.*, 2020, **30**, 1909045.
6 M. M. Joseph, S. R. Aravind, S. K. George, K. R. Pillai, S. Mini and T. T. Sreelekha, *Eur. J. Pharm. Biopharm.*, 2015, **93**, 183–195.
7 J. Dolai, A. Biswas and N. R. Jana, *ACS Appl. Nano Mater.*, 2022, **5**, 14038–14050.
8 B. Jiang, J. Iocozzia, L. Zhao, H. Zhang, Y. W. Harn, Y. Chen and Z. Lin, *Chem. Soc. Rev.*, 2019, **48**, 1194–1228.
9 Y. Wang, X. Wen, Y. Jia, M. Huang, F. Wang, X. Zhang, Y. Bai, G. Yuan and Y. Wang, *Nat. Commun.*, 2020, **11**, 1328.
10 S. Xu, L. Guo, Q. Sun and Z. L. Wang, *Adv. Funct. Mater.*, 2019, **29**, 1808737.
11 J. Zhang, Z. Pan, F. F. Guo, W. C. Liu, H. P. Ning, Y. B. Chen, M. H. Lu, B. Yang, J. Chen, S. T. Zhang, X. R. Xing, J. Rodel, W. W. Cao and Y. F. Chen, *Nat. Commun.*, 2015, **6**, 6615.
12 S. T. Zhang, F. Yan, B. Yang and W. W. Cao, *Appl. Phys. Lett.*, 2010, **97**, 122901.
13 H. You, Z. Wu, L. Zhang, Y. Ying, Y. Liu, L. Fei, X. Chen, Y. Jia, Y. Wang, F. Wang, S. Ju, J. Qiao, C. H. Lam and H. Huang, *Angew. Chem., Int. Ed.*, 2019, **58**, 11779–11784.
14 T. Zheng, J. Wu, D. Xiao and J. Zhu, *Prog. Mater. Sci.*, 2018, **98**, 552–624.
15 S. Das Mahapatra, P. C. Mohapatra, A. I. Aria, G. Christie, Y. K. Mishra, S. Hofmann and V. K. Thakur, *Adv. Sci.*, 2021, **8**, 2100864.
16 C. Chen, X. Wang, Y. Wang, D. Yang, F. Yao, W. Zhang, B. Wang, G. A. Sewvandi, D. Yang and D. Hu, *Adv. Funct. Mater.*, 2020, **30**, 2005141.
17 M. T. Chorsi, E. J. Curry, H. T. Chorsi, R. Das, J. Baroody, P. K. Purohit, H. Ilies and T. D. Nguyen, *Adv. Mater.*, 2019, **31**, e1802084.
18 D. Kim, S. A. Han, J. H. Kim, J. H. Lee, S. W. Kim and S. W. Lee, *Adv. Mater.*, 2020, **32**, e1906989.
19 V. Thangavel, J. L. David, G. Ehud, B. Ramamoorthy and R. B. Chris, *Adv. Funct. Mater.*, 2022, **32**, 2109492.
20 H. Y. Zhu, Y. Wang, J. Xiao, M. Liu, S. M. Xiong, Z. J. Wong, Z. L. Ye, Y. Ye, X. B. Yin and X. Zhang, *Nat. Nanotechnol.*, 2015, **10**, 151–155.
21 M. Wu, Y. X. Wang, S. J. Gao, R. X. Wang, C. X. Ma, Z. Y. Tang, N. Bao, W. X. Wu, F. R. Fan and W. Z. Wu, *Nano Energy*, 2019, **56**, 693–699.
22 M. Pohanka, *Talanta*, 2018, **178**, 970–973.
23 G. Selvolini and G. Marrazza, *Sensors*, 2017, **17**, 718.
24 F. Ju, Y. H. Yun, Z. Zhang, Y. Y. Wang, Y. M. Wang, L. Zhang and B. Chen, *Smart Mater. Struct.*, 2018, **27**, 115039.
25 Y. Q. Fu, J. K. Luo, N. T. Nguyen, A. J. Walton, A. J. Flewitt, X. T. Zu, Y. Li, G. McHale, A. Matthews, E. Iborra, H. Du and W. I. Milne, *Prog. Mater. Sci.*, 2017, **89**, 31–91.
26 C. H. Chuang, T. H. Li, I. C. Chou and Y. J. Teng, *Sens. Actuators, A*, 2016, **244**, 299–309.
27 C. Chi, X. Sun, N. Xue, T. Li and C. Liu, *Sensors*, 2018, **18**, 948.
28 Z. Liu, L. L. Xu, Q. Zheng, Y. Kang, B. J. Shi, D. J. Jiang, H. Li, X. C. Qu, Y. B. Fan, Z. L. Wang and Z. Li, *ACS Nano*, 2020, **14**, 8074–8083.
29 H. L. You, X. X. Ma, Z. Wu, L. F. Fei, X. Q. Chen, J. Yang, Y. S. Liu, Y. M. Jia, H. M. Li, F. F. Wang and H. T. Huang, *Nano Energy*, 2018, **52**, 351–359.
30 Y. Chen, G. Gao, J. Zhao, H. Zhang, J. Yu, X. Yang, Q. Zhang, W. Zhang, S. Xu, J. Sun, Y. Meng and Q. Sun, *Adv. Funct. Mater.*, 2019, **29**, 1900959.
31 X. Dai, B. C. Heng, Y. Bai, F. You, X. Sun, Y. Li, Z. Tang, M. Xu, X. Zhang and X. Deng, *Bioact. Mater.*, 2021, **6**, 2029–2038.
32 W. Deng, Y. Zhou, A. Libanori, G. Chen, W. Yang and J. Chen, *Chem. Soc. Rev.*, 2022, **51**, 3380–3435.
33 S. Li, Z. C. Zhao, J. Z. Zhao, Z. T. Zhang, X. Li and J. M. Zhang, *ACS Appl. Nano Mater.*, 2020, **3**, 1063–1079.
34 Y. Zhang, Y. Liu and Z. L. Wang, *Adv. Mater.*, 2011, **23**, 3004–3013.
35 C. Y. Wang, N. Tian, T. Y. Ma, Y. H. Zhang and H. W. Huang, *Nano Energy*, 2020, **78**, 105371.
36 Z. Liang, C. F. Yan, S. Rtimi and J. Bandara, *Appl. Catal., B*, 2019, **241**, 256–269.
37 X. Zhou, B. Shen, A. Lyubartsev, J. Zhai and N. Hedin, *Nano Energy*, 2022, **96**, 107141.
38 Z. L. Wang and W. Wu, *Natl. Sci. Rev.*, 2013, **1**, 62–90.
39 Z. L. Wang, *Adv. Mater.*, 2012, **24**, 4632–4646.
40 Z. L. Wang, R. Yang, J. Zhou, Y. Qin, C. Xu, Y. Hu and S. Xu, *Mater. Sci. Eng., R*, 2010, **70**, 320–329.
41 S. Tu, Y. Guo, Y. Zhang, C. Hu, T. Zhang, T. Ma and H. Huang, *Adv. Funct. Mater.*, 2020, **30**, 2005158.
42 W. Z. Wu and Z. L. Wang, *Nat. Rev. Mater.*, 2016, **1**, 16031.
43 L. Pan, S. Sun, Y. Chen, P. Wang, J. Wang, X. Zhang, J.-J. Zou and Z. L. Wang, *Adv. Energy Mater.*, 2020, **10**, 2000214.
44 P. Lin, C. Pan and Z. L. Wang, *Mater. Today Nano*, 2018, **4**, 17–31.
45 H. Li, Y. Sang, S. Chang, X. Huang, Y. Zhang, R. Yang, H. Jiang, H. Liu and Z. L. Wang, *Nano Lett.*, 2015, **15**, 2372–2379.
46 J. Shi, M. B. Starr and X. Wang, *Adv. Mater.*, 2012, **24**, 4683–4691.
47 A. Cafarelli, A. Marino, L. Vannozzi, J. Puigmarti-Luis, S. Pane, G. Ciofani and L. Ricotti, *ACS Nano*, 2021, **15**, 11066–11086.
48 M. Y. Wang, B. Wang, F. Huang and Z. Q. Lin, *Angew. Chem., Int. Ed.*, 2019, **58**, 7526–7536.
49 S. Raufeisen, P. Neumeister, J. R. Buchheim, M. Stelter and P. Braeutigam, *Phys. Chem. Chem. Phys.*, 2020, **22**, 23464–23473.

50 J. Wu, N. Qin, B. W. Yuan, E. Z. Lin and D. H. Bao, *ACS Appl. Mater. Interfaces*, 2018, **10**, 37963–37973.
51 H. You, Z. Wu, L. Wang, Y. Jia, S. Li and J. Zou, *Chemosphere*, 2018, **199**, 531–537.
52 Z. Wu, W. Luo, H. Zhang and Y. Jia, *Appl. Surf. Sci.*, 2020, **513**, 145630.
53 R. J. Wang, C. Y. Wang, Y. T. Feng and C. Tang, *Nano Energy*, 2018, **53**, 906–915.
54 T. Kimura, *J. Ceram. Soc. Jpn.*, 2006, **114**, 15–25.
55 J. Peng, W. Liu, J. Zeng, L. Zheng, G. Li, A. Rousseau, A. Gibaud and A. Kassiba, *J. Mater. Sci. Technol.*, 2020, **48**, 92–99.
56 S. Lan, C. Yu, F. Sun, Y. Chen, D. Chen, W. Mai and M. Zhu, *Nano Energy*, 2022, **93**, 106792.
57 X. Zhou, B. Shen, J. Zhai and N. Hedin, *Adv. Funct. Mater.*, 2021, **31**, 2009594.
58 C. H. Li, Y. F. Li, T. T. Yao, L. Zhou, C. R. Xiao, Z. G. Wang, J. X. Zhai, J. Xing, J. Q. Chen, G. X. Tan, Y. H. Zhou, S. J. Qi, P. Yu and C. Y. Ning, *ACS Appl. Mater. Interfaces*, 2020, **12**, 34505–34513.
59 A. Zhang, Z. Liu, B. Xie, J. Lu, K. Guo, S. Ke, L. Shu and H. Fan, *Appl. Catal., B*, 2020, **279**, 118084.
60 A. Dubey, M. E. Castillo, J. Landers, S. Salamon, H. Wende, U. Hagemann, P. Gemeiner, B. Dkhil, V. V. Shvartsman and D. C. Lupascu, *J. Phys. Chem. C*, 2020, **124**, 22266–22277.
61 X. Wen, Z. Chen, E. Liu, X. Lin and C. Chen, *J. Alloys Compd.*, 2016, **678**, 511–517.
62 Y. Miao, W. Tian, J. Han, N. Li, D. Chen, Q. Xu and J. Lu, *Nano Energy*, 2022, **100**, 107473.
63 S. Cheng, Y. Luo, J. Zhang, R. Shi, S. Wei, K. Dong, X. Liu, S. Wu and H. Wang, *Chem. Eng. J.*, 2022, **442**, 136380.
64 C. Wang, F. Chen, C. Hu, T. Ma, Y. Zhang and H. Huang, *Chem. Eng. J.*, 2022, **431**, 133930.
65 P. Wang, X. Li, S. Fan, X. Chen, M. Qin, D. Long, M. O. Tadé and S. Liu, *Appl. Catal., B*, 2020, **279**, 119340.
66 D. Xiang, Z. Liu, M. Wu, H. Liu, X. Zhang, Z. Wang, Z. L. Wang and L. Li, *Small*, 2020, **16**, 1907603.
67 Y. Wei, Y. Zhang, W. Geng, H. Su and M. Long, *Appl. Catal., B*, 2019, **259**, 118084.
68 J. Dolai, A. Biswas, R. Ray and N. R. Jana, *ACS Appl. Mater. Interfaces*, 2022, **14**, 26443–26454.
69 M. Y. Zhang, Q. Y. Hu, K. W. Ma, Y. Ding and C. Li, *Nano Energy*, 2020, **73**, 104810.
70 Y. Wang, L. Zhang, J. Wang, Q. Li, H. Wang, L. Gu, J. Chen, J. Deng, K. Lin, L. Huang and X. Xing, *J. Am. Chem. Soc.*, 2021, **143**, 6491–6497.
71 H.-W. Park, N. D. Huynh, W. Kim, C. Lee, Y. Nam, S. Lee, K.-B. Chung and D. Choi, *Nano Energy*, 2018, **50**, 9–15.
72 F. Chen, H. W. Huang, L. Guo, Y. H. Zhang and T. Y. Ma, *Angew. Chem., Int. Ed.*, 2019, **58**, 10061–10073.
73 H. W. Huang, S. C. Tu, C. Zeng, T. R. Zhang, A. H. Reshak and Y. H. Zhang, *Angew. Chem., Int. Ed.*, 2017, **56**, 11860–11864.
74 L. Chen, H. M. Li, Z. Wu, L. L. Feng, S. G. Yu, H. F. Zhang, J. Gao, Y. W. Mai and Y. M. Jia, *Ceram. Int.*, 2020, **46**, 16763–16769.
75 M. Sharma, V. P. Singh, S. Kumar and R. Vaish, *J. Appl. Phys.*, 2020, **127**, 135103.
76 H. Nam, S. Kim, G. P. Khanal, I. Fujii, S. Ueno and S. Wada, *Jpn. J. Appl. Phys.*, 2019, **58**, Slld04.
77 M. D. Min, Y. M. Liu, C. Y. Song, D. W. Zhao, X. Y. Wang, Y. M. Qiao, R. Feng, W. Hao, P. Tao, W. Shang, J. B. Wu and T. Deng, *ACS Appl. Mater. Interfaces*, 2018, **10**, 21246–21253.
78 S. Tu, H. Huang, T. Zhang and Y. Zhang, *Appl. Catal., B*, 2017, **219**, 550–562.
79 F. Mushtaq, H. Torlakcik, M. Hoop, B. Jang, F. Carlson, T. Grunow, N. Läubli, A. Ferreira, X. Z. Chen, B. J. Nelson and S. Pané, *Adv. Funct. Mater.*, 2019, **29**, 1808135.
80 Q. Xu, X. Gao, S. Zhao, Y.-N. Liu, D. Zhang, K. Zhou, H. Khanbareh, W. Chen, Y. Zhang and C. Bowen, *Adv. Mater.*, 2021, **33**, 2008452.
81 K. Kapat, Q. T. H. Shubhra, M. Zhou and S. Leeuwenburgh, *Adv. Funct. Mater.*, 2020, **30**, 1909045.
82 Z. Zhang, Y. Wang, H. Zhang, Z. Tang, W. Liu, Y. Lu, Z. Wang, H. Yang, W. Pang, H. Zhang, D. Zhang and X. Duan, *Small*, 2017, **13**, 1602962.
83 A. Ramedani, O. Sabzevari and A. Simchi, *Int. J. Pharm.*, 2022, **629**, 122373.
84 P. Zhu, H. Peng, L. Mao and J. Tian, *IEEE Trans. Ultrason Ferroelectr. Freq. Control.*, 2021, **68**, 952–960.
85 C. Pucci, A. Marino, O. Sen, D. De Pasquale, M. Bartolucci, N. Iturrioz-Rodriguez, N. di Leo, G. de Vito, D. Debellis, A. Petretto and G. Ciofani, *Acta Biomater.*, 2022, **139**, 218–236.
86 X. Z. Chen, M. Hoop, N. Shamsudhin, T. Huang, B. Ozkale, Q. Li, E. Siringil, F. Mushtaq, L. Di Tizio, B. J. Nelson and S. Pane, *Adv. Mater.*, 2017, **29**, 1605458.
87 A. Rodzinski, R. Guduru, P. Liang, A. Hadjikhani, T. Stewart, E. Stimphil, C. Runowicz, R. Cote, N. Altman, R. Datar and S. Khizroev, *Sci. Rep.*, 2016, **6**, 20867.
88 G. Ciofani, S. Danti, D. D'Alessandro, S. Moscato, M. Petrini and A. Menciassi, *Nanoscale Res. Lett.*, 2010, **5**, 1093–1101.
89 D. X. Ye, Y. Y. Ma, W. Zhao, H. M. Cao, J. L. Kong, H. M. Xiong and H. Mohwald, *ACS Nano*, 2016, **10**, 4294–4300.
90 A. Marino, E. Almici, S. Migliorin, C. Tapeinos, M. Battaglini, V. Cappello, M. Marchetti, G. de Vito, R. Cicchi, F. S. Pavone and G. Ciofani, *J. Colloid Interface Sci.*, 2019, **538**, 449–461.
91 Y. C. A. J. S. Han Lin, *Chem. Soc. Rev.*, 2018, **47**, 1938.
92 X. Li, J. F. Lovell, J. Yoon and X. Chen, *Nat. Rev. Clin. Oncol.*, 2020, **17**, 657–674.
93 T. C. Pham, V. N. Nguyen, Y. Choi, S. Lee and J. Yoon, *Chem. Rev.*, 2021, **121**, 13454–13619.
94 S. Son, J. H. Kim, X. Wang, C. Zhang, S. A. Yoon, J. Shin, A. Sharma, M. H. Lee, L. Cheng, J. Wu and J. S. Kim, *Chem. Soc. Rev.*, 2020, **49**, 3244–3261.
95 X. Cui, X. Han, L. Yu, B. Zhang and Y. Chen, *Nano Today*, 2019, **28**, 100773.
96 X. Wang, X. Zhong, Z. Liu and L. Cheng, *Nano Today*, 2020, **35**, 100946.

97 P. Zhao, Y. Jiang, Z. Tang, Y. Li, B. Sun, Y. Wu, J. Wu, Y. Liu and W. Bu, *Angew. Chem., Int. Ed.*, 2021, **60**, 8905–8912.
98 W. Fan, N. Lu, Z. Shen, W. Tang, B. Shen, Z. Cui, L. Shan, Z. Yang, Z. Wang, O. Jacobson, Z. Zhou, Y. Liu, P. Hu, W. Yang, J. Song, Y. Zhang, L. Zhang, N. M. Khashab, M. A. Aronova, G. Lu and X. Chen, *Nat. Commun.*, 2019, **10**, 1241.
99 K. Ni, G. Lan, S. S. Veroneau, X. Duan, Y. Song and W. Lin, *Nat. Commun.*, 2018, **9**, 4321.
100 W. Sun, L. Luo, Y. Feng, Y. Cai, Y. Zhuang, R. J. Xie, X. Chen and H. Chen, *Angew. Chem., Int. Ed.*, 2020, **59**, 9914–9921.
101 T. Gu, Y. Wang, Y. Lu, L. Cheng, L. Feng, H. Zhang, X. Li, G. Han and Z. Liu, *Adv. Mater.*, 2019, **31**, e1806803.
102 Z. Lu, J. Gao, C. Fang, Y. Zhou, X. Li and G. Han, *Adv. Sci.*, 2020, **7**, 2001223.
103 Y. Zhao, S. Wang, Y. Ding, Z. Zhang, T. Huang, Y. Zhang, X. Wan, Z. L. Wang and L. Li, *ACS Nano*, 2022, **16**, 9304–9316.
104 H. Hu, W. Feng, X. Qian, L. Yu, Y. Chen and Y. Li, *Adv. Mater.*, 2021, **33**, 2005062.
105 H. Quan Truong, V. Ravichandran, C. Thuy Giang Nguyen, J. H. Kang, Y. T. Ko, T. I. Lee and M. S. Shim, *Chem. Eng. J.*, 2022, **435**, 135039.
106 Y. Liao, D. Wang, S. Zhu, R. Zhou, F. Rahbarizadeh and Z. Gu, *Nano Today*, 2022, **44**, 101510.
107 H. Ge, J. Du, J. Zheng, N. Xu, Q. Yao, S. Long, J. Fan and X. Peng, *Chem. Eng. J.*, 2022, **446**, 137040.
108 P. Zhu, Y. Chen and J. L. Shi, *Adv. Mater.*, 2020, **32**, 2001976.
109 Z. Y. Li, T. M. Zhang, F. Fan, F. Gao, H. X. Ji and L. H. Yang, *J. Phys. Chem. Lett.*, 2020, **11**, 1228–1238.
110 Q. Xu, X. Gao, M. Wen, Y. Liu, Y. Li, C. Wei, X. Wu, Y. Zou, J. Li, X. Li, Y. N. Liu and W. Chen, *ACS Appl. Mater. Interfaces*, 2022, **14**, 28199–28210.
111 Y. Chang, Y. Cheng, R. X. Zheng, X. Q. Wu, P. P. Song, Y. J. Wang, J. Yan and H. Y. Zhang, *Nano Today*, 2021, **38**, 101110.
112 Y. He, Z. Li, C. Cong, F. Ye, J. Yang, X. Zhang, Y. Yuan, Z. Ma, K. Zhang, Y. Lin, L. Zheng, X. J. Liang and D. Gao, *ACS Nano*, 2021, **15**, 10488–10501.
113 X.-Z. Chen, J.-H. Liu, M. Dong, L. Müller, G. Chatzipirpiridis, C. Hu, A. Terzopoulou, H. Torlakcik, X. Wang, F. Mushtaq, J. Puigmartí-Luis, Q.-D. Shen, B. J. Nelson and S. Pané, *Mater. Horiz.*, 2019, **6**, 1512–1516.
114 M. Ge, D. Xu, Z. Chen, C. Wei, Y. Zhang, C. Yang, Y. Chen, H. Lin and J. Shi, *Nano Lett.*, 2021, **21**, 6764–6772.
115 A. R. K. Sasikala, V. K. Kaliannagounder, N. R. Alluri, B. K. Shrestha, S.-J. Kim, H. Ali-Boucetta, C. H. Park and A. R. Unnithan, *Nano Energy*, 2022, **96**, 107134.
116 P. I. P. Soares, I. M. M. Ferreira, R. A. G. B. N. Igreja, C. M. M. Novo and J. P. M. R. Borges, *Recent Pat. Anti-Canc*, 2012, **7**, 64–73.
117 A. Belous, A. Tovstolytkin, S. Solopan, Y. Shlapa and O. Fedorchuk, *Acta Phys. Pol., A*, 2018, **133**, 1006–1012.
118 L. Bubnovskaya, A. Belous, S. Solopan, A. Kovelskaya, L. Bovkun, A. Podoltsev, I. Kondtratenko and S. Osinsky, *J. Nanopart.*, 2014, **2014**, 1–9.
119 Z. H. Dai, Y. Fujita and Y. Akishige, *Mater. Lett.*, 2011, **65**, 2036–2038.
120 Y. Kong, F. Liu, B. Ma, J. Duan, W. Yuan, Y. Sang, L. Han, S. Wang and H. Liu, *Adv. Sci.*, 2021, **8**, 2100962.
121 R.-Q. Li, D.-W. Zheng, Z.-Y. Han, T.-Q. Xie, C. Zhang, J.-X. An, R. Xu, Y.-X. Sun and X.-Z. Zhang, *Mater. Today*, 2020, **40**, 91–100.
122 Y. N. Yoon, D. S. Lee, H. J. Park and J. S. Kim, *Sci. Rep.*, 2020, **10**, 2560.
123 F. van Zaane, D. Subbaiyan, A. van der Ploeg-van den Heuvel, H. S. de Bruijn, E. M. Balbas, G. Pandraud, H. J. Sterenborg, P. J. French and D. J. Robinson, *J. Biophotonics*, 2010, **3**, 347–355.
124 K. Yamagishi, I. Kirino, I. Takahashi, H. Amano, S. Takeoka, Y. Morimoto and T. Fujie, *Nat. Biomed. Eng.*, 2019, **3**, 27–36.
125 G. Li, N. A. Patel, E. C. Burdette, J. G. Pilitsis, H. Su and G. S. Fischer, *IEEE ASME Trans. Mechatron*, 2021, **26**, 255–266.
126 A. Kim, S. K. Lee, T. Parupudi, R. Rahimi, S. H. Song, M. C. Park, S. Islam, J. Zhou, A. K. Majumdar, J. S. Park, J. M. Yoo and B. Ziaie, *Sci. Rep.*, 2020, **10**, 1510.
127 C. Zhang, Y. Li, X. Ma, W. He, C. Liu and Z. Liu, *Sci. China: Chem.*, 2021, **64**, 1–16.
128 Y. Dong, S. Dong, B. Liu, C. Yu, J. Liu, D. Yang, P. Yang and J. Lin, *Adv. Mater.*, 2021, **33**, e2106838.
129 Z. M. Tang, P. R. Zhao, D. L. Ni, Y. Y. Liu, M. Zhang, H. Wang, H. Zhang, H. B. Gao, Z. W. Yao and W. B. Bu, *Mater. Horiz.*, 2018, **5**, 946–952.
130 R. H. Huang, N. B. Sobol, A. Younes, T. Mamun, J. S. Lewis, R. V. Ulijn and S. O'Brien, *ACS Appl. Mater. Interfaces*, 2020, **12**, 51135–51147.
131 Y. Liu, Y. Wang, W. Y. Zhen, Y. H. Wang, S. T. Zhang, Y. Zhao, S. Y. Song, Z. J. Wu and H. J. Zhang, *Biomaterials*, 2020, **251**, 120075.
132 L. L. Feng, S. L. Gai, F. He, P. P. Yang and Y. L. Zhao, *ACS Nano*, 2020, **14**, 7245–7258.
133 D. Staedler, T. Magouroux, R. Hadji, C. Joulaud, J. Extermann, S. Schwung, S. Passemard, C. Kasparian, G. Clarke, M. Gerrmann, R. Le Dantec, Y. Mugnier, D. Rytz, D. Ciepielewski, C. Galez, S. Gerber-Lemaire, L. Juillerat-Jeanneret, L. Bonacina and J. P. Wolf, *ACS Nano*, 2012, **6**, 2542–2549.
134 P. Pantazis, J. Maloney, D. Wu and S. E. Fraser, *Proc. Natl. Acad. Sci. U. S. A.*, 2010, **107**, 14535–14540.
135 L. Dubreil, I. Leroux, M. Ledevin, C. Schleder, L. Lagalice, C. Lovo, R. Fleurisson, S. Passemard, V. Kilin, S. Gerber-Lemaire, M. A. Colle, L. Bonacina and K. Rouger, *ACS Nano*, 2017, **11**, 6672–6681.
136 A. Y. Sonay, K. Kalyviotis, S. Yaganoglu, A. Unsal, M. Konantz, C. Teulon, I. Lieberwirth, S. Sieber, S. Jiang, S. Behzadi, D. Crespy, K. Landfester, S. Roke, C. Lengerke and P. Pantazis, *ACS Nano*, 2021, **15**, 4144–4154.
137 Y. F. Wang, A. Barhoumi, R. Tong, W. P. Wang, T. J. Ji, X. R. Deng, L. L. Li, S. A. Lyon, G. Reznor, D. Zurakowski and D. S. Kohane, *Acta Biomater.*, 2018, **72**, 287–294.

138 C. L. Hsieh, R. Grange, Y. Pu and D. Psaltis, *Opt. Express*, 2009, **17**, 2880–2891.
139 J. Vuilleumier, G. Gaulier, R. De Matos, D. Ortiz, L. Menin, G. Campargue, C. Mas, S. Constant, R. Le Dantec, Y. Mugnier, L. Bonacina and S. Gerber-Lemaire, *ACS Appl. Mater. Interfaces*, 2019, **11**, 27443–27452.
140 G. G. Genchi, A. Marino, A. Rocca, V. Mattoli and G. Ciofani, *Nanotechnology*, 2016, **27**, 232001.
141 S. Semenov, N. Pham and S. Egot-Lemaire, in *Micro-and Nanosystems in Medicine, Active Implants, Biosensors*, ed. O. Dissel and W. C. Schlegel, 2009, vol. 25, pp. 311–313.
142 Y. F. Chen, P. Kosmas and S. Martel, *Int. J. Antennas Propag.*, 2013, **2013**, 309703.
143 W. Ding, Z. Ji and D. Xing, *Appl. Phys. Lett.*, 2017, **110**, 183701.
144 G. Ku and L. V. Wang, *Med. Phys.*, 2001, **28**, 4–10.
145 P. T. Sujai, M. M. Joseph, G. Saranya, J. B. Nair, V. P. Murali and K. K. Maiti, *Nanoscale*, 2020, **12**, 6971–6975.
146 B. Tandon, J. J. Blaker and S. H. Cartmell, *Acta Biomater.*, 2018, **73**, 1–20.
147 M. Berggren, E. D. Glowacki, D. T. Simon, E. Stavrinidou and K. Tybrandt, *Chem. Rev.*, 2022, **122**, 4826–4846.
148 Y. He, Z. Xu, Y. He, G. Cao, S. Ni, Y. Tang, J. Wang, Y. Yuan, Z. Ma, D. Wang and D. Gao, *Biomaterials*, 2022, **290**, 121816.
149 L. Zhan, C. Xiao, C. Li, J. Zhai, F. Yang, J. Piao, C. Ning, Z. Zhou, P. Yu and S. Qi, *ACS Appl. Mater. Interfaces*, 2022, **14**, 45032–45041.
150 A. G. Athanassiadis, Z. Ma, N. Moreno-Gomez, K. Melde, E. Choi, R. Goyal and P. Fischer, *Chem. Rev.*, 2022, **122**, 5165–5208.